

Diss. ETH No. 23348

***Tailoring Conductive Metal Oxides
for
Photochemical and Electrochemical Applications***

A thesis submitted to attain the degree of

DOCTOR OF SCIENCES of ETH ZURICH

(Dr. sc. ETH Zurich)

presented by

Emma Elizabeth Oakton

MSci Chemistry with Research Abroad, Imperial College London

born on 30.07.1990

citizen of

The United Kingdom of Great Britain and Northern Ireland

accepted on the recommendation of

Prof. Dr. Christophe Copéret, examiner

Prof. Dr. Markus Niederberger, co-examiner

Prof. Dr. Thomas J. Schmidt, co-examiner

2016

*You don't know,
until you try.*

to Martin and my Parents

Acknowledgements

A PhD would be difficult to go through alone. I have been lucky enough to be surrounded by people who have supported me along the way. My parents, Julie and Dave, are a constant source of love and support for which I am eternally grateful. To my brother James and great friends Ruth and Rachel, although we don't talk that often I know I can count on you, as you can on me. Living away from my family has not been easy, but having Martin by my side has made it a whole lot easier - thank you for being everything I need. To Martin's family and friends thank you for welcoming me with open arms. Support from your family and friends is vital, but so is support from yourself. Bella and Anna have helped me understand the importance of taking that moment to ask yourself, "How am I doing?".

Of course I wouldn't be writing this thesis if it wasn't for Christophe giving me the opportunity to work in his group - thank you. It has been great to conduct my research alongside wonderful colleagues and friends. I thank all Copéret group members, both past and present for your help, invaluable advice and a great working atmosphere. To Georges thanks for making sessions at the F30 bearable, your XAS expertise and our photocatalysis collaboration. I would like to thank Matt, Giuseppe, Wei-Chih, Deven, Dan, Victor, Murielle, Keith and Wolfram for the interesting and insightful discussions over coffee/tea, which have kept me going from day-to-day. I will definitely miss this time spent with you all, but also look back on it with great fondness for years to come.

Whilst conducting this scientific work, I have had the opportunity to work with expert collaborators from whom I have learned a great deal. I thank Alexey for his guidance and advice throughout my PhD. I would like to thank all members involved in project DuraCAT. Thank you to the members of the Electrochemistry Laboratory at the Paul Scherrer Institute, Tobias, Emiliana, Mauro and Daniel, who have contributed to this thesis. Thank you to Jeremy and Olha at CSEM for their expertise in XRD. I would like to thank Frank and Fabian for their guidance in the world of electron microscopy. This work has been conducted as part of project DuraCAT supported financially by The Competence Center Energy and Mobility (CCEM) and Umicore AG. I also thank the Swiss Competence Center for Energy Research (SCCER) for additional financial support.

Contents

Abstract	vii
Zusammenfassung	ix
1 Introduction	1
2 Blue Tungsten Oxide: Synthesis, Electrochemical Properties and Photocatalytic Performance	7
2.1 Individual Contributions	7
2.2 Introduction	7
2.3 Results and Discussion	9
2.3.1 Precursor Effect on Phase and Morphology	9
2.3.2 Electrochemical Stability	18
2.3.3 Photocatalytic Activity	20
2.4 Conclusion	23
2.5 Experimental Details	24
2.5.1 General	24
2.5.2 Preparation of Blue Tungsten Oxides	25
2.5.3 Oxide Post-Synthetic Treatment	25
2.5.4 Electrochemical Stability Tests	25
2.5.5 Photocatalytic Activity Tests	26
3 Niobium and Antimony-doped Tin Oxide: Structural Differences and Consequences for Electrical Conductivity	27

3.1	Individual Contributions	27
3.2	Introduction	27
3.3	Results and Discussion	29
3.3.1	Optimisation of Niobium-doped Tin Oxide	29
3.3.2	Preparation of Antimony-doped Tin Oxide and Comparison to Niobium-doped Tin Oxide	32
3.3.3	Detailed Characterisation of Tin Oxide, Niobium-doped Tin Ox- ide and Antimony-doped Tin Oxide	36
3.4	Conclusion	42
3.5	Experimental Details	43
3.5.1	General	43
3.5.2	XRD Characterisation	44
3.5.3	Preparation of SnO_2	44
3.5.4	Representative Preparation of $\text{SnO}_2\text{:Nb}$	45
3.5.5	Preparation of $\text{SnO}_2\text{:Sb}$	45
3.5.6	Preparation of Nb_2O_5	45
3.5.7	Post-synthetic Treatment	45
4	Iridium Titanium Oxide: Preparation, Optimisation and Application in Electro- chemical Oxygen Evolution	47
4.1	Individual Contributions	47
4.2	Introduction	47
4.3	Results and Discussion	49
4.3.1	Composition Optimisation	49
4.3.2	$\text{IrO}_2\text{-MO}_x$: Comparing $M = \text{Ti, Sn and Nb}$	56
4.3.3	Chlorine-free Iridium Titanium Oxide	60
4.3.4	Activity and Stability of Chlorine-free Iridium Titanium Oxide in Electrocatalytic Oxygen Evolution	64
4.4	Conclusion	71
4.5	Experimental Details	72

4.5.1	General	72
4.5.2	Representative preparation of 40%IrO ₂ -60%TiO ₂ (Cl)	73
4.5.3	Representative preparation of 40%IrO ₂ -60%TiO ₂ (acac)	73
4.5.4	Electrochemical RDE Experiments	74
5	Oxide Supported Pt Nanoparticles: Preparation, Activity and Stability in Oxygen Reduction	75
5.1	Individual Contributions	75
5.2	Introduction	75
5.3	Results and Discussion	76
5.3.1	Precursor Impregnation	76
5.3.2	Impregnation of Colloidal Pt Solutions	78
5.3.3	Homogeneous Deposition Precipitation	82
5.3.4	Electrochemical Activity and Stability of Pt/IrO ₂ -TiO ₂ in the Oxygen Reduction Reaction	85
5.4	Conclusion	91
5.5	Experimental Details	92
5.5.1	General	92
5.5.2	Impregnation of Tetraammineplatinum(II) nitrate	92
5.5.3	Representative Colloidal Procedure	93
5.5.4	Preparation of Antimony-doped Tin Oxide	93
5.5.5	Colloid Impregnation	93
5.5.6	Representative Homogeneous Deposition Precipitation Procedure	93
5.5.7	Anomalous SAXS Characterisation	94
5.5.8	Electrochemical RDE Experiments	94
6	Conclusion and Outlook	97
	References	103

Abstract

The wider application of Polymer Electrolyte Fuel Cell (PEFC) technology is limited by the degradation of carbon components. Metal oxides are expected to play a key role in increasing PEFC durability, however optimising their electrical conductivity for electrochemical applications remains a challenge. Herein, three methods to increase oxide conductivity are investigated; namely inducing the formation of oxygen defects, adding dopant centers to a host lattice and the efficient use of an intrinsically conductive oxide. Furthermore, combining PEFCs with photo- or electrocatalytic water splitting would allow for direct H_2 and O_2 supply, although this process is limited by sluggish water oxidation (oxygen evolution). Consequently, select oxide materials are also investigated as oxygen evolution catalysts.

The effect of oxygen deficiency on electrical conductivity is investigated for tungsten oxide. High surface area blue tungsten oxides are prepared using a non-hydrolytic sol-gel method. Transmission electron microscopy (TEM) imaging reveals a striking difference in particle morphology, with cubic-shape particles formed from WCl_6 and rod-shape particles from WCl_4 (DME). Electron paramagnetic resonance (EPR) spectroscopy and X-ray diffraction (XRD) indicate the presence of oxygen defects, which likely cause the increase in electrical conductivity observed with respect to WO_3 . Electrochemical stability tests and X-ray photoelectron spectroscopy (XPS) show that oxygen deficient tungsten oxide is oxidised during potential cycling, demonstrating that oxygen deficient materials do not have sufficient stability for electrochemical applications. The activity of tungsten oxide in photocatalytic oxygen evolution is investigated and oxygen deficiency as well as particle size are used to rationalise the decreased photocatalytic activity of these materials with respect to commercial WO_3 .

Doping is studied as an approach to improve electrical conductivity using tin oxide (SnO_2) as a host oxide. Niobium (Nb) and antimony (Sb) doped tin oxides are prepared by an aqueous co-precipitation method and while Sb-doped tin oxide has a vastly improved electrical conductivity in comparison to SnO_2 , little influence on conductivity is observed for doping with Nb. XRD and energy dispersive X-ray (EDX) spectroscopy indicate both materials have comparable structures. Following oxide crystallisation by variable temperature XRD reveals that the crystallite growth of Nb-doped tin oxide is limited in comparison to pure SnO_2 and Sb-doped SnO_2 , which alongside the presence of tetrahedral Nb sites identified by Nb K-edge X-ray absorption spectroscopy (XAS) confirms Nb segregation in Nb-doped tin oxide. Interestingly, ^{119}Sn nuclear magnetic resonance (NMR) spectroscopy shows that Nb does influence the environment

of Sn^{4+} , leading to the conclusion that Nb is partially segregated. The effective reduction in Nb distributed within the SnO_2 host lattice justifies the low conductivity of niobium-doped tin oxide.

Optimising the use of an expensive intrinsically conductive oxide through combination with a stable, non-conductive oxide is investigated using iridium and titanium oxides. Iridium titanium oxide materials are prepared by a one-pot Adams method reaction ($\text{IrO}_2\text{-TiO}_2$). Mixtures of TiO_2 and IrO_2 particles are obtained where IrO_2 particle size, 1 nm diameter, is independent of Ir : Ti ratio. A minimal iridium content of 40 mol_M% is required to achieve an electrical conductivity sufficient for electrochemical applications. The synthetic method is extended to $\text{IrO}_2\text{-MO}_x$ ($M = \text{Sn}$ or Nb), which have similar morphologies, but lower electrical conductivities than $\text{IrO}_2\text{-TiO}_2$. Chlorine free iridium oxide containing materials are prepared and used as catalysts for electrochemical oxygen evolution and demonstrate high activities, which are rationalised by the amorphous nature of the iridium oxide formed by Adams method. In addition to their high activities, the use of iridium titanium oxide materials provides an opportunity to optimise Ir content in the catalyst layer, which would have a significant impact on the cost of water electrolyzers. Furthermore these materials have additional applications as PEFC catalyst supports.

In addition to the catalyst support, the active catalyst phase for oxygen reduction (Pt) is of high importance for the operation of PEFCs. Consequently, methods to yield oxide supported Pt nanoparticles are investigated. Precursor impregnation requires H_2 treatment and characterisation during the reduction process shows that co-reduction of supports such as SnO_2 may lead to ill-defined catalyst structures. Alternatively, colloidal methods can be used to prepare Pt nanoparticles, which do not require reduction after impregnation on an oxide support. However, oxidative removal of the stabilising ligand may leave decomposition products, which hinder electrochemical applications. On the other hand, homogeneous deposition precipitation yields small Pt nanoparticles supported on iridium titanium oxides, without the need for post-synthetic treatment. These materials show improved stability in the oxygen reduction reaction, but reduced activity in comparison to commercial alternatives. The improved stability can be attributed to the increased surface area of the support and the chlorine free method of nanoparticle deposition.

Zusammenfassung

Die alltägliche Anwendung von Polyelektrolytbrennstoffzellen (PEFCs) ist auf Grund der Zersetzung von kohlenstoffhaltigen Bestandteilen begrenzt. Metalloxide spielen in der Erhöhung der Lebensdauer von PEFCs eine Schlüsselrolle; die Herausforderung besteht jedoch darin, deren elektrische Leitfähigkeit zu optimieren. Hier werden drei Methoden zur Optimierung der Leitfähigkeit von Oxiden präsentiert: der gezielte Einbau von Sauerstoff-Fehlstellen, die Dotierung und eine effizientere Verwendung von leitenden Oxiden. Die Kombination von PEFCs mit photo- oder elektrokatalytischer Wasserspaltung würde eine unmittelbare Versorgung mit H_2 und O_2 erlauben, trotz der geringen Effizienz der Sauerstoff Generierung. Daher werden ausgewählte Oxide auch als Katalysatoren für die Sauerstoff Generierung untersucht.

Der Erhöhung der elektrischen Leitfähigkeit durch Sauerstoff-Fehlstellen wurde an Wolframoxid (WO_x) untersucht. Durch ein wasserfreies Sol-Gel Verfahren wurde blaues Wolframoxid mit einer hohen Oberfläche hergestellt. Transmissionselektronenmikroskopische (TEM) Bilder zeigen die unterschiedliche Morphologie des Oxids - abhängig vom Ausgangsstoff - z.B. kubische Partikel wenn WCl_6 und stäbchenförmige Partikel wenn WCl_4 (DME) verwendet wird. Elektronenresonanzspektroskopie (EPR) und Röntgenbeugung (XRD) bestätigen das Vorhandensein von Sauerstoff-Fehlstellen, welche höchstwahrscheinlich für die erhöhte Leitfähigkeit im Vergleich zu handelsüblichem WO_3 verantwortlich sind. Elektrochemische Stabilitätstests und Röntgenphotoelektronenspektroskopie deuten auf eine Oxidation des Materials hin. Dies beweist, dass Materialien mit Sauerstoff-Fehlstellen keine ausreichende Stabilität in Bezug auf elektrochemische Anwendungen haben. Die photokatalytische Erzeugung von Sauerstoff mittels Wolframoxid wurde ebenfalls untersucht. Hierbei konnten die Sauerstoff-Fehlstellen sowie die kleinen Partikelgrößen als Erklärung für die geringere Aktivität im Vergleich zu WO_3 dienen.

Dotierung - zur Erhöhung der Leitfähigkeit - wurde am Zinnoxid (SnO_2) untersucht. Niobium (Nb) und Antimon (Sb) dotierte Zinnoxide wurden durch Ausfällung in wässriger Lösung erhalten. Während das Sb dotierte Material eine besser Leitfähigkeit aufweist, zeigt das Nb dotierte Oxid fast keinen Unterschied zum reinen SnO_2 . XRD und örtlich aufgelöste Energiedispersive Röntgenspektroskopie (EDX) zeigen jedoch, dass beide Materialien vergleichbare Strukturen haben. Ein unterschiedliches Kristallwachstum kann mit Temperatur variabler XRD eindeutig gezeigt werden, die Kristallgröße von Nb dotiertem Zinnoxid ist im Vergleich zu reinem und Sb dotiertem Zinnoxid begrenzt. Röntgenabsorptionsspektroskopie (XAS) deutet auf eine örtliche Abgrenzung von Nb in Nb dotiertem SnO_2 hin. Interessanterweise zeigt ^{119}Sn Kernspinresonanz (NMR) Spektroskopie, dass Nb die Umgebung von Sn^{4+} beein-

flusst und somit nur teilweise isoliert vorkommt. Die effektive Reduktion von Nb, welches im Zinnoxid verteilt ist, erklärt die geringe Leitfähigkeit von Nb dotiertem Zinnoxide.

Durch die Kombination von teuren, leitenden Oxiden mit stabilen, nicht-leitenden Oxiden kann die Wirtschaftlichkeit der resultierenden Materialien gesteigert werden, hierfür wurden Iridium (Ir) Titanoxide nach der Adams Methode hergestellt. In den resultierenden TiO_2 und IrO_2 Mischungen ist die IrO_2 Partikelgrösse (1 nm) unabhängig von dem Ir : Ti Verhältnis. Ein Minimalgehalt von 40 mol_M% Ir ist notwendig, um für die elektrochemische Anwendung genügend hohe Leitfähigkeit zu erhalten. Das synthetische Verfahren wurde auf $\text{IrO}_2\text{-MO}_x$ (M = Sn oder Nb) ausgeweitet wobei ähnliche Partikelformen mit geringerer Leitfähigkeit als $\text{IrO}_2\text{-TiO}_2$ entstehen. Chlorfreie Materialien basierend auf Iridiumoxid weisen hohe Aktivitäten als Katalysatoren für die Erzeugung von Sauerstoff auf, was der amorphen Struktur der Partikel aus der Adams Methode zugeschrieben wird. Zusätzlich gibt es bei $\text{IrO}_2\text{-TiO}_2$ Materialien die Möglichkeit, den Gehalt an Ir in der Oberfläche zu optimieren, was eine signifikante Auswirkung auf den Preis solcher Katalysatoren hätte. Zusätzlich könnten diese Materialien auch in PEFCs als Katalysatorträger eingesetzt werden.

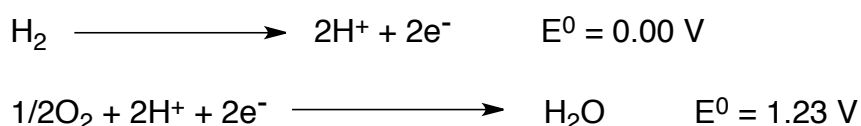
Neben dem Träger ist natürlich der Katalysator für die Reduktion von Sauerstoff äusserst wichtig damit eine PEFC funktioniert, dabei wird meist Platin (Pt) als Katalysator verwendet. Konsequenterweise wurden Verfahren untersucht, um Pt-Partikel gezielt auf dem Träger abzulagern. Die Imprägnierung erfordert eine Reduktion mittels H_2 , jedoch zeigen Studien, dass eine Co-Reduktion des Trägers und SnO_2 zu schlecht definierten Strukturen des Katalysators führt. Demgegenüber benötigen Verfahren basierend auf kolloidalen Suspensionen kein H_2 um Pt auf dem Träger abzulagern. Dabei wird der Stabilisierungsligand des Kolloids oxidativ entfernt, was zu elektrochemisch störenden Zersetzungsrückständen führen kann. Im Gegensatz dazu führt Deposition durch homogene Ausfällung zu kleinen Pt-Partikel auf dem Träger ($\text{IrO}_2\text{-TiO}_2$) ohne Nachbehandlung. Diese Materialien zeichnen sich durch erhöhte Stabilität in der Reduzierung von Sauerstoff aus - jedoch weisen sie eine geringere Aktivität als kommerzielle Katalysatoren auf. Die erhöhte Stabilität kann der höheren Oberfläche des Trägers als auch der chlorfreien Methode zur Ablagerung der Pt-Partikel zugeschrieben werden.

1 Introduction

The increasing global energy demand has triggered continuous, vigorous searches for new fossil fuel sources.^[1] However, considering the known contribution of such carbon based energy sources to global climate change, there has been a multi-faceted effort towards the development of renewable energy technologies. Nonetheless fossil fuels benefit from being easily stored for long periods, whilst the sporadic nature of renewable energy resources means that storage of the generated energy needs to be addressed.^[2]

Using hydrogen as an energy carrier is an idea that has been developed by many scientists over the past century.^[3–6] Hydrogen can be generated using renewable energy, either photocatalytically^[7–10] or electrocatalytically^[11–13] and stored for later use.^[14–18] Hydrogen can then be utilised to generate energy or other fuels in a variety of different ways. The Fisher-Tropsch reaction, methanation reaction, Sabatier process and methanol synthesis can be used to transform H₂ to high value fuels and chemical feedstocks. However these pathways yield carbon based fuels, which depend on the effective capture of CO₂, produced during combustion, to avoid contributions to climate change.^[19] Looking towards a carbon-free energy route, H₂ itself can be used directly as a fuel, producing a single, simple by-product: H₂O.^[20,21]

Although hydrogen can be used directly in a conventional combustion engine with low undesirable emissions,^[21–23] electrochemical fuel cells offer an alternative way to generate energy from H₂ at lower temperatures and with higher efficiencies.^[20,24,25] Hydrogen powered fuel cells combine the oxidation of hydrogen and reduction of oxygen to generate an electric current and H₂O (Scheme 1). Table 1 compares various hydrogen fuel cells and demonstrates the range of materials and operating temperatures, which can be used.^[20,25] This variety has led to a range of possible applications of hydrogen fuel cells including transportation as well as small and large scale stationary power generation.^[20,24,26] In particular, polymer electrolyte fuel cells (PEFCs) have low operating temperatures and high efficiencies, vital for quick start-up times and durability during long-term operation.

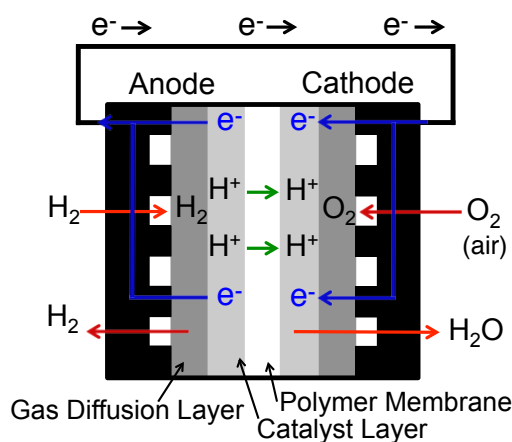


Scheme 1: Hydrogen oxidation and oxygen reduction half-reactions with standard potentials.

Table 1: Fuel cell comparison^[25]

Fuel Cell Type	Operation Temperature	Electrolyte	Electrical Efficiency
Alkaline	90 - 100 °C	Aqueous KOH	60%
Direct Methanol	60 - 200 °C	Perfluorosulfonic acid polymer	40%
Molten Carbonate	600 - 700 °C	Li_2CO_3 , Na_2CO_3 and K_2CO_3	45 - 47%
Phosphoric Acid	150 - 200 °C	H_3PO_4	>40%
Polymer Electrolyte	50 - 100 °C	Perfluorosulfonic acid polymer	53 - 58%
Solid Oxide	600 - 1000 °C	Stabilised zirconia	35 - 43%

Figure 1 shows a simplified structure of a PEFC membrane electrode assembly (MEA). The anodic and cathodic electrodes, composed of a gas diffusion layer and electrocatalyst layer, are separated by a proton conducting, polyfluorosulfonic acid, polymer membrane (commonly Nafion®).^[27] The catalyst layer itself is composed of two parts - the catalyst and its support. On either side of the electrodes are bipolar plates through which gas is delivered and multiple cells can be electrically connected.^[28] The hydrogen oxidation reaction (HOR) occurs at the anode. The protons are transferred from the anode to the cathode by the proton conducting membrane, and the electrons flow through an external circuit, which can be used to power devices. The oxygen reduction reaction (ORR) occurs at the cathode producing water. For efficient cell operation, all components need to be optimised to allow sufficient reactant transport to the catalyst. This means efficient electrical connection for electron transport, porosity for gas flow and catalyst-polymer contact for proton delivery.^[29]

**Figure 1:** Diagram of a PEFC membrane electrode assembly.

Most PEFC components are carbon based, which allows for good electrical connection and porosity.^[27] Platinum nanoparticles are deposited on high surface area carbon to form the catalyst layer of the anode and cathode.^[27,30] Although state-of-the-art PEFCs have many advantages (*vide supra*), their main disadvantages include high production costs and short operation lifetimes, with the latter mainly arising from the decomposition of the carbon-based components.^[31,32] It is known that carbon corrosion occurs at potentials over 0.8 V at operational temperatures (65 - 100 °C) and over 1.0 V at room temperature.^[33,34] Carbon corrosion is thought to be particularly common during both start-stop cycling and steady-state operation, where uneven gas flows can lead to dramatic variations in electrode potentials.^[27,28,34,35] Furthermore, the Pt based catalysts used in PEFCs are known to catalyse carbon oxidation at lower potentials.^[36] Recently, 3D imaging techniques revealed severe reductions in cathode porosity as a result of start-stop potential cycling, which is likely responsible for the observed drop in fuel cell performance through the limitation of mass transport.^[37] In addition to a variety of other catalyst layer degradation mechanisms, such as catalyst dissolution and the effects of generated water,^[27,28] such corrosion of the cell components can result in structural instability, membrane detachment and electrical disconnection of the catalyst, which leads to drops in operation efficiency and lifetime. Consequently, there is a large incentive to develop more durable materials for PEFCs, with a focus on catalyst supports.

For a new catalyst support to be considered as a competitive alternative to carbon, it must fulfill a specific set of criteria.^[38] Supports must be porous with high surface areas ($> 50 \text{ m}^2 \cdot \text{g}^{-1}$), which enables the catalyst loading to be maximised alongside enabling mass-transport and effective mixing with the polymer membrane. Additionally, the support must be stable under PEFC relevant conditions including acid solutions ($\text{pH} = 1$), high potential (0.8 V) at 80 °C. Most importantly, the material must have sufficient electronic conductivity to avoid large ohmic losses. Considering the polymer membrane has a conductivity around $0.02 \text{ S} \cdot \text{cm}^{-1}$ at 50% relative humidity, a support conductivity of around $0.1 \text{ S} \cdot \text{cm}^{-1}$ is widely considered as sufficient.^[38]

Recently, Sasaki and co-workers investigated the stable forms of a wide range of elements under PEFC relevant conditions ($\text{pH} = 0$, temperature = 80 °C and potential = 1.8 V vs. RHE).^[39] From thermochemically calculated pH-potential diagrams, a variety of metal oxides were highlighted as potential candidates for PEFC technology (Figure 2).

Li	Be	Metal-H₂O system at 80°C Molality m ($m = 10^{-8}$ mol/kg H ₂ O), pH = 0 Cathode Eh (vs. SHE) = 1.0 V										B	C	N	O	F
Li ⁺	Be ²⁺											H ₃ BO ₃ (a)	CO ₂ (a) CO ₂ (g)			
Na	Mg											Al	Si	P	S	Cl
Na ⁺	Mg ²⁺											Al ³⁺	H ₂ SiO ₃ (a) H ₄ SiO ₂	H ₄ P ₂ O ₇ (a)	HSO ₄ ⁻	
K	Ca	Sc	Ti	V	Cr	Mn	Fe	Co	Ni	Cu	Zn	Ga	Ge	As	Se	Br
K ⁺	Ca ²⁺	Sc ³⁺	TiO ₂	VO ₄ ⁻	Cr ³⁺	Mn ²⁺	Fe ³⁺ (Fe ₂ O ₃)	Co ²⁺	Ni ²⁺	Cu ²⁺	Zn ²⁺	Ga ³⁺	GeO ₂	HAsO ₄ (a)	H ₂ SeO ₃ (a)	
Rb	Sr	Y	Zr	Nb	Mo	Tc	Ru	Rh	Pd	Ag	Cd	In	Sn	Sb	Te	I
Rb ⁺	Sr ²⁺	Y ³⁺	ZrO ₂ ⁺	Nb ₂ O ₅	MoO ₃		RuO ₂	RhO ₂ (g)	PdO ₂	Ag ⁺	Cd ²⁺	In ³⁺	SnO ₂	Sb ₂ O ₃	Te(OH) ₆ (H ₂ TeO ₄)	
Cs	Ba		Hf	Ta	W	Re	Os	Ir	Pt	Au	Hg	Tl	Pb	Bi	Po	At
Cs ⁺	Ba ²⁺		HfO ₂	Ta ₂ O ₅	O ₂ W(OH) ₂	ReO ₄ ⁻	OsO ₄ (a) (OsO ₂)	IrO ₂	Pt	Au		Tl ⁺	Pb ²⁺	Bi ₂ O ₃		

Figure 2: Stable compounds under PEFC conditions. Copyright The Electrochemical Society 2010.^[39]

Sasaki et al. have demonstrated the promising stability of multiple metal oxides under PEFC relevant conditions.^[39] Additionally, the preparation of metal oxides through a variety of methods, particularly sol-gel chemistry, has been thoroughly documented and indeed such oxides can be prepared as high surface area powders.^[40–43] Therefore metal oxides have the potential to fulfill the PEFC requirements of stability and surface area. However few metal oxides are known to have inherently high electrical conductivity, a property vital to efficient cell operation.^[38] Iridium and ruthenium oxides are metallic type conductors, but their high cost is a disadvantage for commercial systems. Other less costly oxides such as WO₃, SnO₂ and TiO₂ are semiconductors, whose low temperature conductivity maybe increased through doping or varying oxygen stoichiometry. Consequently, a variety of tungsten,^[44,45] tin,^[46–48] niobium^[49–51] and titanium^[52–54] based oxides have been investigated as carbon alternative supports in PEFCs, showing improved oxidation stability. Interestingly, catalysts supported on tungsten oxide have also demonstrated improved poisoning resistance.^[55] Platinum nanoparticles supported on tin based oxides have demonstrated improved stability,^[56] which could be justified by increased amounts of platinum in the oxidation state Pt(0).^[57] Additionally, the ability to optimise the use of intrinsic conducting oxides such as IrO₂, through combination with titanium oxide, has been demonstrated as an alternative route to obtain conductive supports.^[58,59]

Alongside improved oxidation and poisoning resistance, increased catalyst activities have been observed in the presence of metal oxide supports in comparison to carbon supported materials.^[60–62] Improvements in the activity of Pt towards the oxygen reduction reaction have been observed under PEFC relevant conditions for a variety of oxide supports.^[56,61–63] This has been described by strong metal-support interactions, where the reducible nature of the metal oxide support allows for the perturbation of reactant and product adsorption energies on the

metal nanoparticle catalyst surface.^[64] Indeed X-ray photoelectron spectroscopy has identified a decrease in the binding energy of Pt 4f electrons when Pt nanoparticles are desposited on TiO₂ or WO₃ in comparison to carbon.^[60] In addition to changes in Pt binding energy, increased amounts of metallic Pt(0) were observed for Pt nanoparticles on tin oxide based supports, which likely contributes to the increased stability observed.^[56,57]

Polymer electrolyte fuel cells are a promising technology for a variety of mobile and stationary transport applications.^[20] However, in order for any application to be implemented on a large scale, significant infrastructural developments would be required.^[65] The ability to produce hydrogen in-situ, would be one way to avoid these issues.^[15] This could be achieved through the coupling of hydrogen evolution and hydrogen consumption with H₂ produced photocatalytically or electrocatalytically.^[14–16,66,67] Consequently, water could be used as the fuel, from which H₂ is generated and directly supplied to the fuel cell.

Fuel cells are typically supplied with oxygen through air flow, which does not demand particular infrastructural requirements. However, research has shown that fuel cells operate at higher efficiencies when supplied with pure O₂ in comparison to air, due to higher oxygen partial pressures reducing activation losses.^[68] Generating pure oxygen through photo- and/or electrocatalysis could make these improved efficiencies an accessible reality. Photocatalytic oxygen evolution is challenging due to the high number of photo-generated holes required for reaction and the necessary formation of two oxygen-oxygen bonds.^[69] Additionally, the photocatalyst must have a valence band energy, which is intrinsically more positive than the potential required for water oxidation.^[69] As a result only a few catalysts, namely those composed of W, Bi, V and Mo show higher oxygen evolution activities in comparison to hydrogen evolution.^[8] Similarly, efficient electrochemical oxygen evolution is limited by the high overpotentials required and catalyst optimisation is hindered by the similar adsorption properties of multiple intermediate species.^[70] Nonetheless, in addition to Pt, metal oxides such as RuO₂ and IrO₂ are active electrocatalysts for oxygen evolution.^[71,72] Although the high intrinsic electrical conductivity of these materials is an advantage for this electrochemical process, their high cost provides an incentive to optimise their usage. Interestingly, similarly to its potential application in PEFCs, the combination of IrO₂ with another stable oxide such as titanium dioxide has been investigated as a way to optimise IrO₂ usage for oxygen evolution.^[73]

This summary demonstrates the importance of photochemical and electrochemical processes in tackling the increasing global energy demand. Hydrogen can be used as an energy carrier through which renewable energy can be stored and the consequent consumption of hydrogen through PEFC technology presents a low emission, high efficiency route for power generation. Furthermore, the coupling of photocatalytic or electrocatalytic hydrogen and oxy-

gen evolution with PEFC technology presents the possibility of self-sufficient energy generation. However there are key developments still necessary to improve the commercial viability of this technology for large scale applications. These challenges include the development of durable, conductive materials for PEFC catalyst layers and improved catalysts for oxygen evolution.

A variety of metal oxides have been identified as suitable catalyst supports in PEFCs. Tungsten oxide supported catalysts have demonstrated improved poisoning resistance, whilst the increased activity of tin oxide supported Pt nanoparticles has been rationalised through metal support interactions. The combination of metallic conductors such as IrO_2 with other stable oxides presents the possibility of optimising the use of these expensive but conductive materials. Despite these reports, carbon remains the support of choice for PEFCs particularly due to its high electrical conductivity, surface area and porosity. Considering the preparation of high surface area metal oxides has been demonstrated with a variety of methods, improving the electrical conductivity of these materials remains the central challenge in improving their suitability for PEFCs.

This thesis focuses on the preparation of conductive, high surface area metal oxides of tungsten, tin, titanium and iridium for PEFC technology. Chapter 2 details the preparation of tungsten oxides by a non-hydrolytic sol-gel route, where electrical conductivity is improved through the modulation of oxygen stoichiometry. Doped tin oxides are discussed in Chapter 3, where a co-precipitation route leads to materials with differing conductivities when doped with niobium or antimony. Chapter 4 covers the combination of conductive iridium oxide with titanium oxide prepared by a simple one-pot high temperature method, where conductivity is optimised by varying iridium content. The development of these materials triggers the investigation of methods to prepare oxide supported Pt nanoparticles, which is covered in Chapter 5 along with their activity and stability towards oxygen reduction. To understand the properties of these materials, characterisation is essential. X-ray diffraction, N_2 adsorption-desorption and microscopy techniques are employed to have a detailed understanding of the oxide phase and morphology. X-ray absorption techniques are used to understand metal oxidation state and co-ordination environment. Rotating disk electrode experiments coupled with intense degradation protocols are used to investigate the suitability of select materials for PEFCs. Tungsten oxide and iridium oxide have additional applications as oxygen evolution catalysts. The photocatalytic performance of tungsten oxide in oxygen evolution is assessed under UV irradiation in Chapter 2, whilst the electrocatalytic performance of iridium titanium oxide mixtures are detailed in Chapter 4.

2 Blue Tungsten Oxide: Synthesis, Electrochemical Properties and Photocatalytic Performance

2.1 Individual Contributions

All materials were prepared and characterised by E. Oakton unless otherwise stated. XANES characterisation was conducted by G. Siddiqi and V. Mougel at the Swiss Light Source (Paul Scherrer Institute) and analysed by G. Siddiqi. EPR measurements were performed by M. Schwarzwälder. Electrical conductivity measurements were performed using the equipment of the Electrochemistry Laboratory at the Paul Scherrer Institute. Electrochemical stability tests and X-ray photoelectron spectroscopy measurements were performed by E. Fabbri at the Electrochemistry laboratory at the Paul Scherrer Institute. Photocatalytic tests were performed and analysed by G. Siddiqi.

This chapter includes work previously published by The Royal Society of Chemistry: Oakton, E.; Siddiqi, G.; Fedorov, A.; Copéret, C. *New. J. Chem.* **2016**, *40*, 217-222. Copyright, The Royal Society of Chemistry, 2016.

2.2 Introduction

Common forms of tungsten oxide include the bronze-coloured dioxide (WO_2) and yellow trioxide (WO_3). However, intermediate compositions ($\text{WO}_{2 < x < 3}$) are also known, which are characteristically blue in colour. WO_3 is composed of octahedral WO_6 units connected through corner oxygen atoms. When oxygen is removed from WO_3 , the WO_6 units share two corner atoms creating a connection along an edge. The blue colouration of WO_x originates from charge transfer transitions between W^{6+} - W^{5+} and W^{5+} - W^{4+} sites.^[74-76] As oxygen stoichiometry has a large impact on the material band gap and electron mobility, this tendency to form oxygen-deficient phases makes tungsten oxide highly tunable for applications such as gas sensor technology,^[77-79] electrochromic devices,^[80,81] low temperature fuel cells^[44,45] and photocatalysis.^[82,83]

A number of factors make tungsten oxide a promising catalyst support for polymer electrolyte fuel cells (PEFCs).^[84] Tungsten oxides readily form hydrates ($\text{WO}_3 \cdot x\text{H}_2\text{O}$) and are therefore effective proton conductors,^[85,86] which is an advantage for PEFCs. Furthermore, tungsten oxides have improved tolerance toward common fuel stream contaminants such as CO and H_2S .^[55] During oxygen reduction, hydrogen peroxide can be formed by the two-electron re-

duction of O_2 . This is disadvantageous for PEFCs as H_2O_2 can degrade fuel cell components.^[87] Interestingly, tungsten oxide has been shown to trigger decomposition of the undesirable hydrogen peroxide.^[88] However, as any catalyst support must have a minimal conductivity of 0.1 S.cm^{-1} for PEFC applications,^[38] increasing tungsten oxide conductivity remains of high importance.

Alongside its application in electrochemical systems such as PEFCs, tungsten oxide has been applied in a variety of photocatalytic reactions including water oxidation^[89–92] and the degradation of organic molecules.^[82,93] Oxygen defects have also been shown to decrease the band gap of wide-band gap semiconductors like ZnO .^[94,95] As tungsten oxide is known to form substoichiometric compositions containing oxygen defects, the band gap could be narrowed further, facilitating the formation of electron-hole pairs even with lower energy light sources. Changes in particle size and shape are known to influence photocatalysis.^[90,93,96–98] Consequently, the investigation of different synthetic routes to oxygen deficient tungsten oxide, with a focus of controlling morphology, is of high interest in this field.

Due to this variety of applications, the development of various synthetic routes to tungsten oxide, as well as an understanding of the influence of synthetic parameters, is vital.^[99] Previously mesoporous tungsten oxide was prepared by a sol-gel route, where WCl_6 was reacted with different alcohols in the presence of steam.^[100] Non-hydrolytic sol-gel (NHSG) is an alternative route to metal oxides that uses anhydrous organic alcohols or aprotic oxygen donors.^[101] This approach offers many advantages, including the ability to control oxide particle size and shape by the nature of oxygen donor. In addition, slower reaction rates for NHSG often lead to crystalline materials.^[42] A variety of publications have discussed how the alteration of NHSG reaction conditions can affect the resulting oxide morphology.^[102,103] Mesoporous blue tungsten oxide was prepared by reaction of WCl_6 in a 1-butanol/tert-butanol mixture, where the alcohol ratio influences porosity.^[102] The investigation of precursor influences on morphology has also shown some interesting results, where the use of $W(Oi-Pr)_6$ ^[79] or WCl_6 ^[103] in combination with benzyl alcohol provided nanowires or nanoplatelets, respectively. In the latter reported case, the addition of 4-tert-butylcatechol triggered the formation of rod-like structures.^[103] In place of alcohols, diisopropyl ether has been found to be a very efficient aprotic oxygen donor, which reacts with metal chlorides to yield a broad range of metal oxides^[43,104–108] including homogeneous mixed oxides.^[104,109,110] The preparation of pure tungsten oxide from WCl_6 and diisopropyl ether has been reported, although this route involves highly toxic CS_2 solvent.^[111] Therefore, there is clearly a need for the investigation of alternative routes. Outside of the initial preparation method, post-synthetic treatments under nitrogen gas at temperatures of

300 °C and above have been shown to significantly improve the electrical conductivity of blue tungsten oxides.^[102]

As presented above, tungsten oxides have a variety of technological applications. Moreover, the possibility to tune properties through varying oxygen stoichiometry and morphology provides the motivation to investigate the preparation of reduced tungsten oxides. The preparation of oxides by non-hydrolytic sol-gel is thought to give enhanced control over particle size and shape. Whilst some studies have covered the effect of tungsten precursor ligands on particle morphology, the effect of tungsten oxidation state is yet to be investigated. Building upon previous work where diisopropyl ether is used as an oxygen donor,^[112] reduced tungsten oxides (WO_x) are prepared from W(VI) and W(IV) chloride precursors. The effect of post-synthetic treatment in nitrogen atmosphere is also discussed. X-ray diffraction, microscopy and X-ray absorption studies, amongst other techniques, are used to characterise these materials and reveal the effect of oxidation state on both phase and morphology. The stability of reduced tungsten oxide in PEFC conditions is discussed and rationalised with respect to oxygen stoichiometry. Furthermore, the performance of these materials in photocatalytic oxygen evolution is discussed and compared to commercial WO_3 .

2.3 Results and Discussion

2.3.1 Precursor Effect on Phase and Morphology

The reaction of WCl_6 and WCl_4 (DME) (DME = dimethoxyethane) precursors with an excess of diisopropyl ether in 1,2-dichloroethane at 180 °C yielded blue tungsten oxide powders noted as $\text{WO}_{x(\text{VI})}$ and $\text{WO}_{x(\text{IV})}$ respectively. The blue colouration of $\text{WO}_{x(\text{VI})}$ and $\text{WO}_{x(\text{IV})}$ is a clear indication of the presence of oxygen defects and electron rich tungsten centers.^[74–76] Initial characterisation by elemental analysis (Table 2) reveals carbon and chlorine containing residuals remain on the oxide after synthesis, which is consistent with previous reports of similar synthetic routes.^[112]

Table 2: Elemental analysis results of $\text{WO}_{x(\text{VI})}$ and $\text{WO}_{x(\text{IV})}$; W, C, Cl and N content (wt%)

Material	W	C	Cl	N
$\text{WO}_{x(\text{VI})}$	78.6	0.13	0.17	< 0.2
$\text{WO}_{x(\text{IV})}$	78.3	0.87	1.55	< 0.2

The surface areas of both powders, as determined by N_2 adsorption-desorption measurements analysed with Brunauer-Emmett-Teller (BET) theory, are comparable with $85 \text{ m}^2.\text{g}^{-1}$ for $\text{WO}_{x(VI)}$ and $90 \text{ m}^2.\text{g}^{-1}$ for $\text{WO}_{x(IV)}$. Figure 3 shows adsorption-desorption isotherms corresponding to a typical type II case where porosity originates from inter-particle space rather than intra-particle porosity. However, it is clear that the isotherms are not identical. An increase in absorbed volume (V_a) at low, medium and high relative pressure (p/p_0) indicates the presence of micro-, meso- and macropores. Therefore the isotherm shapes indicates that $\text{WO}_{x(VI)}$ has a significant amount of macropores in comparison to $\text{WO}_{x(IV)}$.

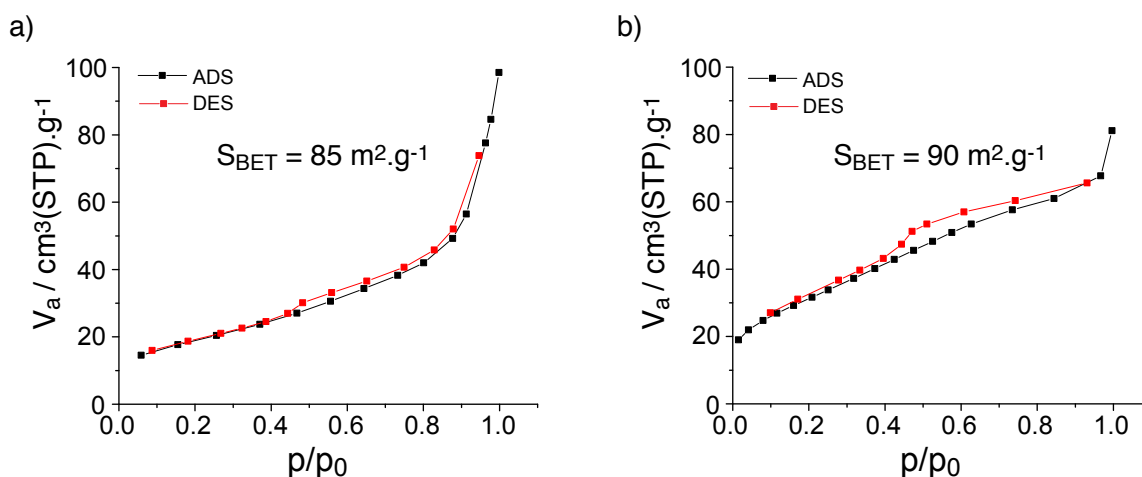


Figure 3: N_2 adsorption-desorption isotherms of $\text{WO}_{x(VI)}$ (a) and $\text{WO}_{x(IV)}$ (b).

Powder X-ray diffraction (XRD) shows phase differences between these two materials (Figure 4). The diffraction pattern of $\text{WO}_{x(VI)}$ is consistent with tetragonal WO_3 , whilst $\text{WO}_{x(IV)}$ could be assigned to multiple oxygen deficient phases such as $\text{WO}_{2.65}$, $\text{W}_{18}\text{O}_{49}$ and $\text{WO}_{2.90}$. Considering the blue colour of $\text{WO}_{x(VI)}$ is consistent with oxygen deficient tungsten oxide, it is suggested that this material contains defects, which are low in concentration and randomly distributed. In contrast, $\text{WO}_{x(IV)}$ likely contains a higher concentration of defects, which form ordered arrays influencing the oxide unit cell. Whilst the exact phase assignment of $\text{WO}_{x(IV)}$ is hindered by both the broad diffraction peaks from the nanoparticulate sample and the diffraction similarity of these oxygen deficient phases; this study clearly demonstrates that a more reduced (or oxygen deficient) phase of tungsten oxide is formed from $\text{WCl}_4(\text{DME})$.

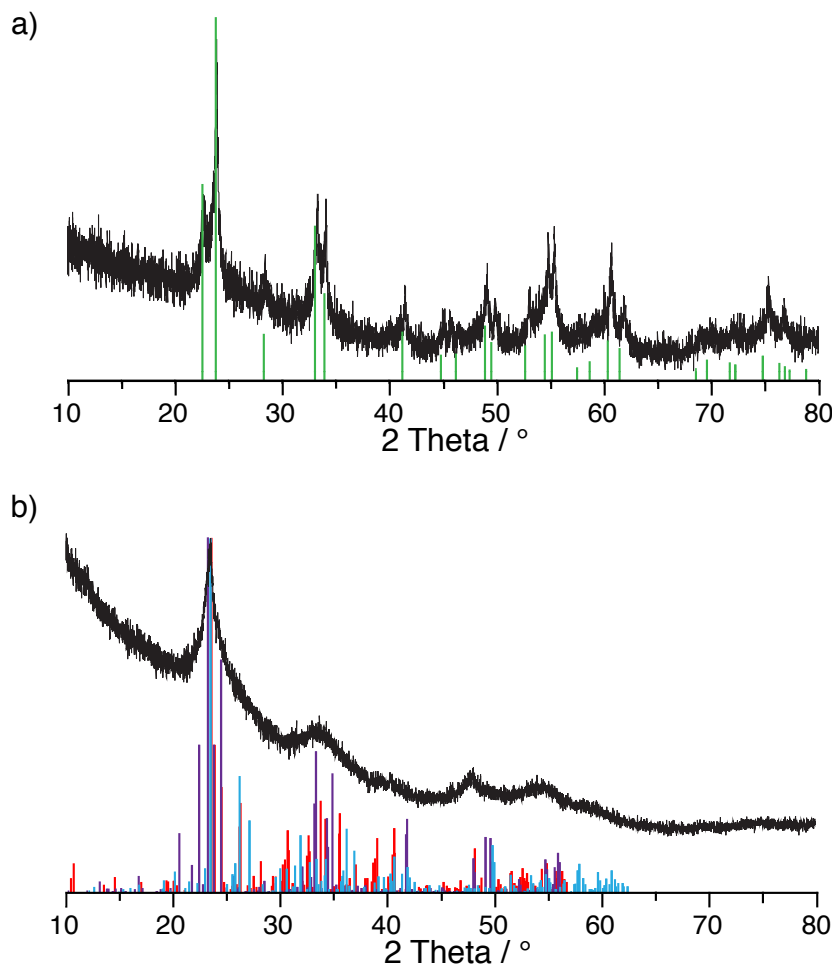


Figure 4: XRD powder diffraction patterns of $\text{WO}_{x(VI)}$ (a) and $\text{WO}_{x(IV)}$ (b) with reference powder diffraction patterns of tetragonal WO_3 (green, ICDD 00-085-0808), $\text{WO}_{2.63}$ (purple, ICDD 00-081-1172), $\text{W}_{18}\text{O}_{49}$ (red, ICDD 084-1516) and $\text{WO}_{2.90}$ (light blue, ICDD 00-073-2182).

Characterisation by bright field transmission electron microscopy (TEM) imaging reveals notable differences between the powder morphologies, with $\text{WO}_{x(VI)}$ and $\text{WO}_{x(IV)}$ being composed of cube-like and rod-like nanoparticles respectively (Figure 5). Similar switches in morphology have been reported in the presence of catechol ligands.^[103] As the influence of dimethoxyethane is assumed to be negligible in view of the excess diisopropyl ether, this shape change is thought to be triggered by the change in precursor oxidation state. XRD characterisation has suggested the formation of ordered defect arrays within $\text{WO}_{x(IV)}$. With this in mind, it is proposed that the formation of such ordered defects, which can be columnar in the case of $\text{W}_{18}\text{O}_{49}$, triggers growth of the nanoparticle along one axis to form rod-shape particles.

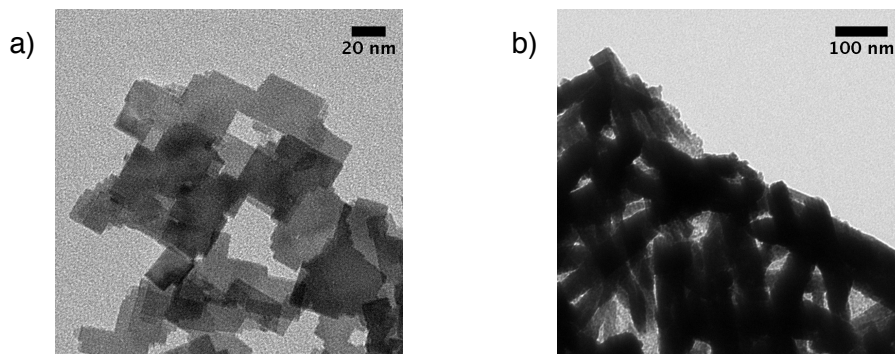


Figure 5: Bright field TEM images of WO_{x(VI)} (a) and WO_{x(IV)} (b).

To further probe the reduced nature of these materials, they were characterised by electron paramagnetic resonance (EPR) and X-ray absorption near edge structure (XANES) spectroscopy. Figure 6 shows two signals are observed in the EPR spectra of WO_{x(VI)} and WO_{x(IV)} around $g = 2.0$ and $g = 1.8$. The sharp signal at $g = 2.0$ is similar to those typically observed for organic radical species and is consequently assigned to organic functionalities remaining on the oxide surface after NHSG synthesis.^[112] The broad signal at $g = 1.8$ is assigned to W(V) centers, which supports the reduced nature of these blue oxide materials.^[113]

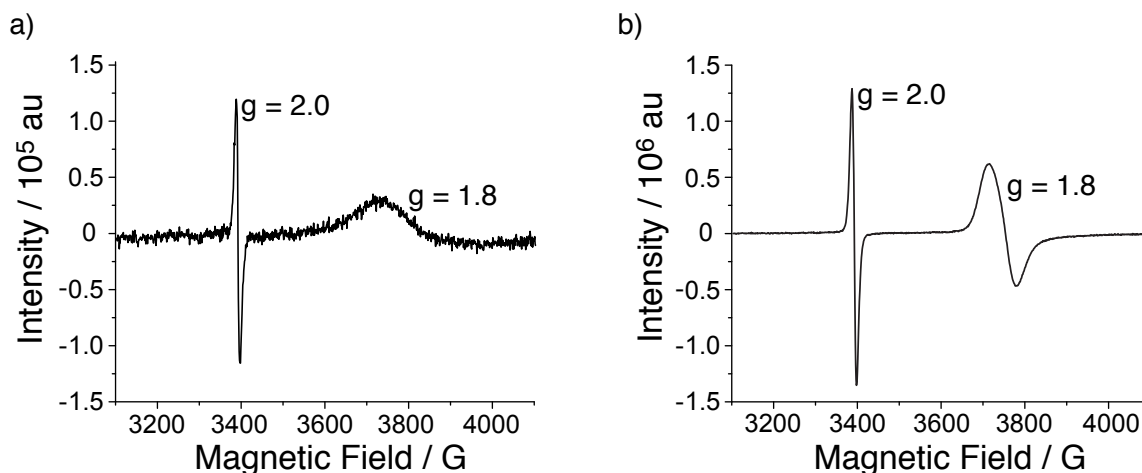


Figure 6: EPR spectra of WO_{x(VI)} (a) and WO_{x(IV)} (b) recorded at 110 K.

Figure 7 shows the X-ray absorption near edge structure (XANES) spectra for WO_{x(VI)} and WO_{x(IV)} in comparison to commercial WO₃ and WO₂. XRD characterisation of the commercial samples can be found in Appendix 1. Although the XRD pattern of commercial WO₂ shows some phases other than WO₂ (likely WO_{2<x<3}), WO₂ appears to be the majority phase (Figure A3). Table 3 details the white line energies of the WO_x samples. From this comparison it is

clear that the white line energies of both $\text{WO}_{x(VI)}$ and $\text{WO}_{x(IV)}$ are shifted to lower values with respect to WO_3 by -0.35 and -0.75 eV respectively. Although these energy shifts are relatively small, they are sufficient to show that $\text{WO}_{x(VI)}$ and $\text{WO}_{x(IV)}$ are reduced with respect to bulk WO_3 .^[114] These results are in good agreement with the XRD and EPR results.

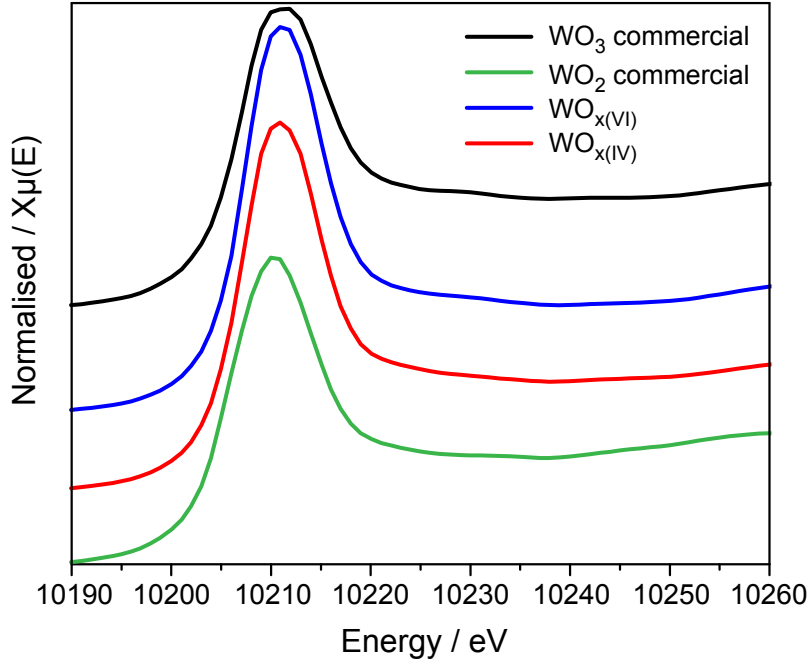


Figure 7: XANES characterisation of tungsten oxides.

Table 3: White Line Energies of the WO_x materials (commercial materials denoted by *)

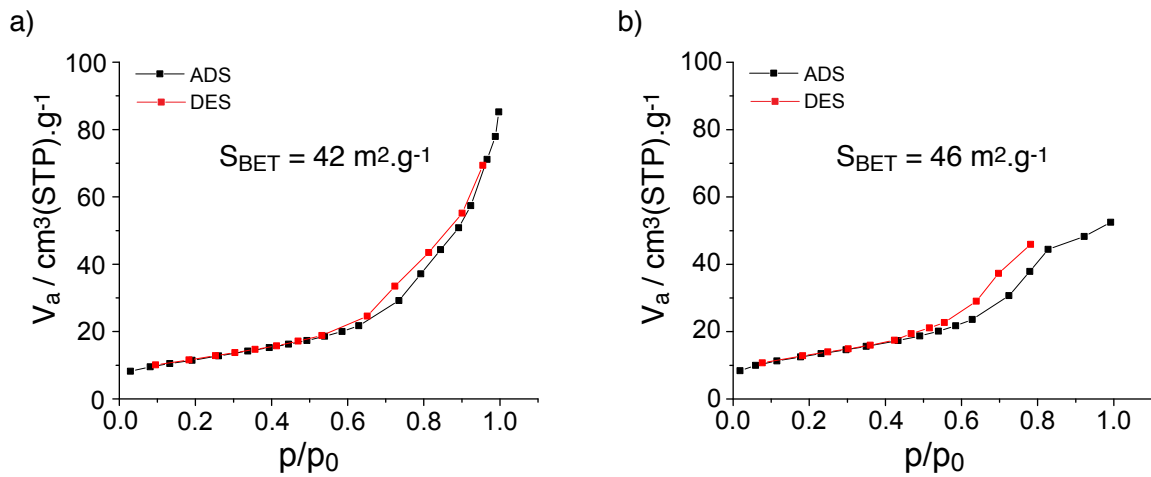
Material	White Line Position / eV
WO_3^*	100211.56
$\text{WO}_{x(VI)}$	10211.21
$\text{WO}_{x(IV)}$	10210.81
WO_2^*	10210.34

To investigate further changes in morphology and phase, $\text{WO}_{x(VI)}$ and $\text{WO}_{x(IV)}$ were treated under flowing N_2 at 500 °C for 3 h. This treatment yields intensely coloured dark blue powders which are subsequently noted as $\text{WO}_{x(VI)-\text{N}_2}$ and $\text{WO}_{x(IV)-\text{N}_2}$. Table 4 shows that chlorine content is significantly reduced for both nitrogen treated materials, while carbon contamination is only marginally decreased in the case of $\text{WO}_{x(IV)-\text{N}_2}$.

Table 4: Elemental analysis results of $\text{WO}_{x(VI)}$ and $\text{WO}_{x(IV)}$ after N_2 treatment; W, C, Cl and N content (wt%)

Material	W	C	Cl	N
$\text{WO}_{x(VI)-\text{N}_2}$	79.1	0.14	< 0.1	< 0.2
$\text{WO}_{x(IV)-\text{N}_2}$	79.9	0.67	0.11	< 0.2

Nitrogen adsorption-desorption measurements analysed with BET theory show that the BET surface areas of both samples have reduced by approximately 50% after nitrogen treatment at high temperature, to $42 \text{ m}^2 \cdot \text{g}^{-1}$ for $\text{WO}_{x(VI)-\text{N}_2}$ and $46 \text{ m}^2 \cdot \text{g}^{-1}$ for $\text{WO}_{x(IV)-\text{N}_2}$. This decrease in surface area is likely due to particle sintering during this post-synthetic treatment. It is important to note that the type II adsorption-desorption isotherms remain (Figure 8) and are similar in shape to those measured for the as-prepared analogs (Figure 3). TEM images shown in Figure 9 reveal that the edges of the cube-like particles of $\text{WO}_{x(VI)}$ have softened and the particles have sintered, whilst the rod-shape particles of $\text{WO}_{x(IV)}$ have decreased in width. The decrease in surface area for $\text{WO}_{x(IV)-\text{N}_2}$ suggests that the particles have overall increased in size, although this is hard to corroborate from these TEM images.

**Figure 8:** N_2 adsorption-desorption isotherms for $\text{WO}_{x(VI)-\text{N}_2}$ (a) and $\text{WO}_{x(IV)-\text{N}_2}$ (b).

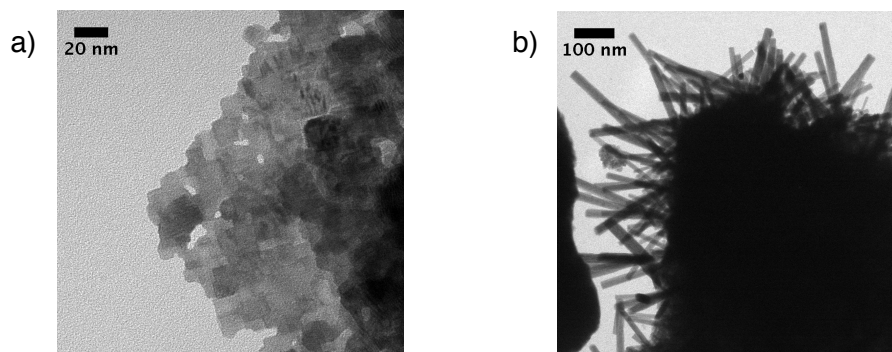


Figure 9: Bright Field TEM images of $\text{WO}_{x(\text{VI})-\text{N}_2}$ (a) and $\text{WO}_{x(\text{IV})-\text{N}_2}$ (b).

Powder XRD characterisation of $\text{WO}_{x(\text{VI})-\text{N}_2}$ indicates that the WO_3 phase is maintained however, a phase transition from tetragonal to monoclinic WO_3 has occurred. A similar phase transformation to monoclinic WO_3 has been reported when hexagonal WO_3 is annealed above 400 °C.^[115] In the case of $\text{WO}_{x(\text{IV})-\text{N}_2}$ no significant phase change is observed as a result of N_2 treatment. This assignment is similarly complicated by the broad diffraction peaks and the occurrence of multiple oxygen deficient tungsten oxide phases. However these results do show that this sample remains oxygen deficient after N_2 treatment.

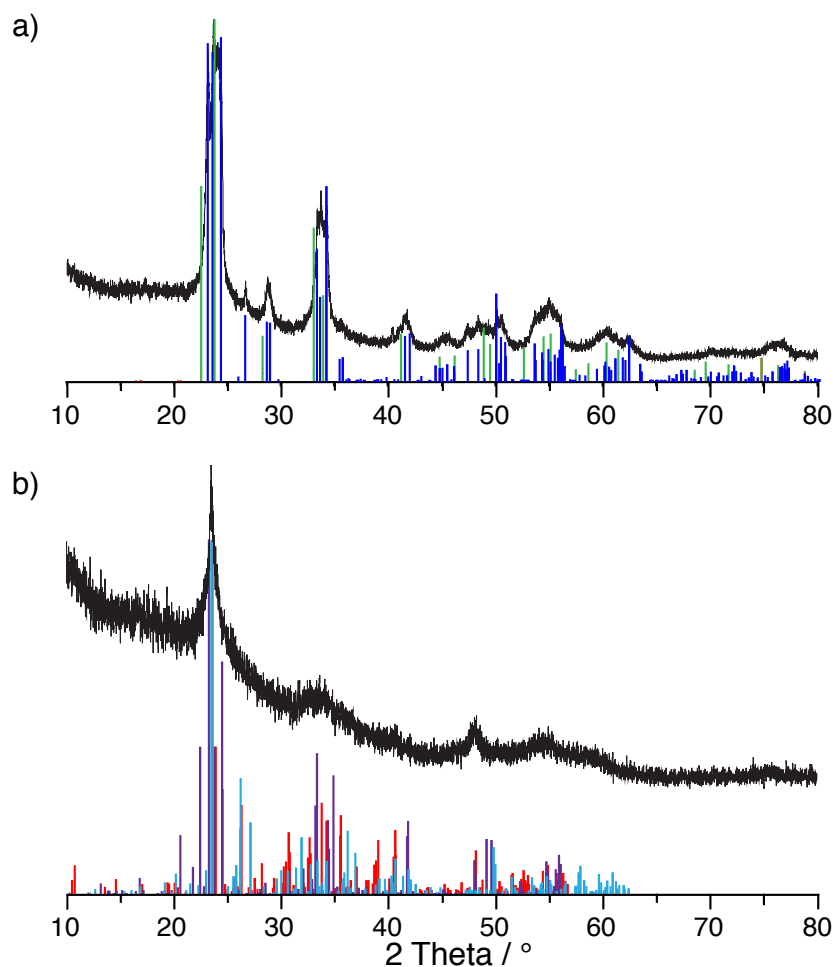


Figure 10: XRD powder diffraction patterns of $\text{WO}_{x(\text{VI})-\text{N}_2}$ (a) and $\text{WO}_{x(\text{IV})-\text{N}_2}$ (b) with reference powder diffraction patterns of tetragonal WO_3 (green, ICDD 00-085-0808), monoclinic WO_3 (dark blue, ICDD 00-083-0951), $\text{WO}_{2.63}$ (purple, ICDD 00-081-1172), $\text{W}_{18}\text{O}_{49}$ (red, ICDD 00-084-1516) and $\text{WO}_{2.90}$ (light blue, ICDD 00-073-2182).

Interestingly, the EPR spectra of the materials after N_2 treatment show a single sharp signal at $g = 2.0$ (Figure 11). This signal is assigned to organic radicals on the support surface, which is supported by the carbon content determined by elemental analysis. Colouration and XRD analysis indicate that these materials remain oxygen deficient, however there is an absence of any EPR signal consistent with the presence of W(V) centers. Therefore it is postulated that the EPR signal of W(V) species of both $\text{WO}_{x(\text{VI})-\text{N}_2}$ and $\text{WO}_{x(\text{IV})-\text{N}_2}$ is reduced due to fast spin relaxation, perhaps as a result of increasing defect concentration.

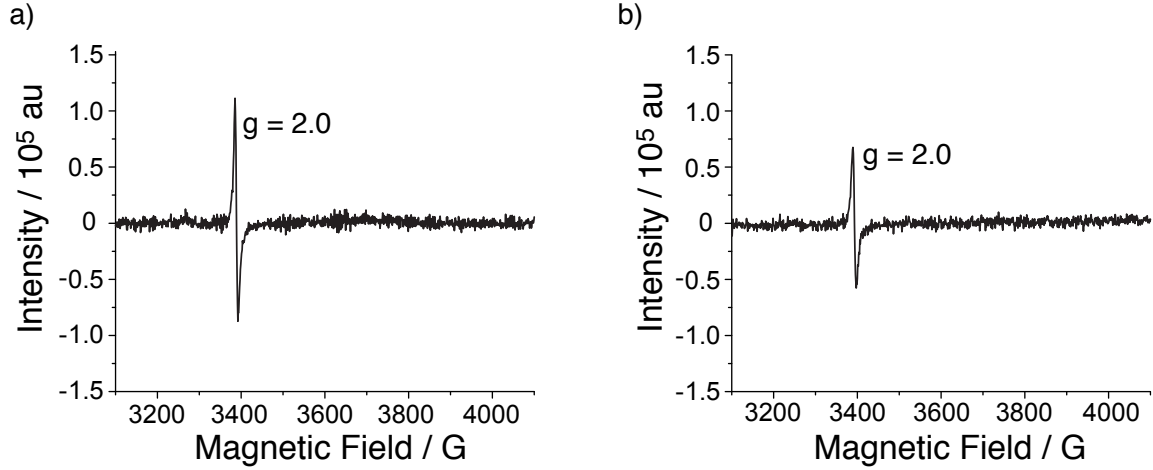


Figure 11: EPR spectra of $\text{WO}_{x(\text{VI})-\text{N}_2}$ (a) and $\text{WO}_{x(\text{IV})-\text{N}_2}$ (b) recorded at 110 K.

Electrical conductivities of all WO_x materials were measured by standard 4-point probe method using compressed powder samples with thicknesses between 100 and 1000 μm . The conductivity of three compressed disks were measured and averaged to give the values reported herein. Table 5 displays the electrical conductivity of commercial WO_3 as well as the WO_x materials before and after N_2 treatment. From these results it is clear that the blue tungsten oxides have an enhanced electrical conductivity in comparison to yellow WO_3 , which is explained by the formation of oxygen defects. Additionally there is a significant increase in conductivity after N_2 treatment at 500 $^\circ\text{C}$. This increase may be triggered by a number of factors. Firstly, surface area measurements indicated a decrease in surface area after this post-synthetic treatment, this likely contributes to increasing conductivity by effectively decreasing the number of particle-particle boundaries, which are expected to be highly resistant to electron flow. Secondly, the more intense blue colouration after N_2 treatment indicates an increased amount of oxygen defects, which likely results in an increased carrier concentration.^[74–76]

Table 5: Electrical Conductivity of the WO_x materials (commercial materials denoted by *)

Material	Electrical Conductivity (σ) / S.cm^{-1}
WO_3^*	$4.5 \cdot 10^{-7}$
$\text{WO}_{x(\text{VI})}$	$1.5 \cdot 10^{-4}$
$\text{WO}_{x(\text{IV})}$	$1.0 \cdot 10^{-4}$
$\text{WO}_{x(\text{VI})-\text{N}_2}$	$4.1 \cdot 10^{-3}$
$\text{WO}_{x(\text{IV})-\text{N}_2}$	$4.0 \cdot 10^{-2}$

In summary the preparation of high surface area blue tungsten oxides with varied morphologies and phases has been reported. The reaction of WCl_6 with diisopropyl ether yields cube-like particles, whilst the reaction of WCl_4 (DME) under the same conditions yields rod-like structures. XRD indicates that $\text{WO}_{x(\text{IV})}$ is more oxygen deficient than $\text{WO}_{x(\text{VI})}$ and it is postulated that the formation of columnar defect structures triggers the growth of rod shape particles. Nitrogen treatment causes a decrease in surface area and a tetragonal to monoclinic phase shift for $\text{WO}_{x(\text{VI})}$. An increase in conductivity is observed with N_2 treatment, in agreement with literature,^[102] likely due to increasing oxygen defects. For discussion of the UV-vis spectra of these materials, see the section dedicated to photocatalytic activity.

2.3.2 Electrochemical Stability

The electrochemical stability of $\text{WO}_{x(\text{IV})}$ was evaluated using cyclic voltammetry with rotating disk electrode (RDE) experiments. For this investigation, $\text{WO}_{x(\text{IV})}$ was combined with Nafion[®] to form an ink, which was deposited onto a glassy carbon electrode. Cyclic voltammetry involves linearly varying the electrode potential and recording current as a function of potential. Considering the acidic environment of PEFCs, 0.1 M aqueous HClO_4 saturated with N_2 was used as an electrolyte. Cyclic voltammograms (CVs) were recorded before and after two degradation cycling regimes, which involved cycling the potential between 0 and 1 V as well as 0.5 and 1.5 V. These two ranges were chosen to investigate both the low and high potential stability of $\text{WO}_{x(\text{IV})}$, correlating to the anodic and cathodic electrodes of PEFCs. In addition to cyclic voltammetry, X-ray photoelectron spectroscopy (XPS) was used to investigate the variation in tungsten oxidation state before and after potential cycling.

Low potential stability was tested by recording CVs before and after 1000 cycles between 0 and 1 V. Figure 12 shows the cyclic voltammogram of $\text{WO}_{x(\text{IV})}$ has a drop in current density (j) after cycling. This CV shrinkage may be explained by a drop in conductivity or dissolution of the electrode material in the acidic electrolyte. XPS spectra acquired before and after cycling show three peaks at 37.7, 35.7 and 33.9 eV, which are assigned to WO_3 ($4f_{5/2}$), $\text{WO}_{2 < x < 3}$ ($4f_{7/2}$) and/or WO_3 ($4f_{7/2}$) and $\text{WO}_{2 < x < 3}$ ($4f_{5/2}$) and/or WO_2 ($4f_{5/2}$) respectively.^[116] Looking more closely at the spectra, there is a clear increase in the high energy peak, WO_3 ($4f_{5/2}$), indicating mild oxidation of the material, which could explain the observed decrease in current.

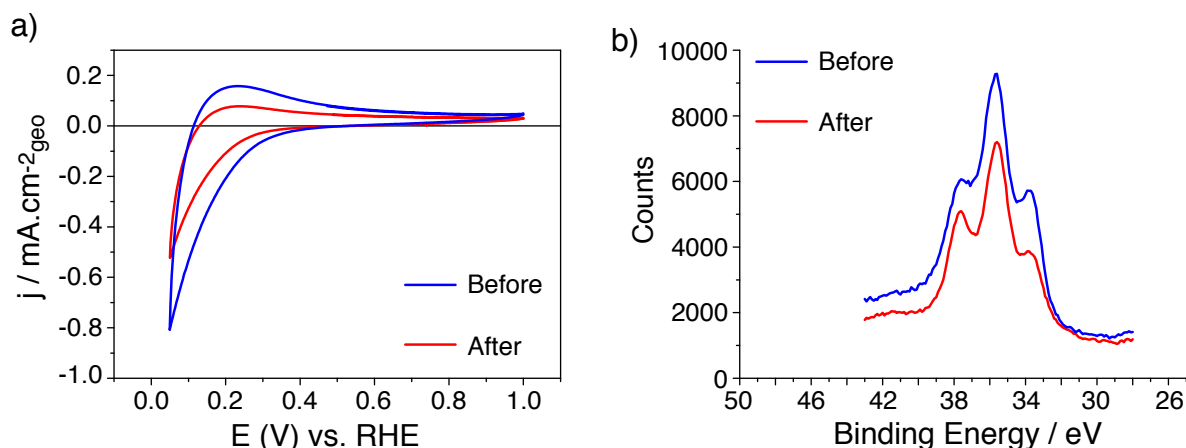


Figure 12: Cyclic voltammograms (a) and XPS spectra (b) of $\text{WO}_{x(IV)}$ recorded before and after stability tests at low potential.

Similarly, high potential stability was tested by cycling 1000 times between 0.5 and 1.5 V. The CVs recorded before and after cycling shows CV shrinkage, which may be due to a decrease in conductivity or material dissolution (Figure 13). Analysis by XPS shows the three peaks assigned as for the low potential stability test described above. Comparing the XPS spectra before and after the stability test at high potential, there is a considerable increase in the peaks assigned to WO_3 , indicating dramatic oxidation of $\text{WO}_{x(IV)}$. Therefore, the drop in current density likely arises from the reduced conductivity of oxidised $\text{WO}_{x(IV)}$.

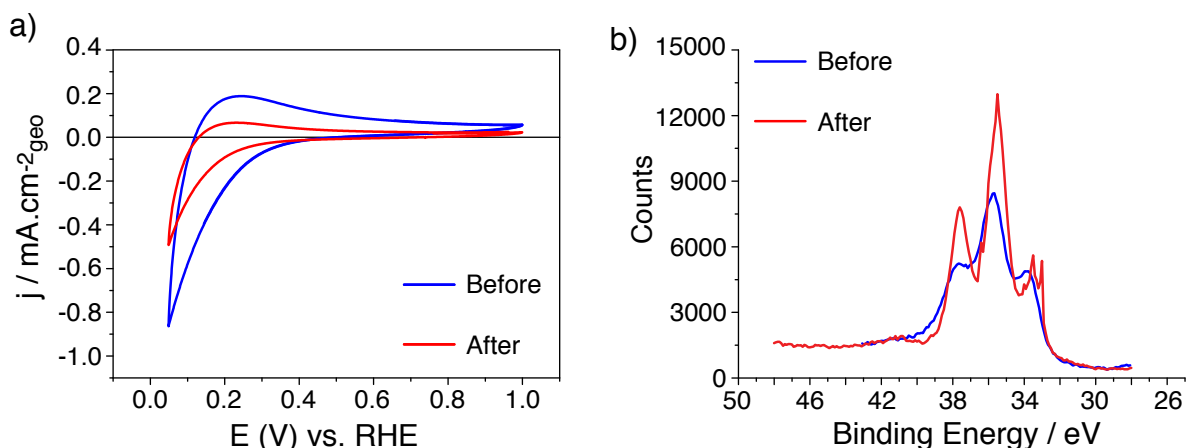


Figure 13: Cyclic voltammograms (a) and XPS spectra (b) of $\text{WO}_{x(IV)}$ recorded before and after stability tests at high potential.

The results of the electrochemical stability tests show that $\text{WO}_{x(IV)}$ oxidises under both low and high potential cycling regimes, with oxidation being more pronounced after cycling at

high potentials. This investigation shows that whilst oxygen vacancies can trigger considerable increases in oxide conductivity, these vacancies can be easily filled during potential cycling even in oxygen free electrolyte. This oxidation contributes to a decrease in electronic conductivity, which would greatly impact PEFC operation.

2.3.3 Photocatalytic Activity

Tungsten oxides have alternative applications as photocatalysts for oxygen evolution.^[89–92] The activity of heterogeneous photocatalysts depends on two major factors, the rate of electron-hole pair formation and the rate of electron-hole pair recombination.^[117] As electron-hole pairs are formed through the promotion of an electron from the valence band to the conduction band, the optical band gap energy can influence the generation of electron-hole pairs. Therefore these materials were characterised by UV-vis diffuse reflectance spectroscopy (UV-vis DRS). Figure 14 shows the spectra from UV-vis DRS measurements of both as-prepared and N₂ treated WO_x samples in comparison to commercial WO₃. Characterisation of the commercial WO₃ sample can be found in Appendix 1.

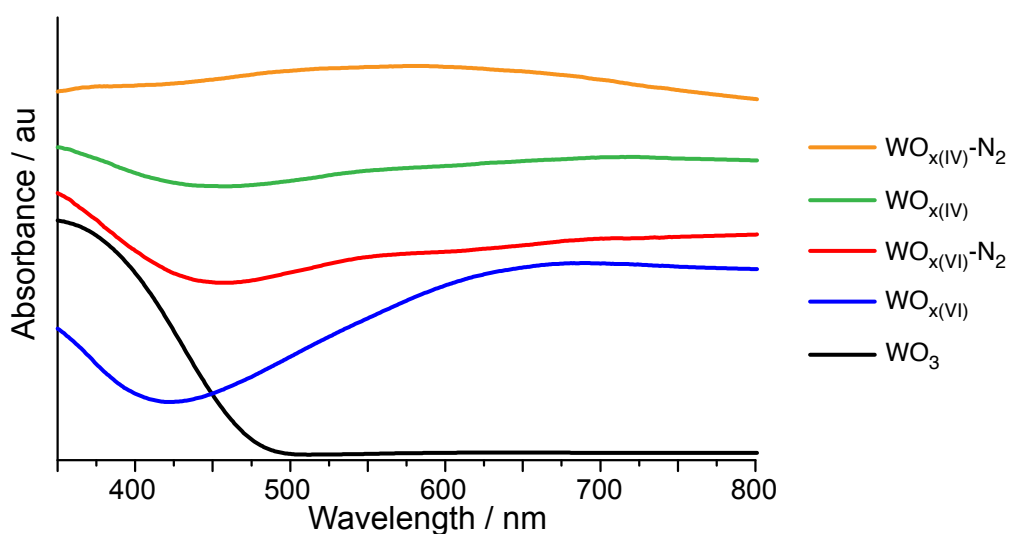


Figure 14: UV-vis DRS spectra of tungsten oxides.

The direct interpretation of UV-vis spectra of tungsten oxide materials is complicated by a number of factors. In general, the UV-vis spectra of nanomaterials can vary depending on the particle size and shape.^[118] Additionally, the UV-vis spectra of WO_x materials are sensitive to the distortion of WO₄ and WO₆ units and the presence of multiple structures can result in overlapping bands, which are difficult to distinguish.^[119] The absorption band at 500 - 800

nm distinguishes both the as-prepared and N₂ treated sol-gel materials from commercial WO₃. Absorptions in this wavelength region are commonly associated with oxygen defects,^[113] which is in agreement with the XRD, EPR and XANES characterisation discussed previously. The band gap energies of these materials was approximated from the deflection point of the UV-vis spectra and these values are compared in Table 6. It should be noted that the UV-vis spectra of WO_{x(IV)-N2} appears to be composed of several overlapping peaks, which complicates band gap approximation.

Table 6: Approximate band gap energies of the WO_x materials (commercial materials denoted by *)

Material	Band Gap / eV
WO ₃ *	2.6
WO _{x(VI)}	3.0
WO _{x(VI)-N2}	2.8
WO _{x(IV)}	2.8
WO _{x(IV)-N2}	-

In general, these results show that all WO_x materials have a higher energy optical band gap than WO₃, seemingly contradicting literature reporting the band gap reducing nature of the oxygen defects.^[94,95] However, as mentioned earlier, direct comparisons are complicated considering the vast differences in particle size and shape. Interestingly, similar trends between the UV-vis spectra of WO₃ and WO_x materials have been observed in literature, in these cases the morphologies of the two samples were also significantly different.^[120] Nonetheless a comparison can be made between WO_{x(VI)} before and after N₂ treatment. Here, there is a noted decrease in band gap energy after N₂ treatment, which would be consistent with an increase amount of oxygen defects.

The performance of these materials in photocatalytic oxygen evolution was tested under UV irradiation and compared to commercial WO₃ (Figure 15). The commercial WO₃ sample has the highest activity of 5.3·10⁻³ mol.min⁻¹.g⁻¹ after 1.2 h of irradiation. N₂ treatment has a positive effect on activity, with both WO_{x(VI)-N2} and WO_{x(IV)-N2} outperforming WO_{x(VI)} and WO_{x(IV)}. Furthermore, WO_{x(VI)-N2} reaches a higher activity than WO_{x(IV)-N2}, with a similar trend observed between WO_{x(VI)} and WO_{x(IV)}. Interestingly, both N₂ treated samples maintain higher oxygen evolution activities than WO₃ after 3 h.

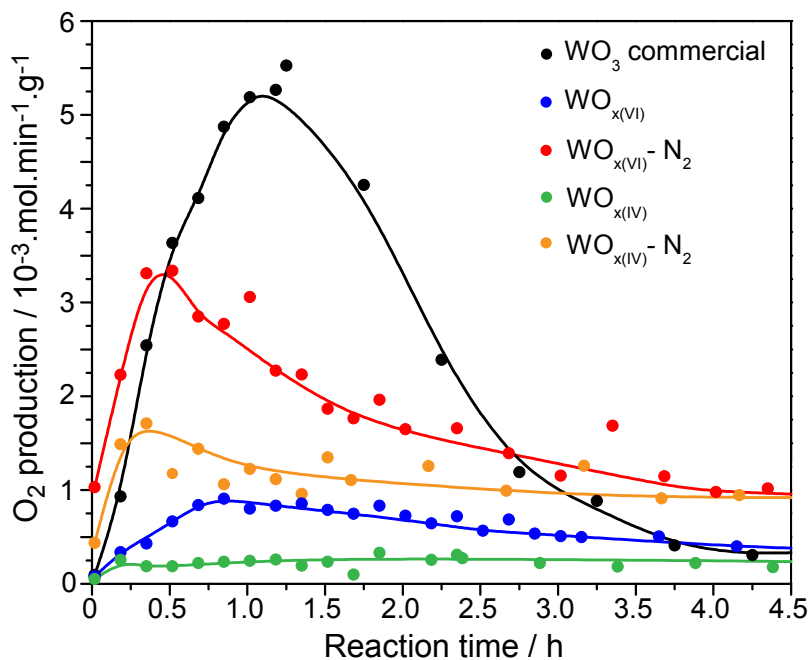


Figure 15: Photocatalytic oxygen evolution activity of tungsten oxides.

A variety of factors contribute to the observed photocatalytic activities of WO_3 and the WO_x materials. The lower band gap energy of WO_3 , likely contributes to its increased activity. This can also be concluded for $\text{WO}_{x(\text{VI})-\text{N}_2}$, which has a slightly smaller band gap than $\text{WO}_{x(\text{VI})}$, but greater photocatalytic activity. The lower activity of all WO_x materials with respect to WO_3 can be explained by two main factors, oxygen stoichiometry and particle size. Oxygen defects are known to act as electron-hole recombination sites.^[121] As maintaining electron-hole separation is key to photocatalytic activity, the oxygen deficiency of the WO_x materials probably contributes towards their low photocatalytic activity. Furthermore, WO_x materials have smaller particle sizes than WO_3 and as electron-hole recombination rates are known to increase for small particle sizes, this further justifies their decreased activity.^[90] In addition to their small particle size and oxygen deficiency, the likely presence of organic functionalities on the oxide surface may also contribute to reduced activity.^[122] Although EPR spectroscopy provided little justification for the presence of W(V) centers in WO_{x-N_2} , electrical conductivity measurements indicate these materials remain oxygen deficient after N_2 treatment. From this information and the known influence of oxygen defects on electron-hole recombination, a reduction in photocatalytic activity would be expected for WO_{x-N_2} . However, an increase in activity is observed for both WO_{x-N_2} materials. TEM imaging and surface area measurements indicate the WO_x particles increase in size after N_2 treatment, which due to lower rates of electron-hole recombination, supports the observed increase in activity after N_2 treatment. Interestingly, $\text{WO}_{x(\text{VI})}$ and $\text{WO}_{x(\text{VI})-\text{N}_2}$ show improved photocatalytic activities with respect to $\text{WO}_{x(\text{IV})}$ and

$\text{WO}_{x(\text{IV})-N_2}$. This can be explained by the lower concentration of oxygen defects in $\text{WO}_{x(\text{VI})}$ and $\text{WO}_{x(\text{VI})-N_2}$, shown by X-ray diffraction. The larger increase in activity for $\text{WO}_{x(\text{VI})-N_2}$ is attributed to the tetragonal-monoclinic transformation, as monoclinic WO_3 is known to have a higher activity towards oxygen evolution than other WO_3 phases.^[123]

2.4 Conclusion

The variety of potential applications for substoichiometric tungsten oxides has triggered an interest in developing different synthetic approaches to prepare such materials. Considering the importance of particle size and shape in many applications, the influence of synthetic parameters on these properties is of particular interest. Whilst several studies have investigated the influence of synthetic parameters for sol-gel prepared tungsten oxides, to the author's knowledge this is the first report of precursor oxidation state effects on WO_x phase and morphology.

High surface area tungsten oxide materials with varying morphologies have been prepared from W(VI) and W(IV) chloride precursors. XRD, EPR, XANES and UV-vis DRS measurements confirm the oxygen deficient nature of the yielded powders, which have significantly higher electronic conductivities in comparison to commercial WO_3 . TEM and XRD characterisation show that both morphology and phase are precursor dependent, with cubic and rod-shaped particles formed with WCl_6 and $\text{WCl}_4(\text{DME})$ respectively. In the case of $\text{WCl}_4(\text{DME})$ the formation of rod-shaped particles can be rationalised by the formation of ordered columnar oxygen defects, as is known for $\text{W}_{18}\text{O}_{49}$. Treating the as-prepared materials under N_2 at 500 °C resulted in a decrease in surface area and increase in conductivity for both $\text{WO}_{x(\text{VI})}$ and $\text{WO}_{x(\text{IV})}$. This increase in conductivity is attributed to increasing oxygen defects and increased particle size.

In line with the potential advantages of tungsten oxides in PEFCs, the stability $\text{WO}_{x(\text{IV})}$ under PEFC relevant conditions was tested using cycling voltammetry. Under both low and high potential cycling regimes, $\text{WO}_{x(\text{IV})}$ shows a drop in current likely due to oxidation of the sample as supported by XPS measurements. This demonstrates that whilst oxygen defects are able to trigger sufficient increases in electrical conductivity, they are easily filled under electrochemical conditions, even in oxygen free electrolyte.

Alternative applications for tungsten oxides includes photocatalytic oxygen evolution. Both as-synthesised and nitrogen treated WO_x samples showed lower oxygen evolution activity under UV irradiation in comparison to WO_3 . UV-vis spectroscopy showed that WO_3 has the smallest optical band gap, which is advantageous in photocatalysis. In addition, the oxygen vacan-

cies in the WO_x materials may act as electron-hole recombination sites, reducing photocatalytic activity. Interestingly both $\text{WO}_{x(VI)-N_2}$ and $\text{WO}_{x(IV)-N_2}$ samples have higher activities than their as-prepared counterparts, this can be explained by an increase in particle size, which can aid electron-hole separation. Furthermore, the tetragonal-monoclinic transformation upon nitrogen treatment of $\text{WO}_{x(VI)}$, results in a further activity increase. Both N_2 treated WO_x materials maintain a higher activity than WO_3 at long reaction times, showing the potential importance of post-synthetic treatment for the preparation of stable photocatalysts.

2.5 Experimental Details

2.5.1 General

All experiments were conducted under argon atmosphere using standard Schlenk and glove box techniques unless otherwise stated. Solvents were dried over an alumina column (MB SPS-800, MBraun), stored over 4 Å molecular sieves and degassed before use with the exception of 1,2-dichloromethane and diisopropyl ether, which were dried and distilled over CaH_2 and Na respectively. WCl_6 (99.99%) was purchased from Strem Chemicals. $\text{WCl}_4(\text{DME})$ was prepared according to literature.^[124] Digestion vessels from the Parr Instrument Company were used for NHSG synthesis. Commercial WO_3 and WO_2 were purchased from Sigma Aldrich. XRD diffractograms were recorded using a Stoe STADI P diffractometer (Cu $K\alpha$ radiation, $\lambda = 1.54051$ Å). TEM images were collected with a Philips CM12 transmission electron microscope. N_2 adsorption-desorption analysis was conducted using a BEL-Mini device supplied by BEL Japan Inc. with ca. 500 mg of each sample. Results were fitted using BEL-Master programme and BET theory. EPR samples were prepared in an Ar filled glove-box by suspending ca. 10 mg of solid in 0.5 mL toluene in a quartz Young EPR tube and freezing in liquid N_2 . Continuous Wave (CW) EPR spectra were recorded on a Bruker EMX X-Band spectrometer (9.5 GHz microwave frequency) at 110 K. Electrical conductivity values were determined from powder disks under 0.625 MPa pressure with thicknesses in the range 100 - 1000 μm . For commercial WO_3 conductivity values were determined using Electrical Impedance Spectroscopy. In the case of all other samples, chronoamperometric measurements were used; where the current was recorded for a range of voltages (0.001 - 0.1 V) and conductivity subsequently calculated using Ohm's law. Electrical conductivity was determined for three pellet thicknesses and averaged to give the values reported. UV-visible diffuse reflectance spectroscopy was conducted under ambient conditions using a Cary UV-vis-NIR spectrophotometer, for clarity the spectra were smoothed using the Smooth function of OriginPro program from OriginLab. For characterisations conducted under ambient conditions, samples were used immediately after removal

from the glove-box. Colour changes were not observed for any sample during analysis. XPS measurements were performed using a VG ESCALAB 220iXL spectrometer (Thermo Fischer Scientific) equipped with an Al Ka monochromatic source (spot size: 500 μm , power: 150 W) and a magnetic lens system. XANES measurements at W L_{III} -edge were performed at the SuperXAS beamline at the Swiss Light Source (Paul Scherrer Institute, Villigen, Switzerland). The SLS is a third generation synchrotron, which operates under top up mode, 2.4 GeV electron energy, and a current of 400 mA. The SuperXAS beamline is positioned on one of three super-bent ports. The incident beam was collimated by Si-coated mirror at 2.8 mrad, monochromatized using a double crystal Si(111) monochromator, and focused with Rh coated toroidal mirror (at 2.8 mrad) down to 100x100 μm . The beam intensity was of 4.5×10^{11} ph.s⁻¹. We collected XANES data in transmission mode at 298 K under Ar atmosphere.

2.5.2 Preparation of Blue Tungsten Oxides

In an Ar filled glove-box, WCl_6 (3.96 g, 0.01 mol) or $\text{WCl}_4(\text{DME})$ (4.05 g, 0.01 mol) was loaded into a digestion vessel with a capacity of 125 mL. 1,2-Dichloroethane (31 mL) was added, followed by excess diisopropyl ether (14 mL, 0.1 mol). After closing, the vessel was removed from the glove box and heated to 180 °C for 3 days using a conventional oven, then allowed to cool overnight. The blue solid obtained was filtered on a glass frit in air, washed with EtOH (3 x 20 mL) and dried overnight under high vacuum (10^{-5} mbar) at 140 °C. The solid was then stored in an Ar filled glove-box (2.0 g, ca. 85% yield).

2.5.3 Oxide Post-Synthetic Treatment

WO_x (ca. 2 g) was loaded into a gas flow reactor and heated to 500 °C ($2^\circ\text{C}.\text{min}^{-1}$) under N_2 flow ($120 \text{ mL}.\text{min}^{-1}$) and kept at this temperature for 3 h. The solid was then evacuated using high vacuum (10^{-5} mbar) and stored in an Ar filled glove-box.

2.5.4 Electrochemical Stability Tests

An ink was prepared by sonicating ultrapure water (1 mL), isopropanol (4 mL), Nafion[®] (20 μL) and $\text{WO}_{x(\text{IV})}$ (15 mg). Electrodes were prepared by dropping 4 x 5 μL ink solution onto a glass carbon rotating disk electrode. Each stability tests ere performed on freshly prepared electrodes. All stability tests were performed in 0.1 M HClO_4 electrolyte saturated with N_2 . All voltages are reported in comparison to the Reversible Hydrogen Electrode (RHE). Cyclic voltammograms were recorded between 0.05 and 1.0 V before and after the stability protocols.

Low potential stability tests involved 1000 potential cycles between 0.0 and 1.0 V at a rate of 50 mVs⁻¹. High potential stability tests involved 1000 potential cycles between 0.5 and 1.5 V at a rate of 50 mVs⁻¹.

2.5.5 Photocatalytic Activity Tests

The photoreactor consisting of a 500 mL jacketed reactor with a 220 mm jacketed quartz immersion well was purchased from Ace Glass, Inc. A quartz mercury low pressure UV arc lamp (450 W, Ace Glass, Inc.) is used to illuminate the photocatalysts. All joints of the reactor are lubricated with Teflon grease (Krytox[®]), as other greases are observed to decompose and release volatiles when under UV illumination. O₂ production is monitored using a micro gas-chromatograph (490 Micro GC, Agilent Technologies, AG) with a 1 m CP-COX column used to separate O₂. An oil-filled bubbler is used to prevent backflow of ambient air into either the micro GC or the reactor. Photocatalytic tests are performed under a flow (26 mL.min⁻¹) of N₂, with a T-junction going to the microGC allowing online sampling of the gases evolved. Photocatalysis is performed within a sealed (non-reflective) light-tight enclosure, and the reactor and UV lamp are cooled with 20 °C cooling water. Agitation is provided via a Teflon stir bar spinning at 435 rpm. Prior to starting photocatalysis, the reactor is filled with a 0.1 M AgNO₃ solution and 100-600 mg of catalyst is loaded. The suspension is then degassed under dynamic vacuum (ca. 20 mbar) for 30 min, followed by de-aeration with bubbling N₂ (26 mL.min⁻¹) for 1 h. GC analysis of the gas stream is free of O₂ prior to starting each photocatalytic test. During photocatalysis, the micro GC is programmed to sample the outlet gas stream on regular intervals, and the UV light is turned on at the same moment of the first GC sample. Once photocatalysis begins the reactor enclosure is not opened and gas production is regularly monitored. Quantification of the O₂ production is done via TCD, which is calibrated prior to use. O₂ production was calculated by the following route: v = volumetric flowrate (mL.min⁻¹) c = concentration (vol %) n = molar flow rate (mol.min⁻¹) Known quantities: v_{N_2} (N₂ flowrate, 26 mL.min⁻¹) and c_{O_2} (concentration of O₂ measured by TCD, vol %), P = atmospheric pressure 1.01 bar, T = 300 K. Calculating volumetric O₂ flow: v_{O_2} (mL.min⁻¹) = $v_{N_2} \cdot c_{O_2}$ Converting volumetric O₂ flow to molar O₂ flow using the ideal gas law: n_{O_2} (mol.min⁻¹) = Pv_{O_2}/RT This number is then divided the mass of catalyst used.

3 Niobium and Antimony-doped Tin Oxide: Structural Differences and Consequences for Electrical Conductivity

3.1 Individual Contributions

All materials were prepared and characterised by E. Oakton unless otherwise stated below. Electrical conductivity measurements were performed using the equipment of the Electrochemistry Laboratory at the Paul Scherrer Institute. The conductivity of commercial antimony-doped tin oxide was performed by E. Fabbri. High Temperature XRD studies were performed and analysed at CSEM SA by Z. Mickovic, J. Tillier and O. Sereda. EPR measurements were performed by M. Schwarzwälder and R. Kissner. EDX maps were measured by F. Krumeich using the facilities of ScopeM at ETH Zürich. XANES characterisation was performed at the Swiss Light Source at the Paul Scherrer Institute and analysed by G. Siddiqi.

This chapter includes work previously published by The Royal Society of Chemistry: Oakton, E.; Tillier, J.; Siddiqi, G.; Mickovic, Z.; Sereda, O.; Fedorov, A.; Copéret, C. *New. J. Chem.* **2016**, *40*, 2655-2660. Copyright, The Royal Society of Chemistry, 2016.

3.2 Introduction

Tin-based metal oxides are of high interest for a variety of technological applications including gas sensor technology,^[125–128] lithium ion batteries,^[129–131] optoelectronic devices,^[132–134] polymer electrolyte fuel cells (PEFCs)^[46, 135, 136] and heterogeneous catalysis.^[137, 138] The performance of tin oxide in many of these applications depends on the tuning of its electrical conductivity. Whilst stoichiometric SnO₂ is a semiconductor, the addition of a dopant atom can increase carrier concentrations and electron mobility, thereby enhancing electrical conductivity at room temperature.^[139] For instance the incorporation of Sb⁵⁺, a group (V) electron donor, into the host SnO₂ lattice provides antimony-doped tin oxide (ATO), which is a well known electron conductor^[140–142] with numerous applications.^[132, 143–146]

The high conductivity of ATO has led to its investigation as a carbon-free catalyst support for PEFCs.^[39, 48, 56, 63, 147] A variety of reports show improved oxygen reduction reaction (ORR) activities for Pt nanoparticles supported on antimony-doped tin oxide supports, in comparison to Pt on carbon supports, which were rationalised by metal-support interactions.^[56, 63] Yin et al. characterised Pt nanoparticles supported on mixed carbon and ATO supports and found that increasing the ATO content of the support increased the proportion of Pt in the metallic state

(Pt(0)) and decreased the binding energy of Pt(0).^[56] Increasing amounts of metallic Pt(0) likely improves dissolution stability in acidic media,^[57] whilst decreased binding energies alter the adsorption energy of O₂ on the Pt surface, leading to increased activities. Such shifts in binding energy have been previously rationalised through Sn-Pt electron transfer.^[148,149] Although ATO supported Pt nanoparticles show improved stability under ORR conditions with respect to Pt on carbon, questions regarding the longer term stability of ATO itself have been raised. It is known that the post-synthetic treatment conditions of ATO are vital for maintaining the desired dopant distribution. Fabbri et al. have recently shown that Sb segregates to the oxide surface during annealing and potential cycling, resulting in phase separation and leaching of antimony into the acidic electrolyte.^[48] This study demonstrates the importance of dopant concentration at the oxide particle surface and that achieving an even dopant distribution throughout the SnO₂ oxide host may be key to increasing the stability of these materials.^[48]

Niobium-doped tin oxide has been investigated as an alternative to ATO under PEFC relevant conditions.^[136,150,151] Takasaki et al. reported improved electrochemically active surface area (ECSA) values for Pt supported on Nb-doped SnO₂ in comparison to Sb-doped and pure SnO₂ as well as carbon, which was rationalised by the higher electrical conductivity of this support.^[151] Stability tests over 10 000 potential cycles show that although there is a gradual decrease in ECSA for the Nb-doped material, the ECSA remains above the alternative supports investigated. Interestingly, there is a wide variety of reported electrical conductivity values for Nb-doped SnO₂ aimed towards PEFC applications,^[136,151–157] ranging between 1600 and 0.07 S.cm⁻¹ for thin films^[152–154,156] and from 0.02 to 1.1x10⁻⁴ S.cm⁻¹ for high surface area nanopowders.^[136,151,155] Indeed it is known that electrical conductivity can vary as a function of the amount of dopant and the homogeneity of its distribution within the host oxide lattice, with the latter depending greatly on the preparation method. As there is a wide range of methods for the preparation of doped oxides, detailed characterisation is vital to fully understand the material structure and move towards the development of structure-property relationships.

Herein, niobium and antimony-doped tin oxides are prepared by aqueous co-precipitation. The effect of Nb content and post-synthetic treatment on Nb-doped tin oxide conductivity is investigated. Despite their analogous preparation methods, the conductivities of the niobium and antimony doped oxides are significantly different. To gain a detailed understanding of the oxide structure, highly sensitive characterisation techniques are employed, including solid state nuclear magnetic resonance spectroscopy and X-ray absorption spectroscopy. In addition, the crystallisation process is followed by variable temperature X-ray diffraction analysed using Rietveld refinement. These detailed structural insights are used to rationalise the measured differences in electrical conductivity.

3.3 Results and Discussion

3.3.1 Optimisation of Niobium-doped Tin Oxide

Co-precipitation has been shown as an effective route to prepare doped tin oxides.^[158–162] Niobium-doped tin oxide ($\text{SnO}_2\text{:Nb}$) was prepared by co-precipitation from Sn(IV) and Nb(V) chloride precursors, where increasing the pH of the acidic aqueous precursor solution triggered oxide precipitation. Both dopant concentration and its distribution throughout the host oxide are key for electrical conductivity. As dopant distribution is known to be highly dependent on the preparation method, Nb loading was optimised for Nb-doped tin oxides prepared by this co-precipitation method. Nb content was varied between 0 and 10 mol_M%, where M represents the total amount of metal atoms. Following post-synthetic treatment at 500 °C under synthetic air flow these materials were characterised by N_2 absorption-desorption with Brunauer-Emmett-Teller (BET) theory (Figure 16), transmission electron microscopy (TEM) imaging (Figure 17), electrical conductivity measurements (Table 7) and energy-dispersive X-ray (EDX) spectroscopy mapping (Figure 18).

Figure 16 compares the N_2 adsorption-desorption isotherms of pure SnO_2 and SnO_2 with a nominal Nb content of 5 mol_M%. Both isotherms have a type II shape typical of nanoparticulate materials, and are representative of all materials discussed in this chapter. The large hysteresis observed at large pressures maybe be due to the formation of metastable nitrogen layers, which delays the continuation of desorption.^[163] Indeed such hystereses could indicate a mesoporous structure, however this is not corroborated by TEM imaging (Figure 17). Bright field TEM images show the powders are composed nanoparticles and when Nb content is increased, smaller particles are observed, which is particularly obvious for the 10 mol_M% Nb sample (Figure 17).

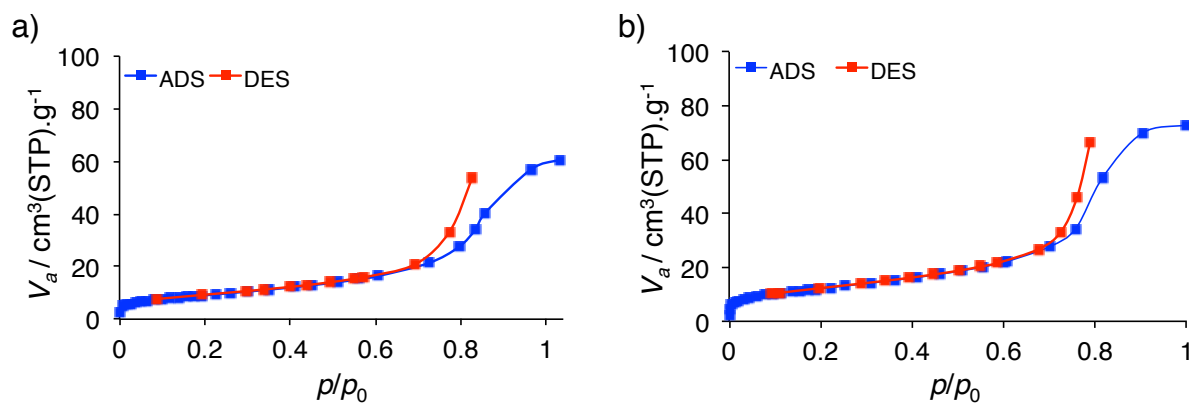


Figure 16: N_2 adsorption-desorption isotherms of SnO_2 (a) and $\text{SnO}_2\text{:Nb}_{0.05}$ (b).

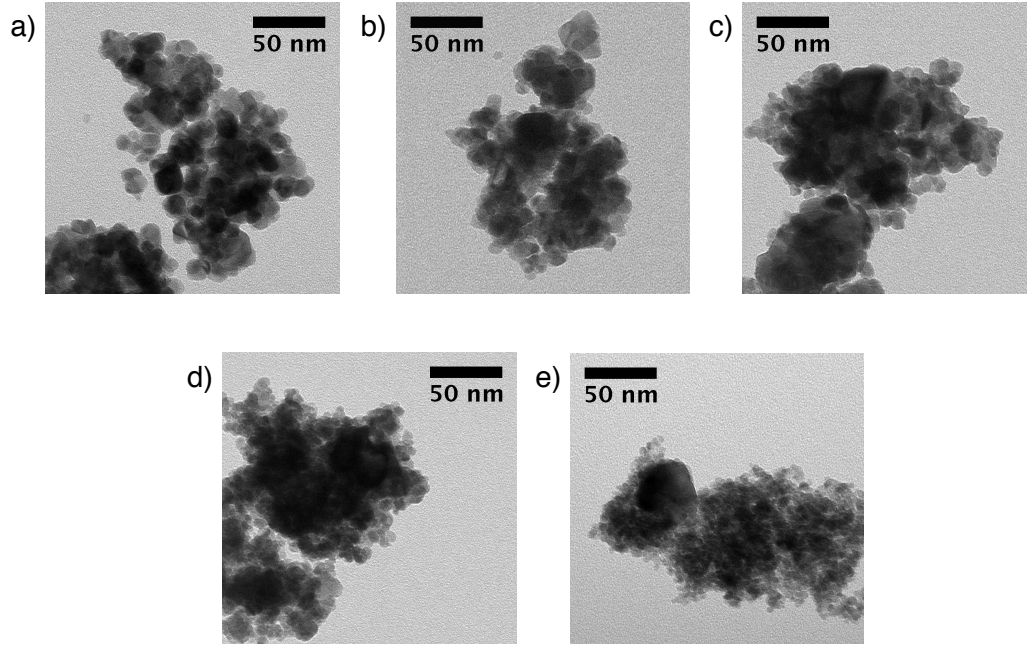


Figure 17: TEM images of $\text{SnO}_2\text{:Nb}$ compositions with 0 (a), 1 (b), 2 (c), 5 (d) and 10 (e) mol% Nb.

Comparing the surface area values derived using BET theory, an increase in surface area with increasing Nb content is observed (Table 7), which is consistent with the TEM data (Figure 17). Electrical conductivity values do not show such a clear trend with Nb content, however there is a small increase in conductivity noted for the 5 mol_M% sample (Table 7). Interestingly a further drop in conductivity is observed for the 10 mol_M% niobium-doped tin oxide sample. Comparing the EDX maps shown in Figure 18, there is a drastic difference in the distribution of Nb within these two samples, with the 10 mol_M% showing Nb segregation, which accounts for the low electrical conductivity. This initial study has shown that 5 mol_M% is the optimum nominal Nb loading to achieve maximum electrical conductivity.

Table 7: Electrical Conductivity of $\text{SnO}_2\text{:Nb}$ materials

Nominal Nb content / mol _M %	S_{BET} / m ² .g ⁻¹	σ / S.cm ⁻¹
0	33	10 ⁻⁶
1	28	10 ⁻⁶
2	28	10 ⁻⁶
5	43	10 ⁻⁵
10	55	10 ⁻⁶

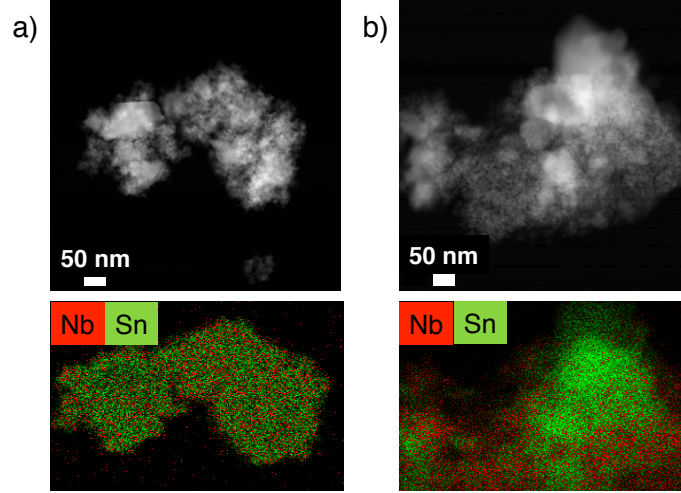


Figure 18: HAADF-STEM images and EDX maps of $\text{SnO}_2\text{:Nb}$ with 5 mol_M% (a) and 10 mol_M% (b) nominal Nb content.

Niobium-doped tin oxide with a nominal Nb content of 5 mol_M% was selected to investigate the influence of post-synthetic treatment on electrical conductivity and is herein noted as $\text{SnO}_2\text{:Nb}$. The temperature of post-synthetic treatment under synthetic air-flow (calcination) was varied between 350 °C and 800 °C. After treatment, each sample was characterised with N_2 adsorption-desorption with BET theory and electrical conductivity measurements (Table 8) as well as bright field TEM imaging (Figure 19). It is important to note that for this investigation, $\text{SnO}_2\text{:Nb}$ was prepared on a larger scale than for the materials discussed previously, which may have triggered the formation of higher surface area materials. Nonetheless, a sharp decrease in surface is observed with increasing calcination temperature (Table 8). In comparison to surface area, electrical conductivity is markedly increased upon calcination, with a maximum at 500 - 650 °C (Figure 8).

Table 8: Electrical Conductivity of $\text{SnO}_2\text{:Nb}$ materials

Treatment Temperature / °C	S_{BET} / $\text{m}^2\cdot\text{g}^{-1}$	σ / $\text{S}\cdot\text{cm}^{-1}$
-	257	10^{-7}
350	143	10^{-6}
500	92	10^{-5}
650	59	10^{-5}
800	28	10^{-6}

Bright field TEM imaging shows a clear increase in particle size with increasing temperature, supporting that this decrease in surface area is due to particle sintering.

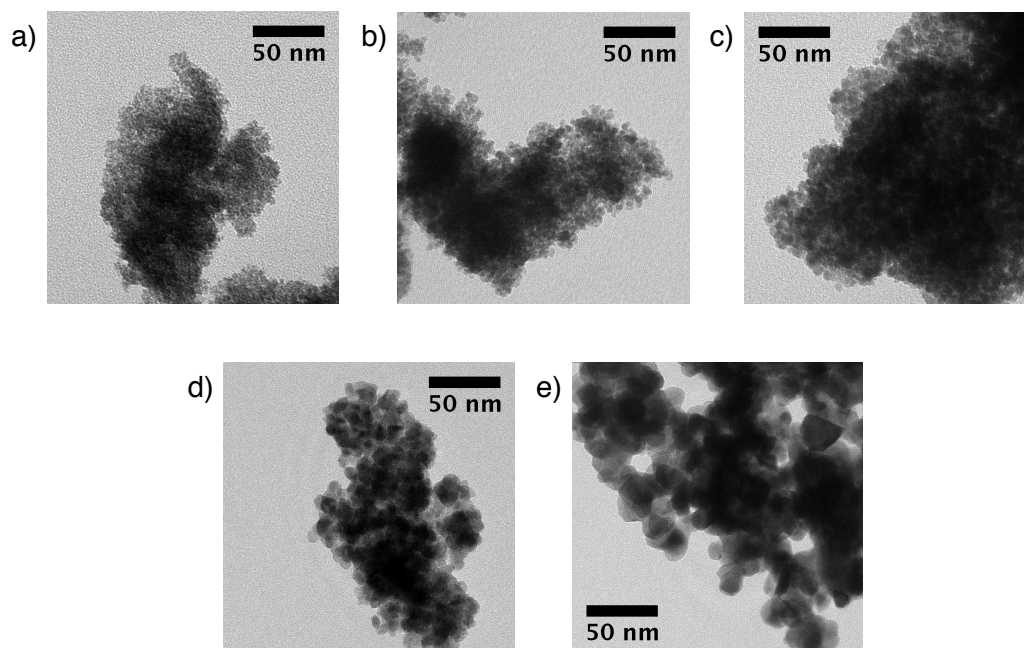


Figure 19: TEM images of $\text{SnO}_2\text{:Nb}$ treated at various temperatures under synthetic air flow; 80 °C, 350 °C (b), 500 °C (c), 650 °C (d) and 800 °C (e).

This short investigation has shown that optimum conductivity values are obtained with calcination temperature between 500 and 650 °C. Taking surface area into account, calcination treatment at 500 °C was determined to be optimum for the preparation of high surface area niobium-doped tin oxide materials.

3.3.2 Preparation of Antimony-doped Tin Oxide and Comparison to Niobium-doped Tin Oxide

Antimony-doped tin oxide ($\text{SnO}_2\text{:Sb}$) was prepared by an analogous co-precipitation route using SbCl_5 with a nominal Sb content of 5 mol_M%. After washing and calcination under synthetic air-flow at 500 °C, a blue-grey powder was obtained. Initial characterisation by N_2 adsorption-desorption and conductivity measurements show that this material has a comparable surface area and electrical conductivity to a commercial antimony-doped tin oxide sample (Table 9). Comparing the homemade niobium and antimony-doped tin oxide, it is clear that both synthetic procedures yield materials with comparable surface areas, however the electrical conductivity of $\text{SnO}_2\text{:Sb}$ is significantly higher than that of $\text{SnO}_2\text{:Nb}$.

Table 9: Surface Area and Electrical Conductivity of SnO₂:Sb and SnO₂:Nb (commercial materials denoted by *)

Material	$S_{BET} / \text{m}^2.\text{g}^{-1}$	$\sigma / \text{S.cm}^{-1}$
SnO ₂ :Nb	92	10^{-5}
SnO ₂ :Sb	80	0.02
SnO ₂ :Sb*	70-80	0.03

In order to better understand the differences in conductivity between these materials, additional characterisation techniques were used to compare these samples. Dopant content was determined by elemental analysis after calcination treatment (Table 10). Comparing these values to the nominal loadings (Table 11) it is clear that the dopant loadings for Nb are in good agreement, whilst the measured Sb content of SnO₂:Sb is approximately half the expected value. The reduced Sb content of SbCl₅ may be linked to the lower boiling point of SbCl₅, and hence increased volatility, in comparison to NbCl₅.

Table 10: Elemental Analysis of SnO₂:Nb and SnO₂:Sb

Material	Sn / wt%	Sb / wt%	Nb / wt%	Cl / wt%
SnO ₂ :Nb	70.5	-	2.97	1.18
SnO ₂ :Sb	73.2	1.92	-	0.53

Table 11: Comparison of Measured and Nominal Dopant Loadings

Material	Measured / wt%	Measured / mol _M %	Nominal / mol _M %
SnO ₂ :Nb	2.97	4.8	5.0
SnO ₂ :Sb	1.92	2.4	5.2

Dopant content is known to influence the electrical conductivity of doped oxides. Therefore, the conductivity difference between these materials may be explained by the difference in dopant content. However the optimisation of SnO₂:Nb has shown that changing the dopant content in a relatively wide range has not further increased conductivity. Therefore structural differences are still expected to play a major role in rationalising these differences in conduc-

tivity. Consequently, $\text{SnO}_2\text{:Nb}$ and $\text{SnO}_2\text{:Sb}$ were characterised by X-ray diffraction (XRD), N_2 adsorption-desorption, TEM imaging and EDX mapping.

XRD powder diffraction patterns of SnO_2 , $\text{SnO}_2\text{:Sb}$ and $\text{SnO}_2\text{:Nb}$ recorded during treatment at 500 °C are shown in Figure 20. Comparing the diffraction patterns with the cassiterite SnO_2 reference shows that all peaks can be accounted for. All other peaks are due to the Pt heating strip. Additionally, the $\text{SnO}_2\text{:Nb}$ and $\text{SnO}_2\text{:Sb}$ powder patterns are comparable to that of SnO_2 prepared and characterised under the same conditions. This suggests that cassiterite SnO_2 is the single phase present in both doped materials and that dopant phases are not observed by this characterisation technique.

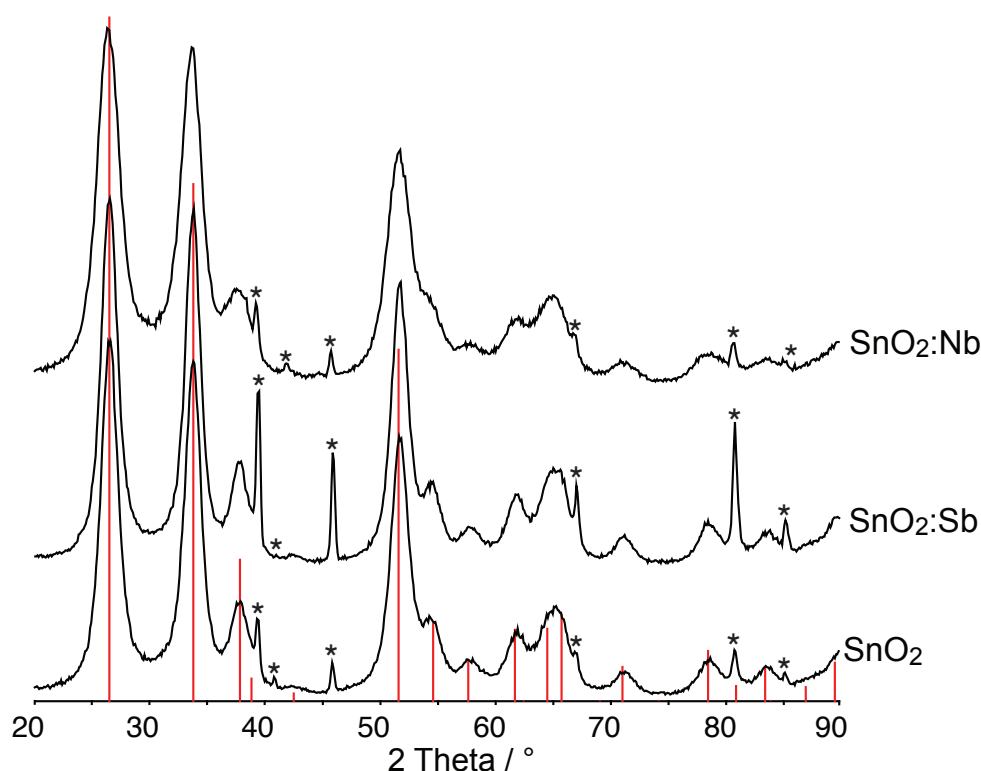


Figure 20: XRD powder diffractions patterns of SnO_2 , $\text{SnO}_2\text{:Sb}$ and $\text{SnO}_2\text{:Nb}$ recorded at 500 °C with reference pattern of cassiterite SnO_2 (ICDD 00-077-0447). Peaks due to the Pt heating strip are denoted by *.

Bright field TEM imaging of these three samples before and after calcination at 500 °C are shown in Figure 21. All samples have nanoparticulate morphologies, with average particle diameters around 1 nm for the as-synthesised powders. After calcination, the oxide particles increase in size to around 5 - 10 nm diameters in all cases. This characterisation demonstrates the morphological similarity between SnO_2 , $\text{SnO}_2\text{:Nb}$ and $\text{SnO}_2\text{:Sb}$ prepared by co-precipitation.

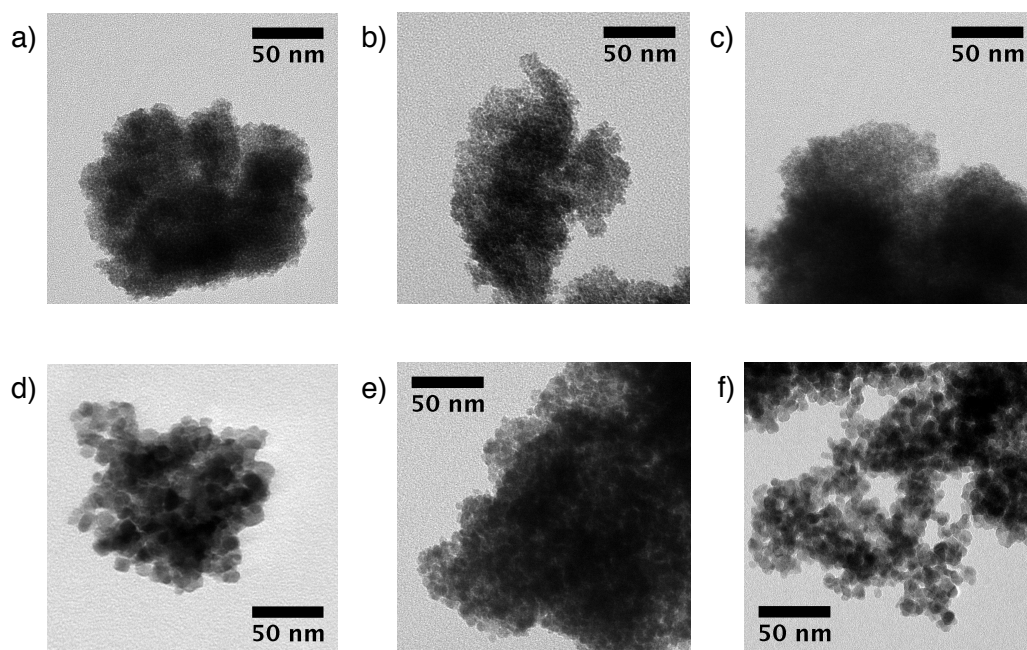


Figure 21: Bright field TEM images of SnO_2 , $\text{SnO}_2\text{:Nb}$ and $\text{SnO}_2\text{:Sb}$ before (a, b, c) and after (d, e, f) calcination respectively.

Continuing with microscopy techniques, the dopant distribution within $\text{SnO}_2\text{:Nb}$ and $\text{SnO}_2\text{:Sb}$ was qualitatively evaluated using EDX mapping. These elemental maps (Figure 22) show that both before and after calcination, all samples have an even distribution of the dopant throughout the large particle agglomerates. From these characterisation techniques it can be concluded that both Nb and Sb are doped homogeneously within the tin oxide lattice.

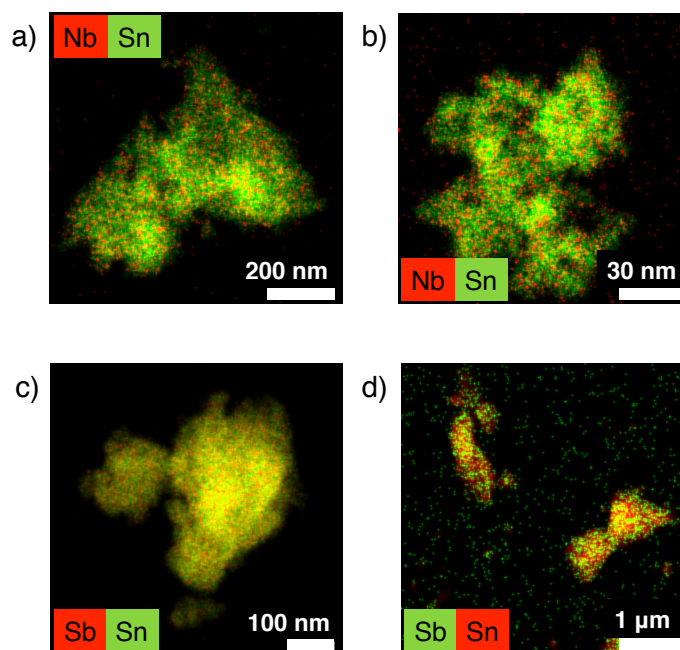


Figure 22: EDX maps of SnO₂:Nb and SnO₂:Sb before (a, c) and after (b, d) calcination respectively.

In summary, the characterisation techniques detailed above show that the morphology of both niobium and antimony-doped materials are highly similar. In particular, XRD measurements do not reveal the presence of additional oxide phases and EDX maps indicate an even distribution of dopant throughout large particle agglomerates.

3.3.3 Detailed Characterisation of Tin Oxide, Niobium-doped Tin Oxide and Antimony-doped Tin Oxide

To gain a more detailed understanding of these oxide structures, High Temperature XRD (HT-XRD) measurements, ¹¹⁹Sn nuclear magnetic resonance (NMR) spectroscopy, Nb K-edge X-ray absorption near edge structure (XANES) spectroscopy were used to characterise the doped oxides. HT-XRD measurements were performed on the as-synthesised oxide powders, which were heated through two heating cycles between room temperature and 800 °C and diffraction patterns were recorded at 50 °C intervals during heating. The recorded diffraction patterns can be found in Appendix 2. Following Rietveld refinement of the diffraction patterns, the lattice volume and crystallite sizes were determined and are shown in the graphs below (Figure 23). The variation of lattice volume shows a non-linear decrease during the first heating cycle, likely due to improvement of chemical order (crystallisation). Initial lattice volumes decrease in the order: SnO₂ > SnO₂:Nb > SnO₂:Sb, and the lattice volumes of SnO₂ and SnO₂:Nb are comparable from around 350 °C. During the second heating cycle, the lattice volumes of all samples are comparable and there is a linear lattice volume increase, which is explained by thermal

expansion of the lattice. Comparing variations in crystallite size during heating shows that all initial values are comparable and the increase in crystallite size during heating is likely due to crystallisation. However it is interesting to note that $\text{SnO}_2\text{:Nb}$ crystallites grow at approximately half the rate of SnO_2 and $\text{SnO}_2\text{:Sb}$. Crystallite sizes remain approximately constant during the second heating cycle.

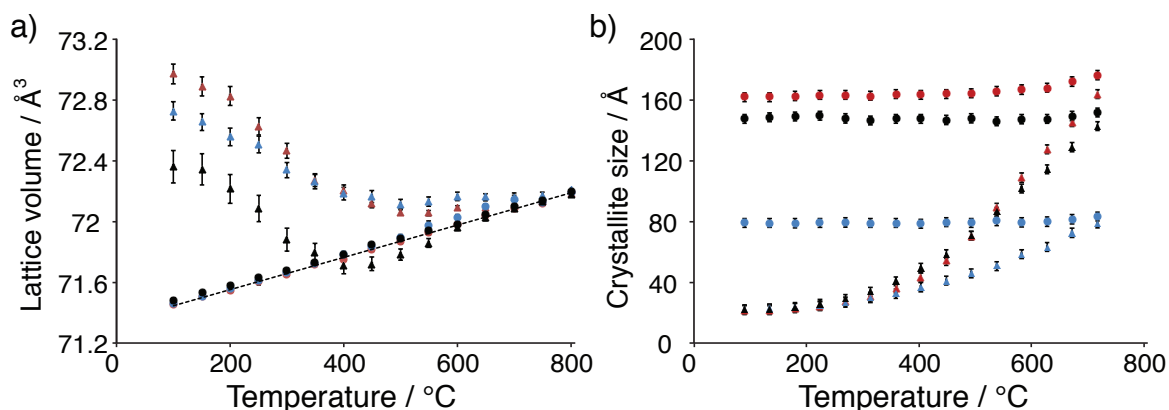


Figure 23: Variation of a) lattice volume and b) crystallite size of SnO_2 (red), $\text{SnO}_2\text{:Nb}$ (blue) and $\text{SnO}_2\text{:Sb}$ (black) during heating cycle 1 (triangle) and heating cycle 2 (circle).

Comparing the behaviour of lattice volume and crystallite size during these measurements can give an insight into the material structure. Lattice volumes are a typical indicator of dopant incorporation due to swelling or contraction of the host lattice when the dopant center has a significantly different ionic radius to the host. Sb^{5+} has a smaller ionic radius in comparison to Sn^{4+} and therefore the decrease in lattice volume observed is consistent with the incorporation of Sb^{5+} in SnO_2 .^[164] This indicates antimony is doped within the SnO_2 lattice throughout the heat treatment. A smaller lattice volume is also observed for $\text{SnO}_2\text{:Nb}$ until 350 $^\circ\text{C}$, as would be expected as the ionic radius of octahedral Nb^{5+} falls between Sn^{4+} and Sb^{5+} .^[164] This suggests that initially niobium is doped within the SnO_2 lattice and segregates upon heat treatment. Similarly, crystallite size can be an indicator of dopant segregation as the limitation of crystallite growth by segregated dopant phases has been reported.^[165,166] Therefore the similar growth rates and final crystallite sizes of SnO_2 and $\text{SnO}_2\text{:Sb}$ are a good indication that all antimony is evenly distributed throughout the SnO_2 host lattice. In contrast, the slower growth rate of $\text{SnO}_2\text{:Nb}$, in addition to the lattice volume trends observed, supports the presence of a segregated phase, likely Nb_2O_5 .

HT-XRD measurements indicate the presence of segregated dopant phases in $\text{SnO}_2\text{:Nb}$. ^{119}Sn Magic Angle Spinning (MAS) NMR was used to characterise the influence of the dopant centers

on the SnO_2 host, in order to determine if any Nb dopant is incorporated in SnO_2 . The ^{119}Sn MAS NMR spectra of SnO_2 , $\text{SnO}_2\text{:Nb}$ and $\text{SnO}_2\text{:Sb}$ before and calcination at 500°C are reported in Figure 24. The spectra recorded before calcination each show a peak around -600 ppm, which is assigned to the environment of Sn^{4+} . All other peaks are assigned as spinning side bands. These signals can be described by two main characteristics chemical shift value and line width, the latter reported as Full Width Half Maximum (FWHM), which are shown in Table 12. Comparing these data shows that all samples have comparable chemical shift and line width values before calcination. After calcination, both chemical shift and line width increase in the order: $\text{SnO}_2 < \text{SnO}_2\text{:Nb} < \text{SnO}_2\text{:Sb}$.

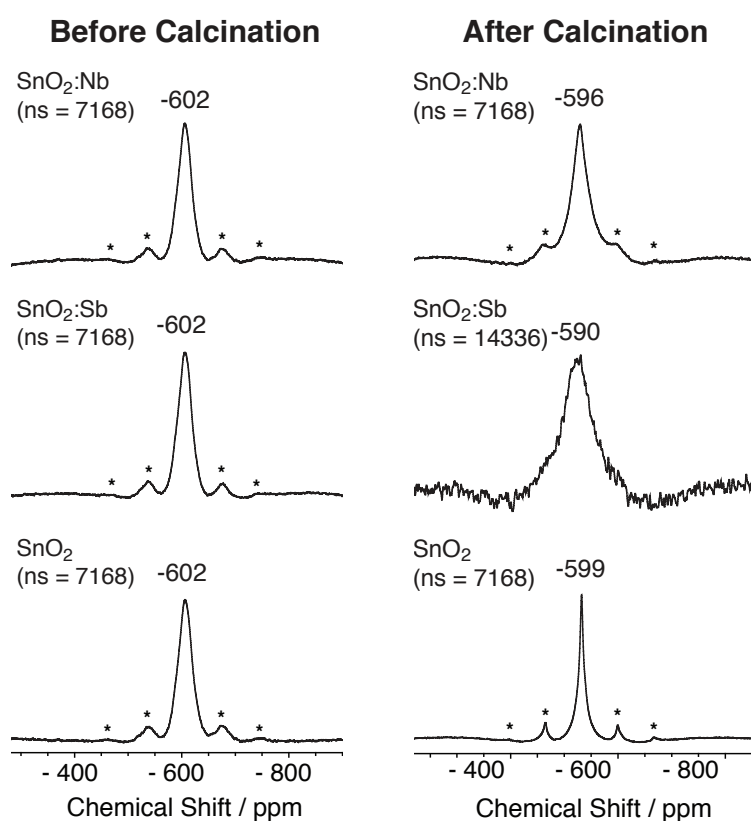


Figure 24: ^{119}Sn MAS NMR spectra of SnO_2 , $\text{SnO}_2\text{:Nb}$ and $\text{SnO}_2\text{:Sb}$ before and after calcination. Spinning side bands are denoted by *.

Table 12: Chemical shifts and line widths (FWHM) of SnO₂, SnO₂:Nb and SnO₂:Sb

	Material	Chemical shift / ppm	Line width / Hz
Before Calcination	SnO ₂	-602	4500
	SnO ₂ :Nb	-602	4500
	SnO ₂ :Sb	-602	4500
After Calcination	SnO ₂	-599	1500
	SnO ₂ :Nb	-596	5200
	SnO ₂ :Sb	-590	9200

All samples have the same chemical shift and line width before calcination, which indicates that all Sn⁴⁺ centers are in a similar environment. This can be explained by the poor crystalline nature of the as-synthesised materials, which were dried at 80 °C. Large variations in the ¹¹⁹Sn signals are observed after calcination. Whilst the line width of the SnO₂ signal narrows, due to improvement in chemical order as a result of crystallisation, the line widths of SnO₂:Nb and SnO₂:Sb increase. This broadening is assigned to the presence of dopant Sb⁵⁺ and Nb⁵⁺ centers within the SnO₂ lattice, which influence the distribution of local Sn⁴⁺ environments.^[167,168] Combining this information with the HT-XRD measurements, it is concluded that whilst all Sb⁵⁺ has substituted Sn⁴⁺ sites within the SnO₂ lattice, only partial amounts of Nb⁵⁺ substitute Sn⁴⁺ and the remainder exist as segregated Nb₂O₅.

Interestingly, the Sn⁴⁺ signals after calcination are shifted downfield, with the degree of shift varying in magnitude in the order: SnO₂ < SnO₂:Nb < SnO₂:Sb. Such downfield shifts are typically associated with reduced electron density around the center of interest. Whilst the presence of the different dopant centers likely contribute to this downfield shift, the shift observed for pure SnO₂ indicates that there are additional contributions. One explanation of this would be the reduction in electron density around Sn⁴⁺ by oxygen vacancies.^[168] In order to confirm the presence of oxygen defects and characterise their nature, all materials were characterised by EPR spectroscopy. The EPR spectra of the as-synthesised materials do not show any signals, indicating an absence of oxygen defects, which is consistent with their NMR spectra. Two signals are observed for calcined SnO₂ at g = 2 and g = 1.89. The sharp signal at g = 2 is assigned to superoxide species and/or oxygen defects,^[169] whilst the broad signal at g = 1.89 is assigned to oxygen defects.^[170] A broad, signal with weak hyperfine coupling centered around g = 1.89 is observed for SnO₂:Nb. This signal is assigned to oxygen defects, which are likely coupling with Nb centers. This evidence of a weak defect-Nb interaction could mean that the defects are close to Nb⁵⁺ within the SnO₂ lattice. Interestingly, there is a complete lack

of signal observed for calcined $\text{SnO}_2\text{:Sb}$, likely due to the relatively high electron conductivity of this sample. This is rationalised by the interaction of oxygen defects with the delocalised electronic network of this material, which may lead to fast spin relaxation.

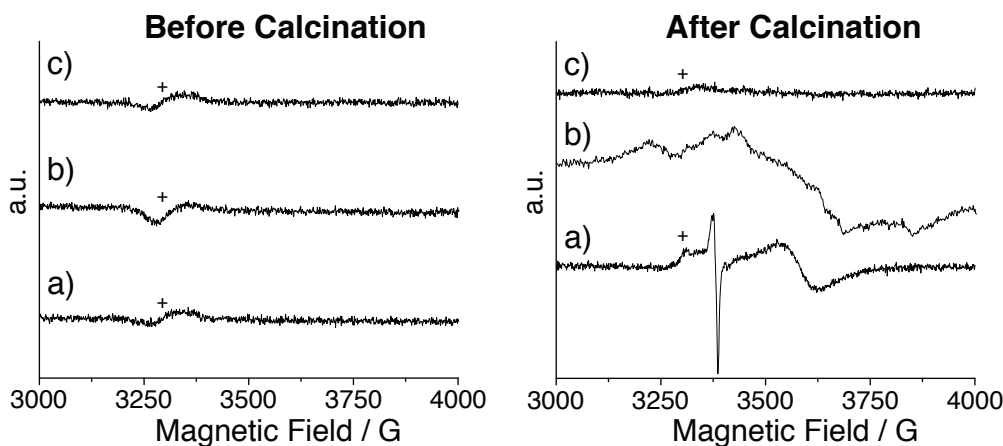


Figure 25: EPR spectra of SnO_2 (a), $\text{SnO}_2\text{:Sb}$ (b) and $\text{SnO}_2\text{:Nb}$ (c) before and after calcination at 500 °C.

To investigate the structure of $\text{SnO}_2\text{:Nb}$ from the dopant point of view, $\text{SnO}_2\text{:Nb}$ was characterised by Nb K-edge XANES spectroscopy and compared to homemade and commercial Nb_2O_5 , the powder diffraction patterns of which can be found in Appendix 2. Homemade Nb_2O_5 was prepared by an analogous precipitation route. Figure 26 shows the XANES spectra, with features of interest being the white line (edge) and clearly observable pre-edge signal present around 18994 eV. Comparing the white line energies of all samples before and after calcination confirms that all niobium centers are in the +5 oxidation state expected for Nb_2O_5 . Pre-edge features are known to be highly symmetry dependent and their interpretation can give information regarding the geometry of the absorbing center. Pre-edge features in Nb K-edge XANES spectra have been assigned to tetrahedral Nb, which can be present in Nb_2O_5 .^[171] Conversely, the absence of a pre-edge feature indicates all Nb centers are in octahedral symmetry.^[172] As all Sn sites in cassiterite SnO_2 are of octahedral symmetry, in the absence of severe lattice distortions, the dopant atom should adopt an octahedral symmetry when substituting a Sn^{4+} site. Therefore the absence or presence of this pre-edge feature can be used as an indication for the doping of Nb in SnO_2 . From Figure 26, a clearly observable pre-edge feature is observed for $\text{SnO}_2\text{:Nb}$ before and after calcination, indicating segregation of Nb_2O_5 . Interestingly, a decrease in the magnitude of the pre-edge feature is observed after calcination, even for homemade Nb_2O_5 (Figure 27). This observation can be explained by the crystallisation of Nb_2O_5 reducing the number of tetrahedral sites. However, the larger decrease observed

for $\text{SnO}_2\text{:Nb}$ indicates additional contributions to decreasing amounts of tetrahedral Nb_2O_5 . Considering the ^{119}Sn MAS NMR results discussed previously, it is proposed that Nb centers migrate into the SnO_2 lattice during the calcination process, leading to an additional drop in the pre-edge feature intensity.

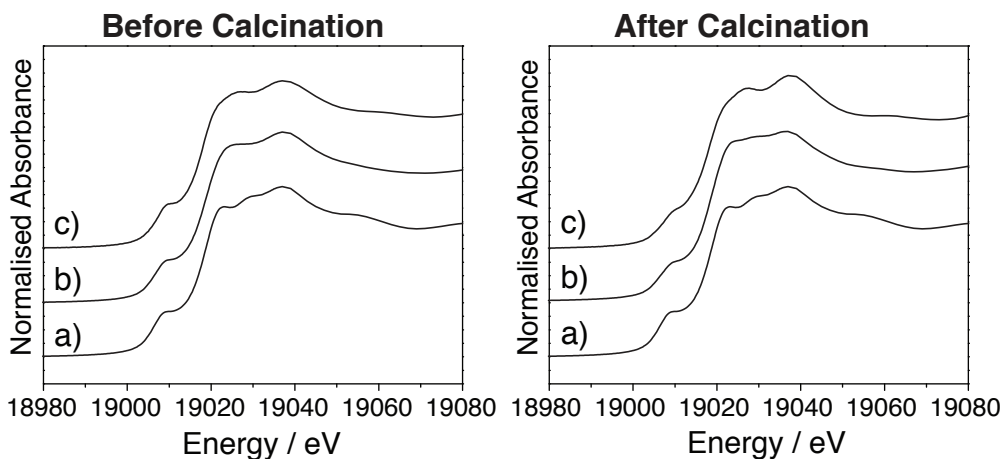


Figure 26: XAS spectra of commercial Nb_2O_5 (a), Nb_2O_5 (b) and $\text{SnO}_2\text{:Nb}$ (c) before and after calcination at 500 °C.

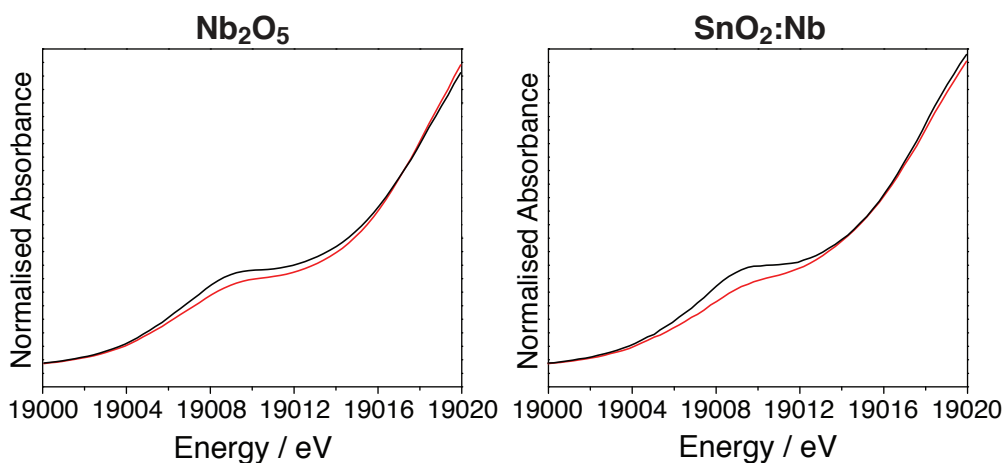


Figure 27: XAS spectra before (black) and after (red) calcination at 500 °C of homemade Nb_2O_5 and $\text{SnO}_2\text{:Nb}$.

Despite the apparent similarity of $\text{SnO}_2\text{:Sb}$ and $\text{SnO}_2\text{:Nb}$ from X-ray powder diffraction and EDX mapping, HT-XRD measurements as well as Nb-K edge XANES spectroscopy have revealed

that Nb in $\text{SnO}_2\text{:Nb}$ is partially segregated. This partial doping may be a result of reduced solubility of Nb in SnO_2 and/or differing hydrolysis rates of the Sn, Sb and Nb chlorides.

3.4 Conclusion

Niobium-doped tin oxide was prepared by a simple aqueous co-precipitation method, which yielded high surface area nanopowders. Optimum electrical conductivity was achieved with 5 mol_M% Nb loading and post-synthetic calcination treatment under air flow at 500 °C. Characterisation by XRD and EDX mapping shows cassiterite SnO_2 to be the single phase present and that the Nb dopant is evenly distributed across large nanoparticle agglomerates. Antimony-doped tin oxide, prepared under analogous conditions, has a comparable surface area but a much improved electrical conductivity with respect to its niobium analogue. Comparing $\text{SnO}_2\text{:Nb}$ and $\text{SnO}_2\text{:Sb}$ by XRD, TEM and EDX mapping characterisation methods suggest their phase and morphological similarity.

Variable temperature XRD measurements and ^{119}Sn MAS NMR spectroscopy were used to further understand the structures of $\text{SnO}_2\text{:Nb}$ and $\text{SnO}_2\text{:Sb}$, in particular their lattice volume variations and changes in the Sn environment as a result of calcination treatment. HT-XRD measurements analysed with Rietveld refinement confirmed that the lattice volume of $\text{SnO}_2\text{:Sb}$ is lower than that of pure SnO_2 , as would be expected for the incorporation of Sb^{5+} . In contrast, SnO_2 and $\text{SnO}_2\text{:Nb}$ have similar lattice volumes, which suggests Nb is not incorporated within the SnO_2 lattice. Furthermore the observed limitation of $\text{SnO}_2\text{:Nb}$ crystallite growth is consistent with the presence of a segregated dopant phase. ^{119}Sn MAS NMR spectroscopy shows a broadening of Sn^{4+} environments for the doped materials as a result of calcination, indicating that the dopant centers are present in the SnO_2 lattice. Therefore it is concluded that antimony is evenly distributed throughout the SnO_2 lattice, whilst niobium is partially segregated.

Further characterisation of niobium-doped tin oxide using Nb K-edge XANES spectroscopy revealed that Nb is in the 5+ oxidation state, in agreement with both commercial and home-made Nb_2O_5 . The observed pre-edge feature confirmed some Nb centers have tetrahedral geometry, as known for minor sites in Nb_2O_5 . An observed decrease in pre-edge feature intensity as a result of calcination treatment is due to both the crystallisation process and the migration of Nb into the SnO_2 lattice. Therefore it is concluded that as-synthesised $\text{SnO}_2\text{:Nb}$ is composed of SnO_2 and Nb_2O_5 and Nb migrates into the Nb lattice upon calcination to yield a partially doped material. This likely contributes to the reduction in electronic conductivity due to lower effective dopant concentrations. The homogeneous incorporation of Sb and the segregation of Nb could be explained by differences in solubility and/or precursor hydrolysis

rates. The inability to identify the segregated Nb_2O_5 phase by standard XRD diffraction and EDX mapping is likely due to the low content, poor crystalline nature and small particle size of any segregated Nb_2O_5 .

This investigation exemplifies that it is essential to characterise doped oxides by a combination of techniques from both the host and dopant point of view in order to fully understand the material structure. Through this investigation we have revealed significant structural differences between Sb and Nb doped SnO_2 , despite their preparation by an analogous co-precipitation method and their apparent similar structure according to classical characterisation techniques such as XRD diffraction and EDX mapping. An interesting area for future work would be to use these detailed characterisation techniques to develop alternative synthetic approaches to prepare niobium-doped tin oxide.

3.5 Experimental Details

3.5.1 General

$\text{SnCl}_4 \cdot 5\text{H}_2\text{O}$ (98%), SbCl_5 (99.999%), concentrated hydrochloric acid (99%), ammonium hydroxide (25% NH_3) and absolute ethanol were purchased from Sigma Aldrich and used as received. NbCl_5 (99.99%) was purchased from Strem Chemicals. Commercial ATO and Nb_2O_5 were obtained from Mitsubishi and Acros Organics respectively. Distilled water was further purified using a Merck Millipore Synergy Ultrapure Water System and had a resistivity of 18.2 $\text{M}\Omega \cdot \text{cm}$ at 25 °C upon use. N_2 adsorption-desorption analysis was conducted using a BEL-Mini device supplied by BEL Japan Inc. All samples were pre-treated at 150 °C under vacuum for 16 h on a BEL-Prep machine also from BEL Japan Inc. Results were fitted using BEL-Master programme and BET theory. Bright field TEM images were recorded using a 100 kV Philips CM12 transmission electron microscope. EDX maps were conducted on a FEI Talos F200X microscope. Electrical conductivity values were determined from powder disks under 0.625 MPa pressure with thicknesses in the range 100 - 1000 μm . Conductivity values were determined using 4-point measurements. Chronoamperometric measurements were used, where the current was recorded for a range of voltages (0.001 - 0.1 V) and conductivity subsequently calculated using Ohm's law. Electrical conductivity was determined for three pellet thicknesses and averaged to give the reported values. ^{119}Sn MAS NMR measurements were conducted on a 400 MHz Bruker spectrometer at 10 kHz spinning speed; the samples were packed in a 4 mm zirconia rotor. Continuous Wave (CW) EPR spectra of the powders in quartz tubes were recorded on a Bruker EMX X-Band spectrometer (9.5 GHz microwave frequency) at 110 K. XANES measurements at Nb K-edge were performed at the SuperXAS beamline at the Swiss

Light Source (Paul Scherrer Institute, Villigen, Switzerland). The SLS is a third generation synchrotron, which operates under top up mode, 2.4 GeV electron energy, and a current of 400 mA. The SuperXAS beamline is positioned on one of three super-bent ports. The incident beam was collimated by Si-coated mirror at 2.8 mrad, monochromatized using a double crystal Si(111) monochromator, and focused with Rh coated toroidal mirror (at 2.8 mrad) down to 100x100 μm . The beam intensity was of 4-5.10¹¹ ph.s⁻¹. The procedures reported below, except that for Nb₂O₅, refer to large-scale preparations.

3.5.2 XRD Characterisation

The High-Temperature X-Ray Diffraction (HT-XRD) experiments were performed using an Anton Paar HTK 16N high-temperature chamber mounted in an X'Pert Pro-MPD diffractometer. The samples were deposited on top of the Pt heating strip as a slurry in EtOH and allowed to dry. To ensure accurate temperature control the temperature regulator was attached onto the Pt strip. The samples were heated from room temperature up to 800 °C with a heating rate of 2 °C.min⁻¹ under ambient atmosphere. Bragg-Brentano diffraction patterns were acquired at 50 °C intervals between 100 °C to 800 °C. For each temperature step, a stabilisation time of 5 minutes was allowed before acquisition. After the first in-situ annealing, the samples were cooled down to room temperature with a cooling-rate of 60 °C.min⁻¹ and a second HT-XRD experiment was then performed under the same conditions. The diffractometer was equipped with the copper K α radiation (1.541874 Å) and the diffracted intensity has been recorded using a PIXcel detector with its maximum active length of 3.347° in order to allow quick acquisition of each diffractogram. The diffraction patterns have been acquired for 2 θ angles ranging from 20 to 90° with a step size of 0.1°. Instrumental broadening of XRD peaks has been taken in account using the NIST 674b standard.

3.5.3 Preparation of SnO₂

SnCl₄.5H₂O (16 g, 0.046 mol) was dissolved in 250 mL distilled H₂O. NH₄OH was added until the solution reached pH = 3, after which a white precipitate was formed. After stirring for 1 h, the precipitate was washed with distilled water and EtOH. After drying on a rotary evaporator (40 °C, 100 mbar), the white solid was dried under air flow at 80 °C for 1 h.

3.5.4 Representative Preparation of $\text{SnO}_2\text{:Nb}$

$\text{SnCl}_4 \cdot 5\text{H}_2\text{O}$ (15 g, 0.043 mol) was dissolved in 250 mL distilled H_2O . NbCl_5 (0.62 g, 2.3×10^{-3} mol) was removed from an Ar filled glovebox, immediately dissolved in conc. HCl (2 mL) and added to the Sn chloride solution. Following steps were conducted as described for SnO_2 .

3.5.5 Preparation of $\text{SnO}_2\text{:Sb}$

$\text{SnCl}_4 \cdot 5\text{H}_2\text{O}$ (15 g, 0.043 mol) was dissolved in 250 mL distilled H_2O . SbCl_5 (0.71 g, 2.4×10^{-3} mol) was immediately dissolved in conc. HCl (2 mL) and added to the Sn chloride solution. Following steps were conducted as described for SnO_2 .

3.5.6 Preparation of Nb_2O_5

NbCl_5 (3.95 g, 0.015 mol) was removed from an Ar filled glovebox, immediately dissolved in conc. HCl (6 mL) and added to ultrapure water (100 mL). Following steps were conducted as described for SnO_2 .

3.5.7 Post-synthetic Treatment

Approximately 2 g of the as-synthesised material was loaded into a glass flow reactor and calcined under synthetic air ($120 \text{ mL} \cdot \text{min}^{-1}$). All samples were calcined at 500°C for 16 h ($120^\circ\text{C} \cdot \text{min}^{-1}$) and cooled under air flow. $\text{SnO}_2\text{:Nb}$ was calcined at additional temperatures of 350, 650 and 800°C under the same heating rate and gas flow conditions.

4 Iridium Titanium Oxide: Preparation, Optimisation and Application in Electrochemical Oxygen Evolution

4.1 Individual Contributions

The synthetic method was developed by D. Lebedev and E. Oakton. D. Lebedev prepared and characterised the homemade IrO₂ materials investigated as oxygen evolution catalysts. All other materials were prepared and characterised by E. Oakton unless otherwise stated below. The XRD characterisation report in Figure 30 was performed by J. Tillier at CSEM SA. HAADF-STEM images were recorded by F. Krumeich using the ScopeM facilities of the ETH Zürich. The EDX map presented in Figure A16 was recorded at EPFL. Electrical conductivity measurements were performed using the equipment of the Electrochemistry Laboratory at the Paul Scherrer Institute. Electrochemical characterisation was performed and analysed by K. Waltar, M. Povia and D. Abbott at the Electrochemistry Laboratory of the Paul Scherrer Institute. X-ray absorption spectroscopy studies were performed by D. Abbott, E. Fabbri and M. Povia at the Swiss Light Source (Paul Scherrer Institute) and analysed by G. Siddiqi. All other characterisation methods were performed and analysed by E. Oakton.

This chapter includes work previously published by The Royal Society of Chemistry: Oakton, E.; Lebedev, D.; Fedorov, A.; Krumeich, F.; Tillier, J.; Sereda, O.; Schmidt, T. J.; Copéret, C. *New. J. Chem.* **2016**, *40*, 1834-1838. Copyright, The Royal Society of Chemistry, 2016.

4.2 Introduction

Water electrolysis presents a key opportunity to produce H₂ and O₂ using renewable energy.^[173] Proton exchange membrane water electrolyzers (PEMWEs) are electrochemical cells, which produce hydrogen at the cathode and oxygen at the anode.^[173,174] However the implementation of this technology is severely limited by the large overpotentials required for the oxygen evolution reaction (OER).^[70,175] There are a variety of suggested OER mechanisms (Table 13) and in all cases, oxygenated intermediates on the catalyst surface play a key role. The OER overpotential depends on the adsorption energies of the reaction intermediates.^[70,175,176] Additionally, there are multiple activation steps, which influence the reaction rate.^[176] The natural similarity of the oxygenated intermediates hinders catalyst development as the adsorption energies of each species are inherently linked and are therefore difficult to individually tune.^[70,176] Furthermore, many catalysts contain surface chlorides, which can complicate the

effective evaluation of these materials towards oxygen evolution, as chlorine evolution occurs at potentials only slightly higher than the standard potential of oxygen evolution, 1.36 V vs. 1.23 V respectively, and therefore can also contribute to the generated current.

Table 13: OER mechanisms in acidic solution^[176]

Electrochemical oxide pathway ^[177]
$S + H_2O \rightarrow S-OH + H^+ + e^-$
$S-OH \rightarrow S-O + H^+ + e^-$
$2S-O \rightarrow 2S + O_2$
Oxide pathway ^[177]
$S + H_2O \rightarrow S-OH + H^+ + e^-$
$2S-OH \rightarrow S-O + S + H_2O$
$2S-O \rightarrow 2S + O_2$
Krasil'shchikov pathway ^[178]
$S + H_2O \rightarrow S-OH + H^+ + e^-$
$S-OH \rightarrow S-O^- + H^+$
$S-O^- \rightarrow S-O + e^-$
$2S-O \rightarrow 2S + O_2$
Wade and Hackerman pathway ^[179]
$2S + 2H_2O \rightarrow SO + SH_2O + 2H^+ + 2e^-$
$SO + 2SOH^- \rightarrow 2S + SH_2O + O_2 + 2e^-$

The high OER activity and acid stability of IrO₂ together with its high electrical conductivity makes it a front runner for applications in PEMWEs.^[71, 175, 180] However, the high cost of IrO₂ is a limitation for the large scale application of PEMWE technology. A strategy to reduce cost and optimise IrO₂ usage would be to combine IrO₂ with a co-material, which effectively acts as a catalyst support. Many advantages of using catalyst supports have been identified, including reducing catalyst particle size, physical stabilisation of the catalyst particles and enhancing catalytic activity through synergistic effects.^[73, 181, 182] Typical requirements of OER catalyst supports include; long-term stability, high surface area and sufficient electrical conductivity.^[73] However, recent work has shown that materials with low electrical conductivities are also suitable supports, including titanium,^[183] tantalum,^[184] and silicon carbides^[185] as well as titanium,^[73, 186] silicon,^[187] tin^[188, 189] and tantalum^[190] based oxides. Interestingly, in the case of IrO₂ supported on TiO₂, the need to have sufficient IrO₂ content to allow for

efficient electron flow has been emphasised.^[73] Therefore the high surface area of the supporting material is a compromise between improving catalyst utilisation and minimising the amount of IrO₂ required to generate a conductive material through a percolation network of IrO₂ nanoparticles.^[73]

There are a variety of methods, which could be used to prepare iridium oxides. Sol-gel methods are well developed for the preparation of a variety of pure and mixed metal oxides,^[40,42,43] including Ir containing materials.^[191,192] However, sol-gel protocols typically require post-synthetic treatment at high temperatures to improve crystallinity and such treatments are often linked to reductions in surface area, which can be disadvantageous for catalysis. Additionally, long reaction times, as those reported for gelation,^[192] can be impractical when looking towards commercial applications. Adams method is an alternative oxide preparation route, first reported in 1923, involving the high temperature reaction of a metal precursor with sodium nitrate.^[193] A variety of oxides, including iridium-containing materials, have been prepared by this method.^[73,193–197] The short reaction times are a particular advantage in comparison to other routes.

This chapter describes the preparation of iridium titanium oxide (IrO₂-TiO₂) by a practical one-pot Adams method route. Composition dependent changes in surface area, TiO₂ phase, particle size and electrical conductivity are evaluated and discussed. This synthetic method is extended to cover IrO₂-MO_x materials (M = Sn or Nb) and measured differences in conductivity are discussed. Chlorine-free IrO₂-TiO₂ is yielded with comparable morphology. Chlorine-free IrO₂ and IrO₂-TiO₂ materials are investigated as oxygen evolution catalysts by rotating disk electrode experiments. Differences in activity, described by the potential required to achieve a set current value, are rationalised by X-ray absorption spectroscopy (XAS). Stability studies, involving potential cycling, are used to compare the most active OER catalysts.

4.3 Results and Discussion

4.3.1 Composition Optimisation

Iridium titanium oxide materials were prepared by an Adams method route involving the reaction of iridium(III) chloride and titanium(IV) oxysulfate with NaNO₃ at 350 °C. Iridium content was varied between 0 and 100 mol_M% in 20 mol_M% increments, where M represents the total number of metal centers. IrO₂-TiO₂ compositions are also denoted as X%IrO₂-(100-X)%TiO₂, where percentage refers to mol_M%.

Figure 28a shows a N_2 adsorption-desorption isotherm, which is representative of all yielded IrO_2 - TiO_2 materials. The type II shape curve is typical of nanoparticulate powders. Surface area values, $m^2.g^{-1}$, were derived from the N_2 adsorption-desorption measurements using Brunauer-Emmett-Teller (BET) theory. Figure 28b shows the variation of surface area with iridium content, with all samples having high surface areas around $250 m^2.g^{-1}$. However, considering the variation in formula weight between the iridium poor and iridium rich compositions, discussing surface area in terms of $m^2.g^{-1}$ may be misleading. When the effect of composition is removed by comparing surface area in molar terms, $m^2.mol^{-1}$, there is a clear increase in surface area with Ir content, suggesting composition has a direct influence on this property.

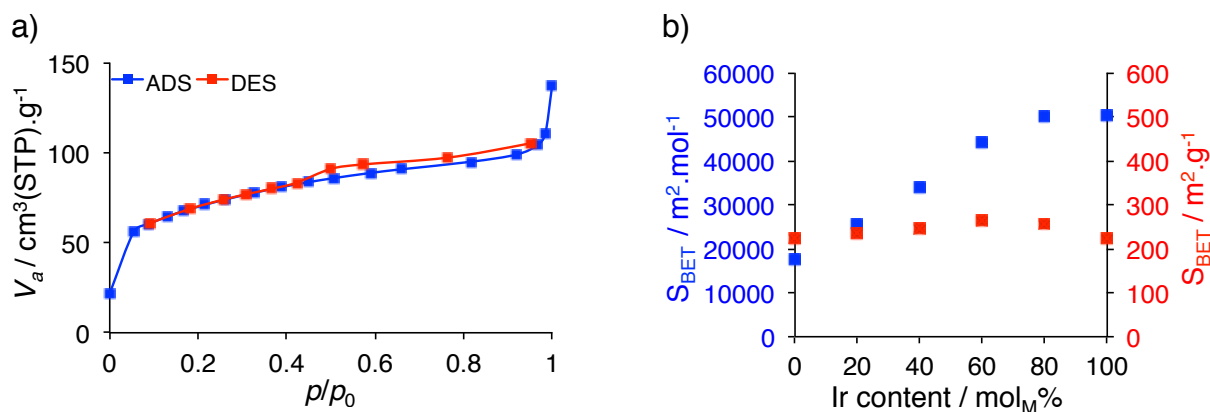


Figure 28: Representative N_2 adsorption-desorption isotherm of 40% IrO_2 -60% TiO_2 (a) and surface area values of varying IrO_2 - TiO_2 compositions (b).

Figure 29 details the interesting phase changes observed by X-ray diffraction (XRD) when varying sample composition. Anatase TiO_2 is formed in the absence of Ir, however anatase TiO_2 cannot be clearly identified in any other diffractogram shown in Figure 29. The broad diffraction pattern indicates that these samples are composed of small nanoparticles. To gain a more detailed understanding of the material structure, the XRD powder diffraction pattern of 40% IrO_2 -60% TiO_2 was recorded as a combination 200 scans (Figure 30). The asymmetry of the large diffraction peak around 35° indicates rutile TiO_2 is also present, in addition to IrO_2 and anatase TiO_2 . The identification of rutile TiO_2 suggests that IrO_2 influences the phase of TiO_2 formed. It is important to note that further analysis of this data using Rietveld refinement was limited by the broad and overlapping diffraction patterns.

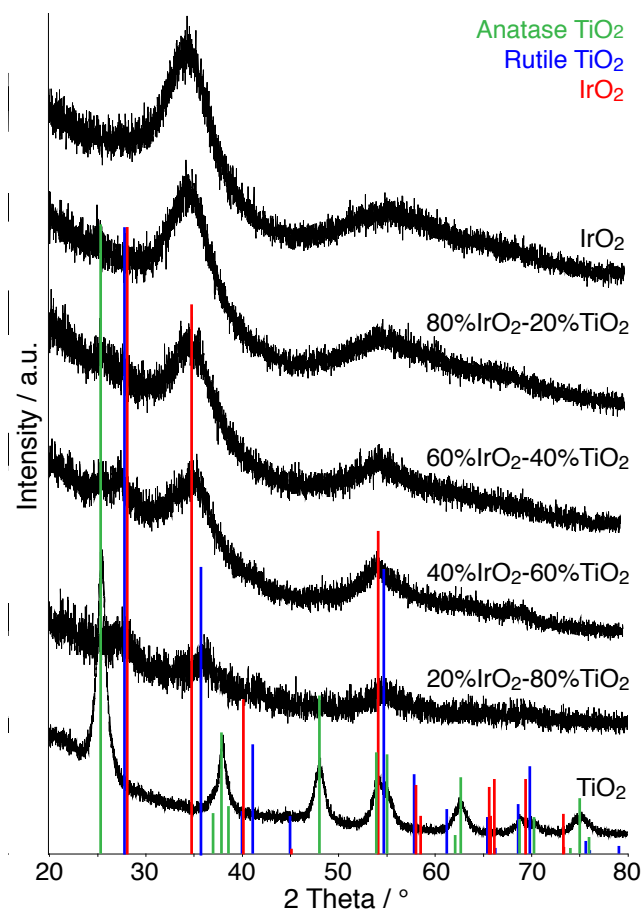


Figure 29: XRD diffraction patterns of varying IrO_2 - TiO_2 compositions with reference patterns for anatase TiO_2 (ICDD 00-084-1286), rutile TiO_2 (ICDD 00-086-0147) and IrO_2 (ICDD 00-015-0870).

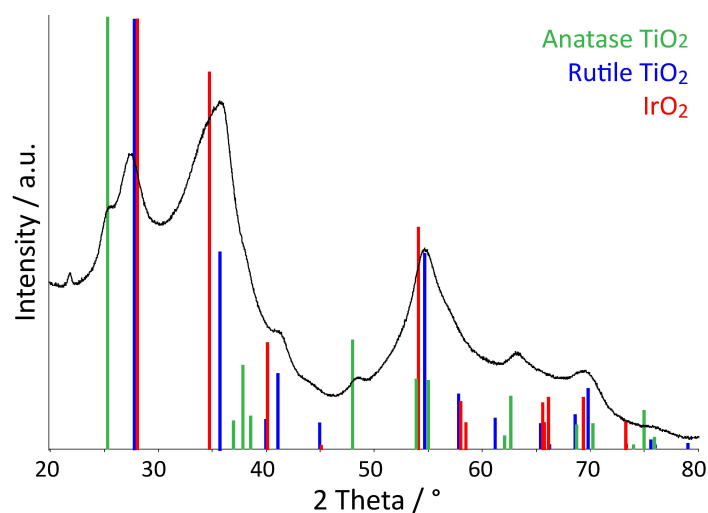


Figure 30: XRD diffraction pattern of 40% IrO_2 -60% TiO_2 with reference patterns for anatase TiO_2 (ICDD 00-084-1286), rutile TiO_2 (ICDD 00-086-0147) and IrO_2 (ICDD 00-015-0870). The peak around 23° is assigned to SiO_2 dust contamination.

Sample morphology was further probed by microscopy techniques. Comparing the bright field transmission electron microscopy (TEM) images of TiO_2 and IrO_2 show that particles around 5 and 1 - 2 nm in diameter are formed respectively (Figure 31). The formation of small IrO_2 particles fits well with the observed relationship between surface area and Ir content (Figure 28). Due to the high electron density of IrO_2 (and hence large electron scattering ability) detailed images of the IrO_2 - TiO_2 samples are difficult to obtain through bright field TEM. Therefore high angle annular dark field scanning transmission electron microscopy (HAADF-STEM) imaging, which has an increased sensitivity to electron density, was used. Shown below, the HAADF-STEM images detail a nanoparticulate structure, with bright areas assigned to be IrO_2 particles being clearly visible. By comparing the various compositions it is clear that the iridium oxide nanoparticles remain around 1 nm in diameter, independently of Ir content. Using this information, the IrO_2 - TiO_2 materials are described as mixtures of TiO_2 and IrO_2 particles, with particle diameters of 5 and 1 nm respectively, which are independent of composition.

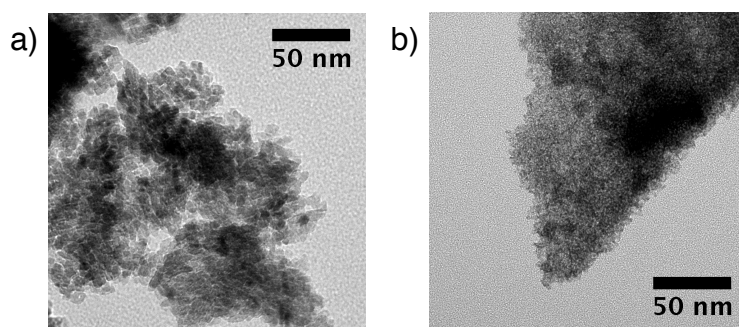


Figure 31: Bright field TEM images of TiO_2 (a) and IrO_2 (b) prepared by Adams method.

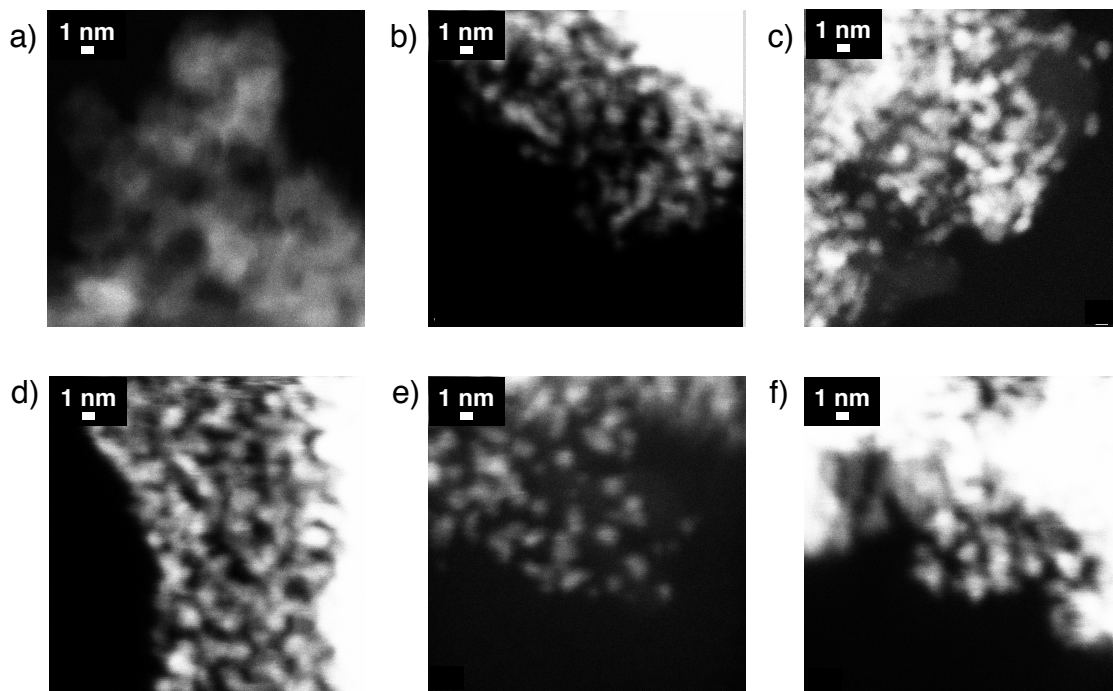


Figure 32: HAADF-STEM images of $\text{IrO}_2\text{-TiO}_2$ compositions with Ir contents of 0 (a), 20 (b), 40 (c), 60 (d), 80 (e) and 100 (f) $\text{mol}_M\%$.

Whilst iridium oxide has a variety of potential applications, particularly as a stable, conductive catalyst support in polymer electrolyte fuel cells^[58,59,198] and as an electrochemical oxygen evolution catalyst,^[71,175,180] the high cost of this material is considered a large disadvantage for commercial applications. Electrical conductivity is a key requirement for effective electrochemical cell operation and a minimal value of 0.1 S.cm^{-1} has been suggested for PEFC applications.^[38] With the aim of minimising Ir content, but maintaining sufficient conductivity for electrochemical applications, the electrical conductivity (σ) of $\text{IrO}_2\text{-TiO}_2$ as a function Ir content was investigated. It should be noted that in addition to the compositions described above, additional $\text{IrO}_2\text{-TiO}_2$ materials have been prepared by Adams method. Electrical conductivity values were determined by a 4-point probe method using compressed oxide powders of varying thicknesses (100 - 1000 μm). For each sample, three measurements were performed at varying thicknesses and the values averaged to give the numbers reported below. For all compositions except pure TiO_2 and 5% $\text{IrO}_2\text{-95}\%\text{TiO}_2$, chronoamperometric measurements were used to determine the current at set voltages from which resistance, resistivity and conductivity were determined. Electrical impedance spectroscopy (EIS) was used to determine the conductivities of pure TiO_2 and 5% $\text{IrO}_2\text{-95}\%\text{TiO}_2$. The electrical conductivity values of the varying compositions are reported in Table 14. To give an indication of the conductivity range provided by different batches of the same composition, the conductivities of two individual

batches were compared for samples with 20, 40, 60, 80 and 100 mol_M% Ir and these ranges are indicated in the table below.

Table 14: Conductivity values of various IrO₂-TiO₂ compositions

Ir content / mol _M %	σ / S.cm ⁻¹	σ range
0	10 ⁻⁸	-
5	10 ⁻⁶	-
20	0.0085	±0.0005
23	0.012	-
25	0.016	-
30	0.054	-
35	0.20	-
40	0.46	±0.02
50	0.44	-
60	0.64	±0.15
70	1.4	-
80	2.5	±0.12
100	4.0	±0.12

The conductivity values reported in Table 14 are better represented in Figure 33. This relationship shows that electrical conductivity increases with Ir content, as would be expected considering IrO₂ is a metallic-type conductor. Interestingly, this relationship is not linear and conductivity starts to significantly increase from 20 mol_M% Ir and sufficient conductivity for electrochemical applications is confidently reached at 40 mol_M%.^[38] Percolation theory is commonly employed to describe the properties of randomly organised networks. In 1990, McLachlan, Blaszkiewicz and Newnham introduced a percolation model for describing the conductivity of physical mixtures of low and high conductivity particles (Equation 1).^[199] This relationship shows that the conductivity of the oxide mixture is dependent on the volume fraction of the poor conductor (f), the percolation limit (f_c) and a variable exponent (t). The percolation limit is defined as the minimal volume fraction of the conductive phase required to form a conductive network through the mixture. Konstantinova et al. described the percolation limit as a function of the particle size ratio of the low and high conductivity particles assuming spherical nanoparticles with monodisperse size distribution, where inter-particle space is neglected.^[200] Assuming composition independent nanoparticle diameters of 5 and 1 nm for TiO₂ and IrO₂ respectively, the percolation limit of IrO₂-TiO₂ was determined to be 0.35. With this value in

hand, and the volume fraction of TiO_2 determined from the particle size and Ir : Ti ratio, the conductivity of these materials was plotted versus the experimental data. Using the non-linear least square method, the best fit between the experimental and model values was achieved with a t value of 3.3, which is reasonable considering literature reports.^[201–203] With this t value, the conductivity of $\text{IrO}_2\text{-TiO}_2$ can be predicted from the composition, or vice versa.

$$\sigma \propto \left(\frac{1-f}{f_c} \right) \quad (1)$$

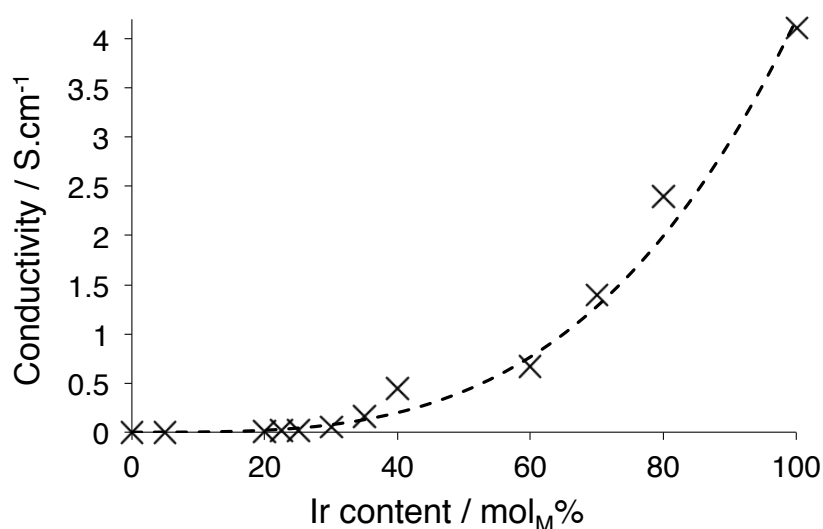


Figure 33: Conductivity-content relationship for $\text{IrO}_2\text{-TiO}_2$ comparison between experimental (cross) and percolation theory (line).

This investigation has shown that a simple reaction method, such as the oxidation of inorganic metal precursors by NaNO_3 , can produce high surface area materials with reproducible morphologies. XRD characterisation suggests a strong interaction between IrO_2 and TiO_2 , due to the additional formation of rutile TiO_2 in the presence of Ir. HAADF-STEM imaging revealed small IrO_2 nanoparticles are formed (ca. 1 nm in diameter) and their size is independent of composition. As expected, the electrical conductivity of these materials increases with Ir content. Interestingly an approximately exponential relationship between electrical conductivity and Ir content is found, which is effectively described using percolation theory. The minimal conductivity for electrochemical applications is achieved at 40 mol_M% Ir content.

4.3.2 IrO₂-MO_x: Comparing M = Ti, Sn and Nb

To investigate the influence of titanium oxide on the electrical conductivity of 40%IrO₂-60%TiO₂, compositional analogues were prepared by replacing TiO₂ with SnO₂ and Nb₂O₅, referred to as IrO₂-SnO₂ and IrO₂-NbO_{2.5} respectively. All materials were prepared by the same Adams method route using SnCl₂·5H₂O and NbCl₅ precursors with a constant metal : nitrate molar ratio.

XRD powder diffraction patterns of IrO₂-SnO₂ and IrO₂-NbO_{2.5} are shown in Figure 34 alongside those of their pure oxides prepared by the same Adams method. The XRD powder diffraction patterns clearly show that cassiterite SnO₂ is formed, whilst the broad diffraction pattern of Nb₂O₅ is difficult to interpret but is consistent with monoclinic Nb₂O₅. Similarly to what was observed for IrO₂-TiO₂ (Figure 29), the diffraction patterns of IrO₂-MO_x consist of broad peaks due to IrO₂. In the case of IrO₂-SnO₂ these peaks may also include contributions from cassiterite SnO₂, considering the similarity of the reference patterns.

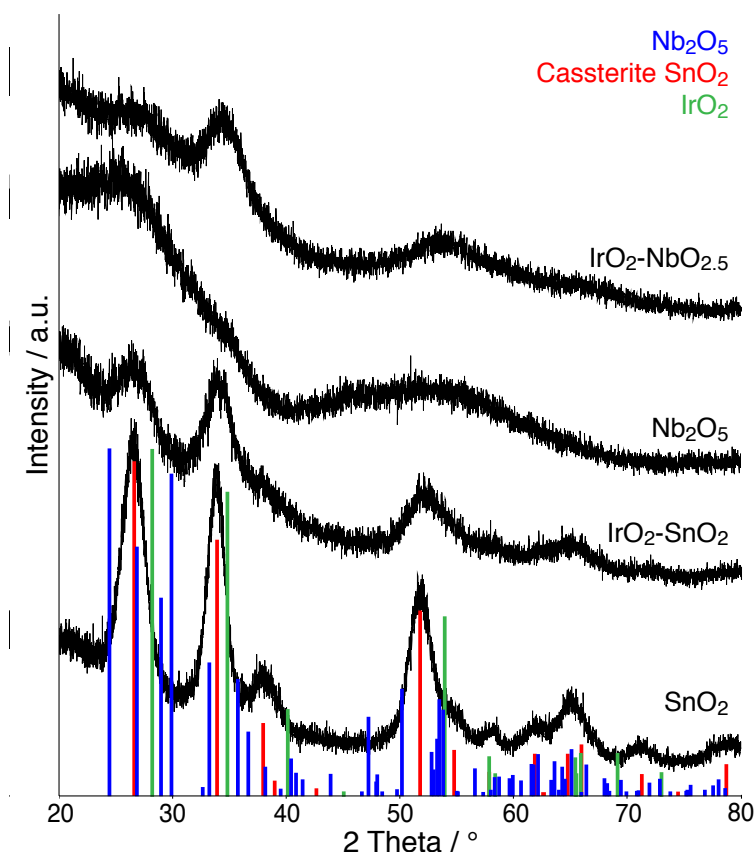


Figure 34: XRD powder diffraction patterns of SnO₂, IrO₂-SnO₂, Nb₂O₅ and IrO₂-NbO_{2.5} with reference patterns for IrO₂ (ICDD 00-015-0870), cassiterite SnO₂ (ICDD 00-077-0447) and monoclinic Nb₂O₅ (ICDD 00-080-2493).

The N_2 adsorption-desorption isotherms of IrO_2 - SnO_2 and IrO_2 - $NbO_{2.5}$ shown in Figure 35 are typical of nanoparticulate powders, due to their type II shape. Table 15 compares the surface areas of the IrO_2 - MO_x samples determined with BET theory. Both samples have high surface areas, however a clear trend can be observed when comparing surface area in molar terms, with this property increasing in the order IrO_2 - SnO_2 < IrO_2 - TiO_2 < IrO_2 - $NbO_{2.5}$.

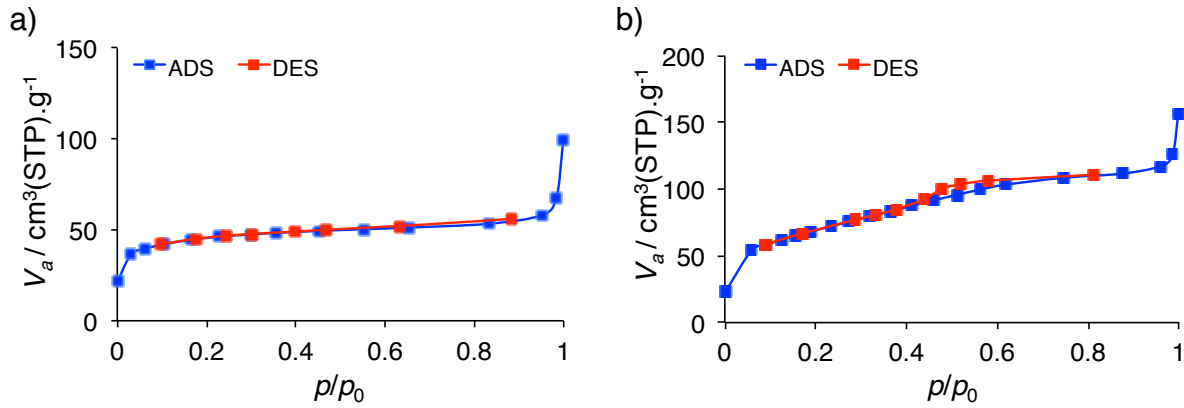


Figure 35: N_2 adsorption-desorption isotherms of IrO_2 - SnO_2 (a) and IrO_2 - $NbO_{2.5}$ (b).

Table 15: Surface Area of MO_x and IrO_2 - MO_x materials

Sample	$S_{BET} / m^2 \cdot g^{-1}$	$S_{BET} / m^2 \cdot mol^{-1}$
IrO_2 - SnO_2	163	29400
IrO_2 - TiO_2	251	34500
IrO_2 - $NbO_{2.5}$	248	42000

A greater insight into the morphology of these oxide materials is gained through bright field TEM imaging. TEM images of SnO_2 and Nb_2O_5 prepared by Adams method at 350 °C are shown in Figure 36. SnO_2 nanoparticles are approximately 5 nm in diameter, whilst the particle size of Nb_2O_5 is more difficult to determine. HAADF-STEM imaging of IrO_2 - SnO_2 and IrO_2 - $NbO_{2.5}$ (Figure 37) shows bright areas assigned to IrO_2 particles of comparable sizes (ca. 1 nm diameter) to IrO_2 - TiO_2 (Figure 32).

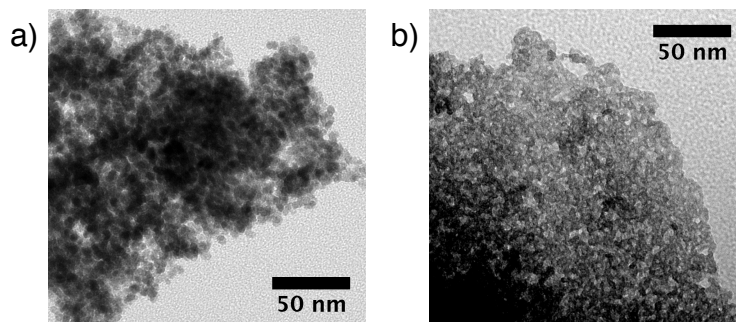


Figure 36: Bright Field TEM images of SnO_2 (a) and Nb_2O_5 (b) prepared by Adams method.

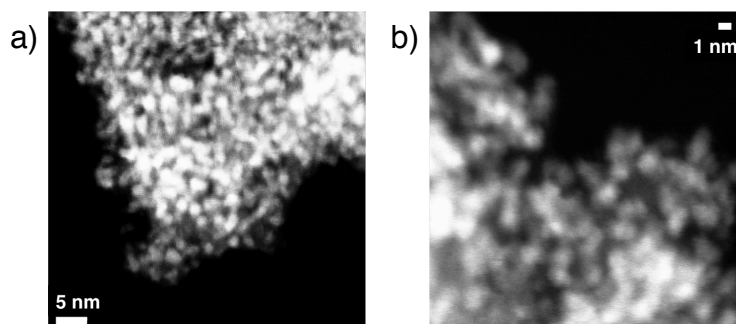


Figure 37: HAADF-STEM images of $\text{IrO}_2\text{-SnO}_2$ (a) and $\text{IrO}_2\text{-NbO}_{2.5}$ (b).

The characterisation described above has shown that all $\text{IrO}_2\text{-MO}_x$ materials ($M = \text{Ti}, \text{Sn}$ and Nb) are composed of small IrO_2 particles mixed with MO_x particles. Although there are some differences in surface area, all samples have surface areas of the same order of magnitude.

The electrical conductivity of these materials was determined by 4-point measurements of the compressed powders and are reported in Table 16 below. Despite the morphological similarity, the electrical conductivity results clearly show a large difference between $\text{IrO}_2\text{-TiO}_2$, $\text{IrO}_2\text{-SnO}_2$ and $\text{IrO}_2\text{-NbO}_{2.5}$. This suggests that MO_x plays a role in determining sample conductivity.

Table 16: Electrical Conductivity of the $\text{IrO}_2\text{-MO}_x$ materials

Sample	$\sigma / \text{S.cm}^{-1}$
$\text{IrO}_2\text{-SnO}_2$	0.029
$\text{IrO}_2\text{-NbO}_{2.5}$	0.037
$\text{IrO}_2\text{-TiO}_2$	0.46

One rationalisation for the difference in conductivity between $\text{IrO}_2\text{-TiO}_2$, $\text{IrO}_2\text{-SnO}_2$ and $\text{IrO}_2\text{-NbO}_{2.5}$ is the coverage of IrO_2 surfaces in the latter two compositions, which would be expected to limit electron transport between nanoparticles. This hypothesis was investigated by CO_2 temperature programmed desorption (CO_2 -TPD) measurements. In this method, CO_2 is absorbed on the oxide surface at low temperatures and desorbed by increasing the sample temperature. Therefore the signal of the thermal conductivity detector (TCD) is a unique description of the temperature dependent interaction of the material surface with CO_2 . $\text{IrO}_2\text{-TiO}_2$, $\text{IrO}_2\text{-SnO}_2$ and $\text{IrO}_2\text{-NbO}_{2.5}$, as well as their pure oxide components were characterised by CO_2 -TPD, the results of which are shown in Figure 38. All materials show an initial increase in TCD signal around 0 - 100 °C and an additional higher temperature signal from 300 °C upwards.

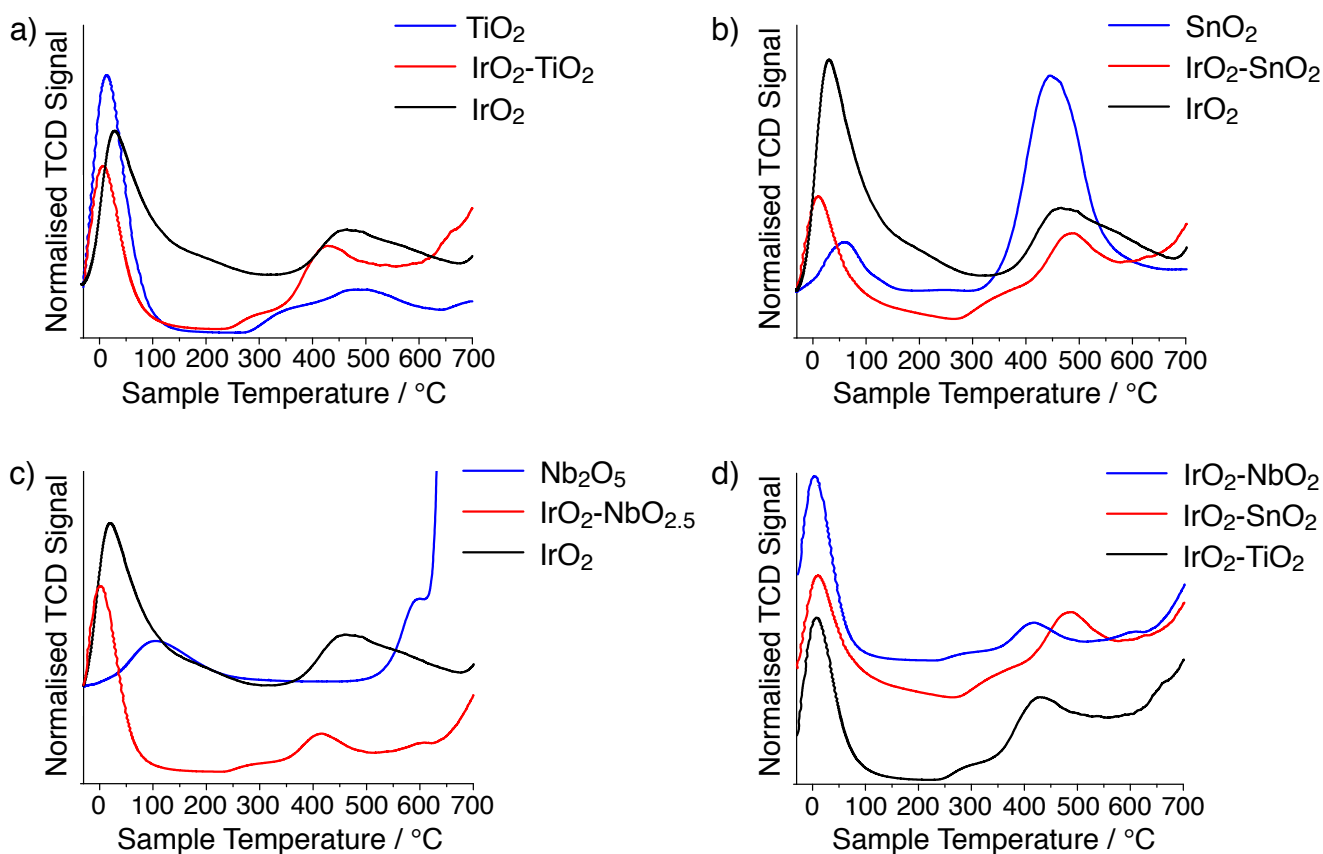


Figure 38: CO_2 -TPD results for $\text{IrO}_2\text{-TiO}_2$ (a), $\text{IrO}_2\text{-SnO}_2$ (b), $\text{IrO}_2\text{-NbO}_{2.5}$ (c) with their respective pure oxides and a direct comparison of $\text{IrO}_2\text{-MO}_x$ materials (d).

Comparing the low temperature TCD signals of all $\text{IrO}_2\text{-MO}_x$ materials shows that this peak is shifted to a lower temperature with respect to IrO_2 . TiO_2 and SnO_2 show low temperature

peaks similar to IrO_2 with a maximum around 20 °C, whilst that of Nb_2O_5 has a maximum around 120 °C. The similarity of the $\text{IrO}_2\text{-MO}_x$ and MO_x CO_2 -TPD signals complicates the assignment of IrO_2 surface contributions. However CO_2 -TPD reveals a significant contribution of IrO_2 to the $\text{IrO}_2\text{-NbO}_{2.5}$ surface specific signal, supported by the similarity of the low temperature peak to that of IrO_2 . Interestingly, the CO_2 -TPD results of $\text{IrO}_2\text{-TiO}_2$, $\text{IrO}_2\text{-SnO}_2$ and $\text{IrO}_2\text{-NbO}_{2.5}$ are remarkably similar, particularly at low temperatures (Figure 38d). The similarity of these signals and the difference in electrical conductivities (Table 16) suggests the surface does not make a large contribution to overall conductivity. An alternative explanation for the observed conductivity difference between the $\text{IrO}_2\text{-MO}_x$ materials may be due to the improved particle connectivity for $\text{IrO}_2\text{-TiO}_2$. XRD characterisation of $\text{IrO}_2\text{-TiO}_2$ confirmed the presence of rutile TiO_2 in addition to anatase TiO_2 , the latter of which is formed as a single phase in the absence of Ir (Figure 30). This shows a clear effect of Ir on TiO_2 growth and could be an indication of improved $\text{IrO}_2\text{-TiO}_2$ particle connectivity.

This investigation has shown that $\text{IrO}_2\text{-SnO}_2$ and $\text{IrO}_2\text{-NbO}_{2.5}$, with Ir contents of 40 mol_M%, are yielded as high surface area powders using the one-pot Adams method route described for $\text{IrO}_2\text{-TiO}_2$. XRD shows similar diffraction patterns for all samples, which are dominated by broad peaks consistent with IrO_2 . HAADF-STEM imaging indicates that small IrO_2 particles are formed, as observed previously. Despite their morphological similarities, electrical conductivity measurements show that $\text{IrO}_2\text{-TiO}_2$ has an electrical conductivity one order or magnitude higher than $\text{IrO}_2\text{-SnO}_2$ and $\text{IrO}_2\text{-NbO}_{2.5}$. CO_2 -TPD measurements confirm the presence of surface contributions from IrO_2 , particularly for $\text{IrO}_2\text{-NbO}_{2.5}$, therefore surface coverage of IrO_2 does not explain the decreased electrical conductivity of $\text{IrO}_2\text{-SnO}_2$ and $\text{IrO}_2\text{-NbO}_{2.5}$. The increased conductivity of $\text{IrO}_2\text{-TiO}_2$ may be explained by improved particle connectivity, as XRD measurements have indicated an influence of Ir on TiO_2 particle growth (Figure 30).

4.3.3 Chlorine-free Iridium Titanium Oxide

All Ir containing materials discussed previously were prepared from an iridium chloride precursor (IrCl_3). Unsurprisingly, the characterisation of $\text{IrO}_2\text{-TiO}_2$ by energy dispersive X-ray spectroscopy (EDX) indicates the presence of chlorine contamination in these materials (Figure 39), likely due to surface chloride species. Concerning the potential application of $\text{IrO}_2\text{-TiO}_2$ in electrocatalytic oxygen evolution, the presence of surface chloride species can complicate interpretation of results due to the competing chlorine evolution. Therefore efforts were made to remove the chlorine contamination of these materials, whilst maintaining sufficient electrical conductivity for electrochemical applications.

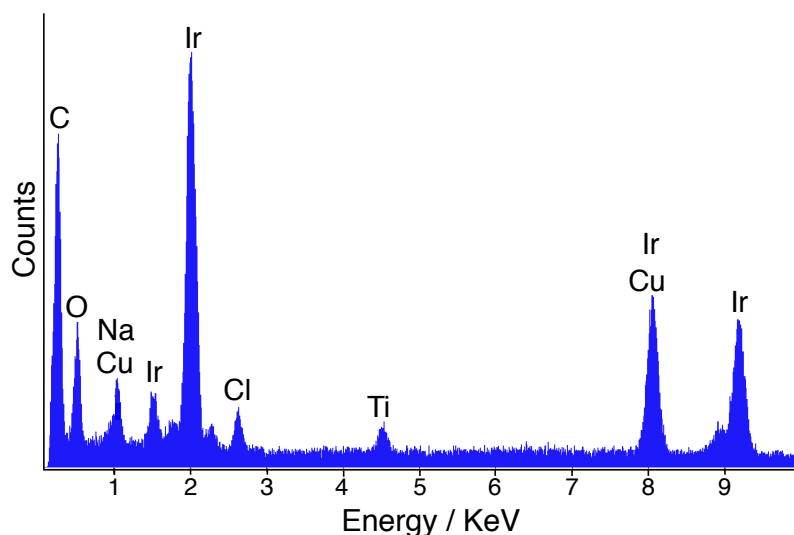


Figure 39: EDX spectrum of 40%IrO₂-60%TiO₂ prepared from IrCl₃.

Whilst increasing the reaction temperature to 500 °C did significantly decrease chloride contamination (Figure 40), electrical conductivity was compromised (Table 17). HAADF-STEM imaging shows that the decrease in conductivity is likely linked to the observed change in morphology after reaction at a higher temperature (Figure 40a).

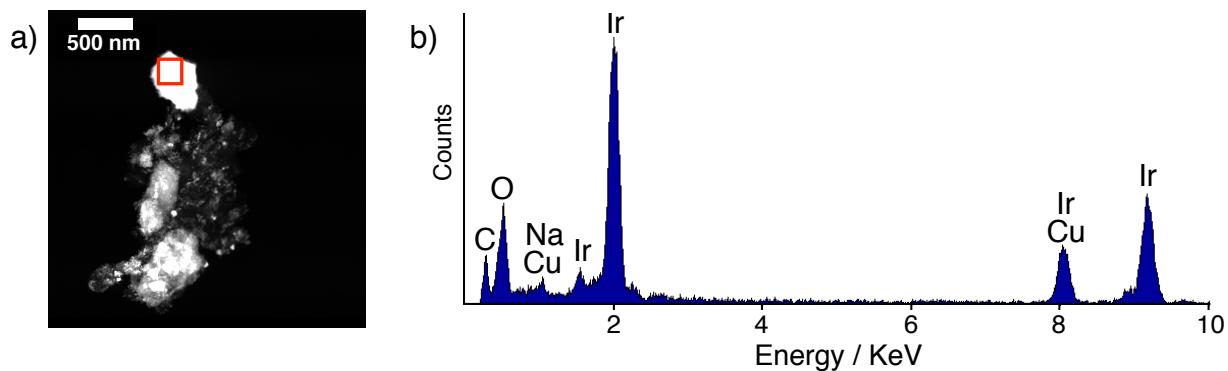


Figure 40: HAADF-STEM image of 40%IrO₂-60%TiO₂ prepared at 500 °C (a) and EDX spectrum (b). The red square indicates the area over which the EDX spectrum was recorded.

Table 17: Electrical Conductivity of the IrO₂-TiO₂ at different reaction temperatures

Reaction Temperature / °C	σ / S.cm ⁻¹
350	0.46
500	0.05

An alternative method to prepare chlorine-free IrO₂-TiO₂ is to use a chlorine-free Ir precursor. Therefore a variety of IrO₂-TiO₂ materials were prepared by replacing IrCl₃ with Ir(acac)₃ (acac = acetylacetonate). The X-ray diffraction patterns of the chlorine-free compositions are similar to those measured for the chlorinated analogs (Figure 29), with broad diffraction peaks complicating further interpretation (Figure 41). HAADF-STEM imaging of 30, 40 and 70 mol_M% Ir content samples shows similar morphologies are obtained as observed previously (Figure 32) with ca. 1 - 2 nm diameter IrO₂ particles mixed with larger TiO₂ particles (Figure 42).

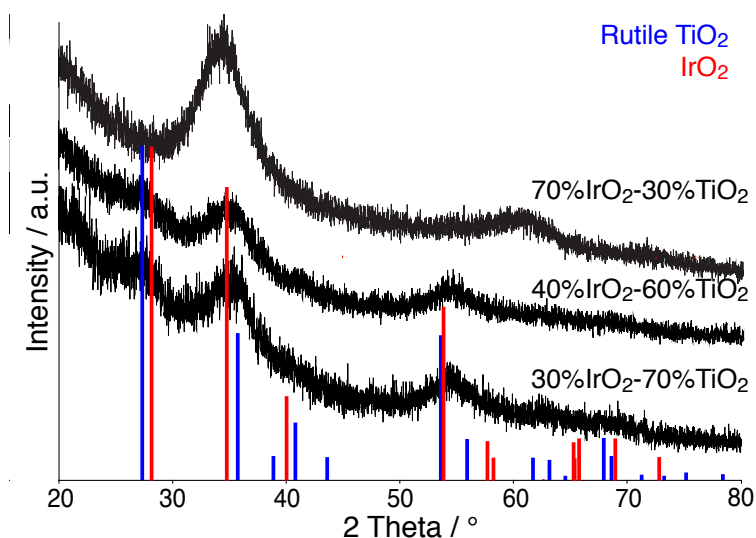


Figure 41: XRD powder diffraction patterns of IrO₂-TiO₂ prepared from Ir(acac)₃ (30, 40 and 70 mol_M% Ir content) with reference patterns of rutile TiO₂ (ICDD 00-086-0147) and IrO₂ (ICDD 00-015-0870).

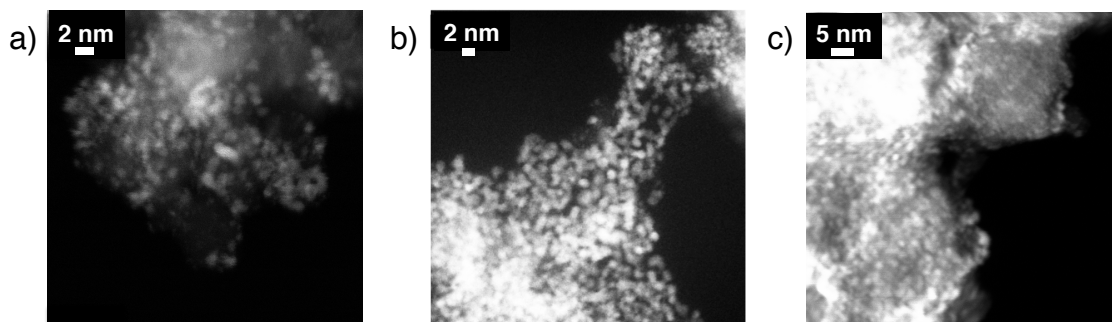


Figure 42: HAADF-STEM images of IrO₂-TiO₂ prepared from Ir(acac)₃ with 30 (a), 40 (b) and 70 (c) mol_M% Ir content.

Table 18 compares the surface areas and electrical conductivities of the chlorine containing and chlorine-free analogs. Surface areas, determined by N₂ adsorption-desorption measurements analysed with BET theory, show comparable surface areas are achieved with both precursors. Comparing electrical conductivities of samples of the same composition shows that with an Ir content of 30 and 40 mol_M% similar electrical conductivities are achieved, whilst the conductivity of 70 mol_M% Ir sample prepared from Ir(acac)₃ is lower than expected, although still sufficient for electrochemical applications.^[38]

Table 18: Electrical Conductivity of the IrO₂-TiO₂ prepared from different iridium precursors

Ir content / mol _M %	Ir precursor	S_{BET} / m ² .g ⁻¹	σ / S.cm ⁻¹
30	IrCl ₃	230	0.05
	Ir(acac) ₃	230	0.04
40	IrCl ₃	251	0.46 ± 0.02
	Ir(acac) ₃	245	0.26 ± 0.02
70	IrCl ₃	291	1.4
	Ir(acac) ₃	190	0.2

This investigation has shown that chlorine-free IrO₂-TiO₂ materials can be prepared from iridium acetylacetonate with morphologies, which are comparable to their chlorinated analogs. High surface area materials are yielded, with HAADF-STEM imaging showing small IrO₂ particles are formed as with iridium chloride. This demonstrates the inherent ability of this synthetic method to yield small IrO₂ particles.

4.3.4 Activity and Stability of Chlorine-free Iridium Titanium Oxide in Electrocatalytic Oxygen Evolution

Chlorine-free iridium titanium oxide ($\text{IrO}_2\text{-TiO}_2(\text{acac})$) can be easily prepared by the replacement of IrCl_3 with $\text{Ir}(\text{acac})_3$, yielding high surface area powders with comparable morphologies and electrical conductivities to their chlorinated analogs. The chlorine-free nature of $\text{IrO}_2\text{-TiO}_2(\text{acac})$ is a major advantage for OER applications, considering the possibility of competing chlorine evolution. Consequently, the activity and stability of two $\text{IrO}_2\text{-TiO}_2(\text{acac})$ compositions (40 and 70 mol_M% Ir) were investigated as electrochemical oxygen evolution electrocatalysts in acidic media and compared to pure IrO_2 prepared by Adams method as well as two IrO_2 -based commercial samples. It is important to note that all homemade materials are prepared from $\text{Ir}(\text{acac})_3$. The materials investigated are detailed in the Table 19, where temperature refers to the reaction temperature of all samples, except for homemade IrO_2 (28 m².g⁻¹), which was further calcined under air-flow at 600 °C after reaction at 500 °C. $\text{IrO}_2\text{-TiO}_2$ compositions are also denoted as X% IrO_2 -(100-X)% TiO_2 , where percentage refers to mol_M%.

Table 19: OER catalysts

Producer	Composition	Temperature / °C	S_{BET} / m ² .g ⁻¹	Name
Sigma Aldrich	IrO_2	-	3	$\text{IrO}_2(3)$
Homemade	IrO_2	600	28	$\text{IrO}_2(28)$
Homemade	IrO_2	350	150	$\text{IrO}_2(150)$
Umicore AG & Co.	70% IrO_2 -30% TiO_2	-	34	$\text{IrO}_2\text{-TiO}_2(34)$
Homemade	70% IrO_2 -30% TiO_2	350	190	$\text{IrO}_2\text{-TiO}_2(190)$
Homemade	40% IrO_2 -60% TiO_2	350	245	$\text{IrO}_2\text{-TiO}_2(245)$

A variety of IrO_2 materials are compared with varying surface areas, where the reaction temperature was increased and an additional calcination treatment performed to decrease the surface area of homemade IrO_2 . Homemade $\text{IrO}_2\text{-TiO}_2$ with a comparable Ir : Ti ratio to the commercial sample from Umicore AG is also investigated, in addition to a lower Ir content sample.

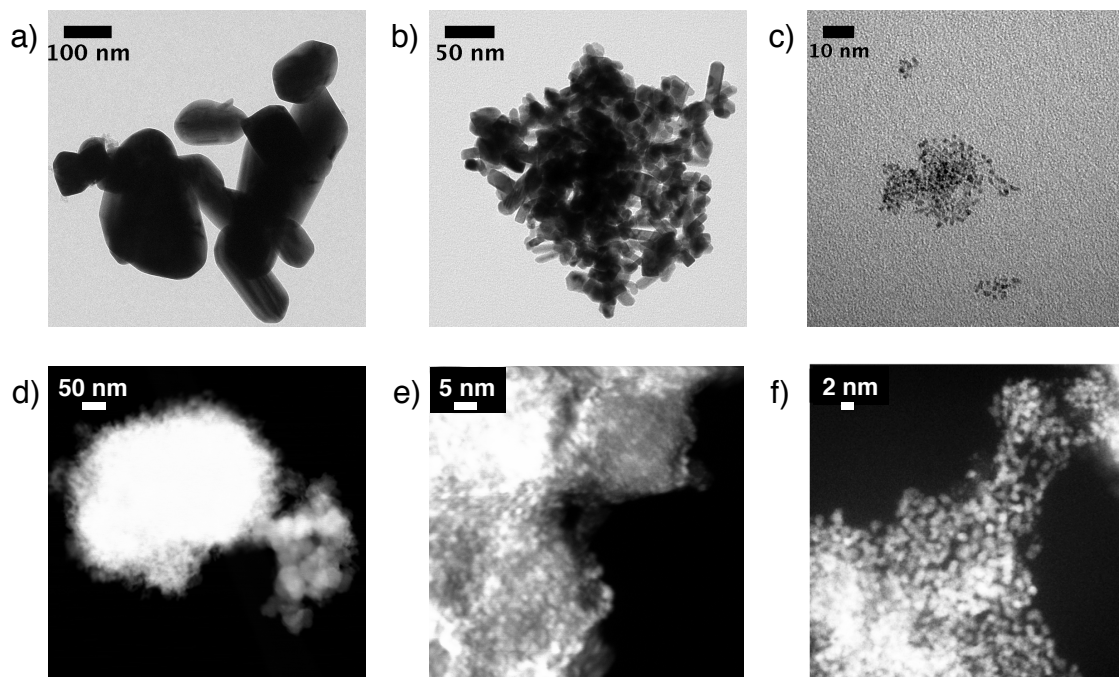


Figure 43: Bright field TEM images of IrO₂(3) (a), IrO₂(28) (b) and IrO₂(150) (c). HAADF-STEM images of IrO₂-TiO₂(34) (d), IrO₂-TiO₂(190) (e) and IrO₂-TiO₂(245) (f).

A range of electrochemical techniques are used to evaluate the suitability of these materials as oxygen evolution catalysts. For all measurements, the catalyst powders were combined with Nafion[®], a perfluorosulfonic acid proton conducting polymer, and deposited on a glass carbon rotating disk electrode. Rotating disk electrode experiments are used to reduce mass transfer limitations by inducing a convective flow of the acidic electrolyte (0.1 M HClO₄) to the electrode surface. It is important to note that all reported potentials are with reference to the Reversible Hydrogen Electrode (RHE).

Cyclic voltammetry is used to identify redox processes occurring on the catalyst surface. With this technique, the potential is linearly swept at a defined rate over a potential window centered around the standard oxygen evolution potential (1.23 V). Potential specific changes in current can give an indication of any electrochemical processes taking place. Tafel plots can be constructed to define the relationship between potential and current, which can be related to the reaction mechanism.^[175] Chronoamperometric measurements are used to construct the Tafel plots where the current is recorded at a specific potential, which is held for a defined amount of time (10 s).^[175] Catalyst activities are compared using an activity descriptor, which is defined as the potential required to achieve a current density of 10 A.g_{Ir}⁻¹.^[175] This value can be directly determined from the Tafel plot or by extrapolation of the Tafel slope. The lower the potential required to reach 10 A.g_{Ir}⁻¹, the greater the catalyst activity. The current produced per electrochemically active surface area (A.cm⁻²) could also be used as an activity descriptor

however, the determination of active surface area is non-trivial for many OER catalysts.^[175] Due to difficulties determining Ir content from elemental analysis, nominal Ir loadings are used to determine current density. Finally, catalyst stability is evaluated by recording the variation in current generated at a set voltage during potential cycling under conditions, that may trigger oxidation or dissolution of the catalyst. Decreases in current as a result of potential cycling may indicate catalyst degradation.

The homemade catalysts were characterised by cyclic voltammetry, where the voltage is swept between 1.4 and 1.0 V at a rate of 50 mV.s^{-1} . Figure 44 displays the cyclic voltammograms (CVs) of the homemade catalysts. The shape of all CVs are similar, specific redox couples are not observed, with the almost square CV shape likely due to capacitive currents. The varying current magnitude is likely due to variations in capacitance from varying composition and particle size.

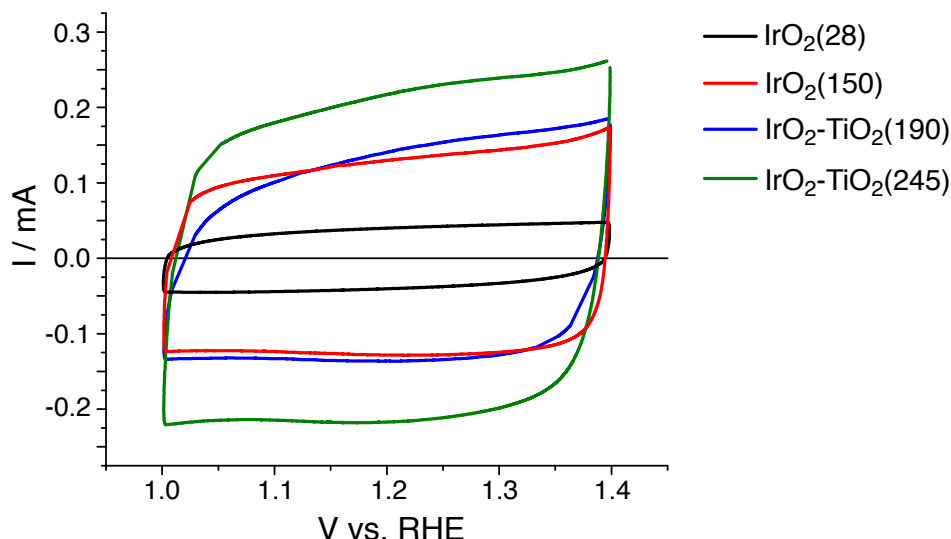


Figure 44: Cyclic voltammograms of the homemade OER catalysts.

Tafel plots are commonly implemented to compare electrocatalysts and can be used to gain an insight into the variation of potential with current.^[175] When temperature is constant, the Tafel slope varies as a function of the reaction mechanism^[175] and can indicate switches in reaction mechanism for different electrocatalysts. Figure 45 compares the Tafel plots of the investigated OER catalysts. The slope of all Tafel plots are similar, indicating similar oxygen evolution mechanisms are operating, which would be expected considering IrO₂ as the active electrocatalyst.

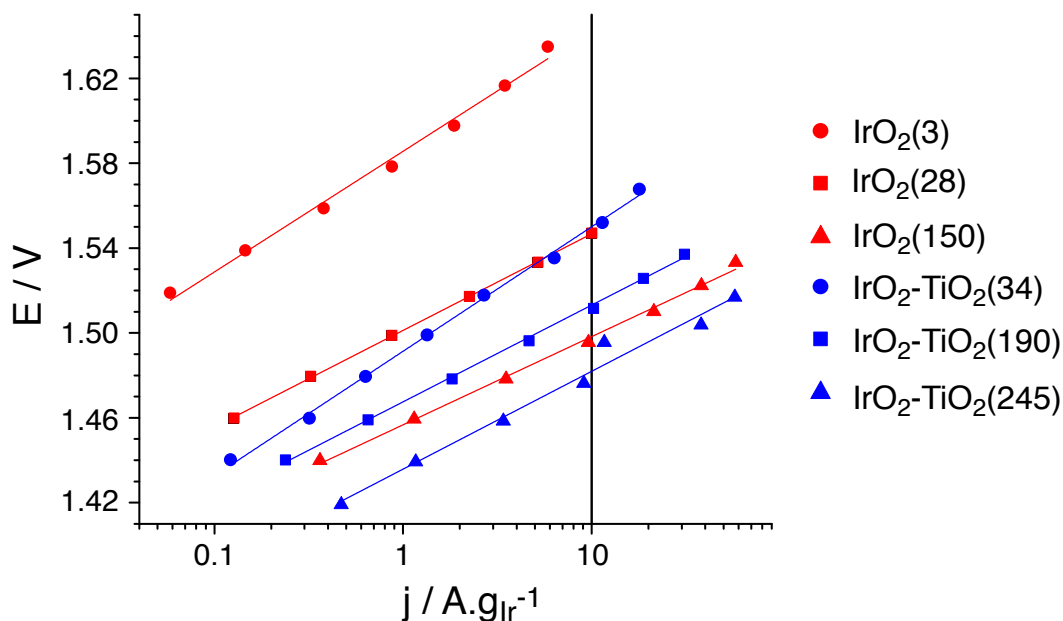


Figure 45: Tafel plots of homemade and commercial materials investigated as oxygen evolution catalysts.

The OER activities of these various catalysts were evaluated by comparing the potential required to achieve a current of $10 \text{ A.g}_{\text{Ir}}^{-1}$.^[175] These values are obtained from the Tafel plots previously reported (Figure 45) and are plotted in Figure 46. Comparing the pure IrO_2 catalysts shows that decreasing particle size vastly reduces potential (Figure 43). Interestingly, $\text{IrO}_2\text{-TiO}_2(190)$ has a lower onset potential than its compositional counterpart, $\text{IrO}_2\text{-TiO}_2(34)$, which may be explained by the reduced IrO_2 particle size. EDX mapping of a sample of Pt nanoparticles supported on $\text{IrO}_2\text{-TiO}_2(34)$ indicates large particles of IrO_2 (Figure A16). Furthermore, $\text{IrO}_2\text{-TiO}_2(245)$ has a comparable onset potential to $\text{IrO}_2(150)$ and $\text{IrO}_2\text{-TiO}_2(190)$. Considering the morphological similarity of these samples, the potential to achieve $10 \text{ A.g}_{\text{Ir}}^{-1}$ is very likely linked to IrO_2 particle size.

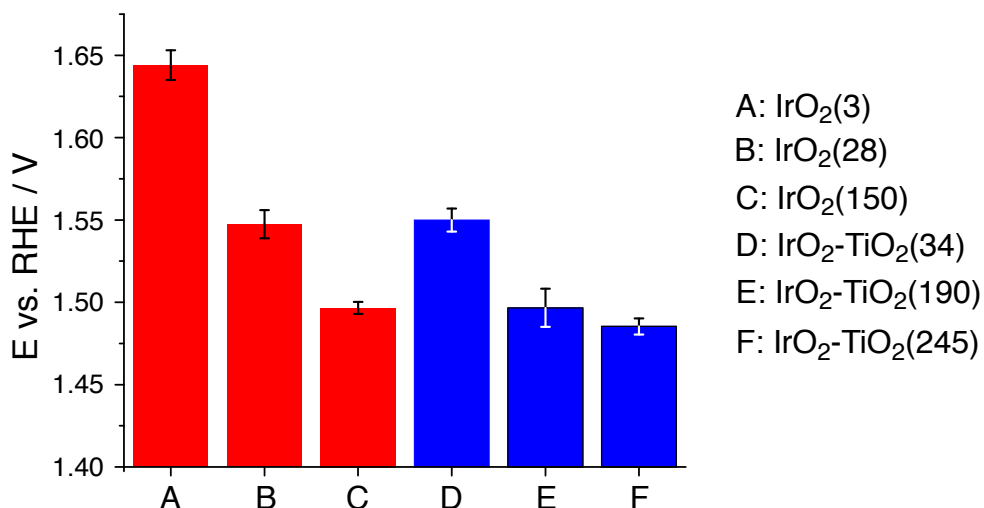


Figure 46: Potentials required to achieve a current density of $10 \text{ A.g}_{\text{Ir}}^{-1}$ for a variety of OER catalysts.

To help rationalise these observed differences in activity, IrO₂(28), IrO₂(150) and IrO₂-TiO₂(245) were further characterised by X-ray absorption spectroscopy (XAS). The X-ray absorption near edge structure (XANES) spectroscopy results compare the white line energies of the Ir L_{III}-edge. From this data, presented in Figure 47 and tabulated in Table 20, there is a clear decrease in energy in the order IrO₂(28) > IrO₂-TiO₂(245) > IrO₂(150). This shows that the average oxidation state of Ir in the samples prepared at 350 °C is lower than that prepared at a higher temperature.

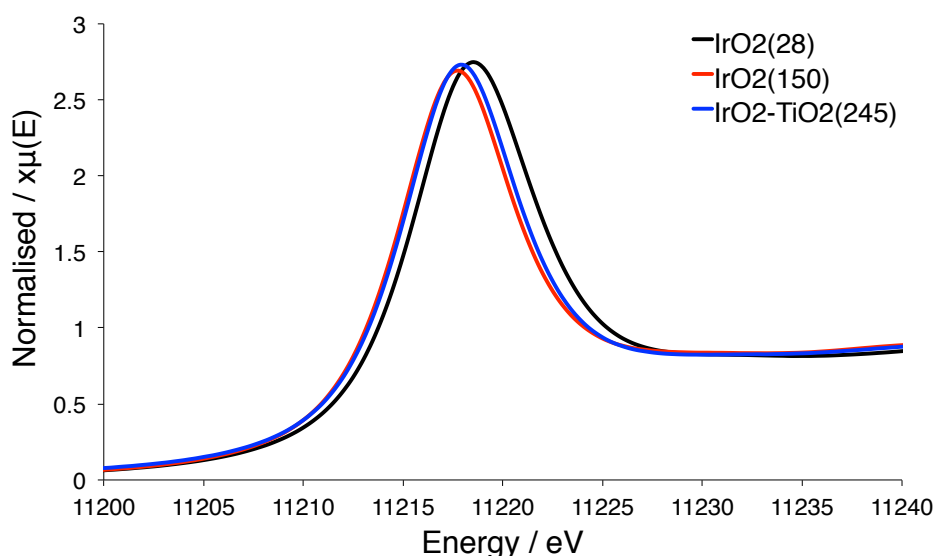
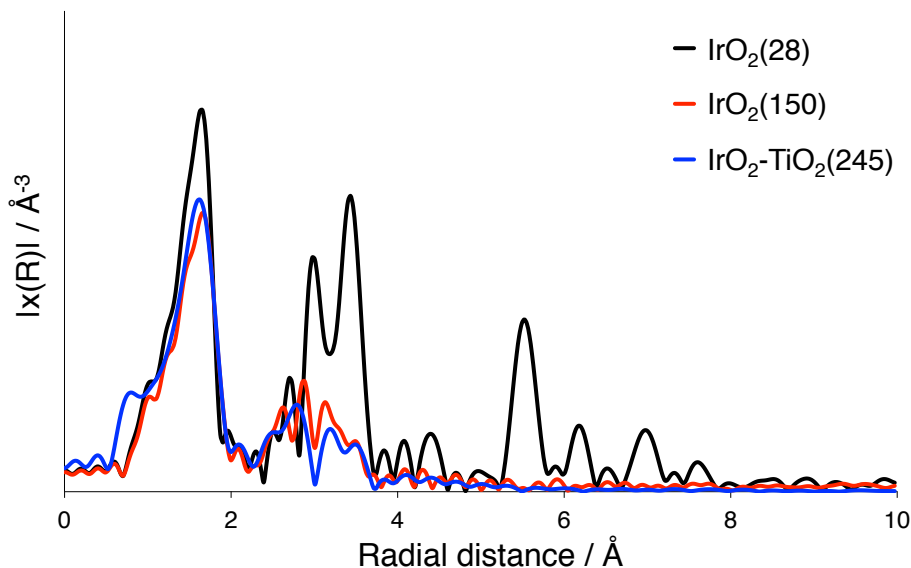


Figure 47: XANES spectra of IrO₂(28), IrO₂(150) and IrO₂-TiO₂(245).

Table 20: White line energies

Sample	Ir L_{III} -edge energy / eV
IrO ₂ (28)	11216.0
IrO ₂ -TiO ₂ (245)	11215.5
IrO ₂ (150)	11215.3

Interestingly, qualitative comparison of the extended X-ray absorption fine structure (EXAFS) spectroscopy results (Figure 48) show that the radial distribution functions (RDF) of IrO₂(150) and IrO₂-TiO₂(245) are similar, whilst that of IrO₂(28) is notably different. Peaks in the RDF of IrO₂(28) can be observed until 8 Å, whilst the RDF of the high surface area samples diminishes around 4 Å, indicating a decrease in order. Interestingly, the RDF of IrO₂(150) and IrO₂-TiO₂(245) show similarities to published spectra of iridium oxohydroxide.^[204–206] Considering the role played by surface hydroxide species in many of the proposed OER mechanisms,^[176] the presence of Ir-OH species would be consistent with the increased OER activity observed for these samples.

**Figure 48:** EXAFS spectra of IrO₂(28), IrO₂(150) and IrO₂-TiO₂(245).

To further probe the presence of oxohydroxide species, the EXAFS spectra were fitted using a rutile IrO₂ structure to obtain the average Ir-O bond distance over six Ir-O scattering paths. The EXAFS fit and tabulated parameters can be found in Appendix 3. Table 21 details the

determined Ir-O bond distances for IrO₂(28), IrO₂(150) and IrO₂-TiO₂(245). Interestingly, the bond distances vary in a similar way to that observed for the white line energies, with Ir-O distance increasing in the order IrO₂(28) > IrO₂-TiO₂(245) > IrO₂(150). It is known that Ir-O bond distances for Ir⁴⁺ and Ir³⁺ oxidation states are 1.97 and 2.02 Å respectively.^[205,206] Therefore the increase in bond length is in agreement with the white line energies, which suggest the Ir centers in IrO₂-TiO₂ and IrO₂(150) are more reduced with respect to IrO₂(28). This increase in bond length further supports the presence of iridium oxohydroxide species in IrO₂-TiO₂(245) and IrO₂(150).

Table 21: Ir-O bond distances

Sample	Ir-O bond distance / Å
IrO ₂ (28)	1.985
IrO ₂ -TiO ₂ (245)	2.013
IrO ₂ (150)	2.022

In summary, the characterisation of IrO₂(28), IrO₂(150) and IrO₂-TiO₂(245) by X-ray absorption spectroscopy has shown that the latter two materials are reduced in comparison to IrO₂(28). This is likely due to the reduced reaction temperature for IrO₂(150) and IrO₂-TiO₂(245), which leads to smaller IrO₂ particles that are more amorphous in character and which likely contain iridium oxohydroxide species (IrO_x(OH)_y). Considering these results together with the potentials measured (Figure 46), the formation of a more amorphous oxide as well as iridium oxohydroxide species likely play a role in reducing OER potential. The hydroxylation of IrO₂ may facilitate OER more readily, as surface hydroxides are key intermediates in oxygen evolution.^[70,175,176]

Activity parameters and XAS characterisation have shown that both homemade IrO₂ and IrO₂-TiO₂ catalysts have exceptionally high activities for electrochemical oxygen evolution in comparison to commercial IrO₂ and IrO₂-TiO₂ catalysts. The next stage of the electrochemical investigations involves determining the stability of these catalysts. The most active catalysts were chosen for this study, namely IrO₂(28), IrO₂(150), IrO₂-TiO₂(190) and IrO₂-TiO₂(245). The stability of these samples was determined during 500 potential cycles between 1 and 1.6 V, where current density was recorded at 50 cycle intervals and normalised with respect to the initial value. Figure 49 compares the stabilities of the samples of interest.

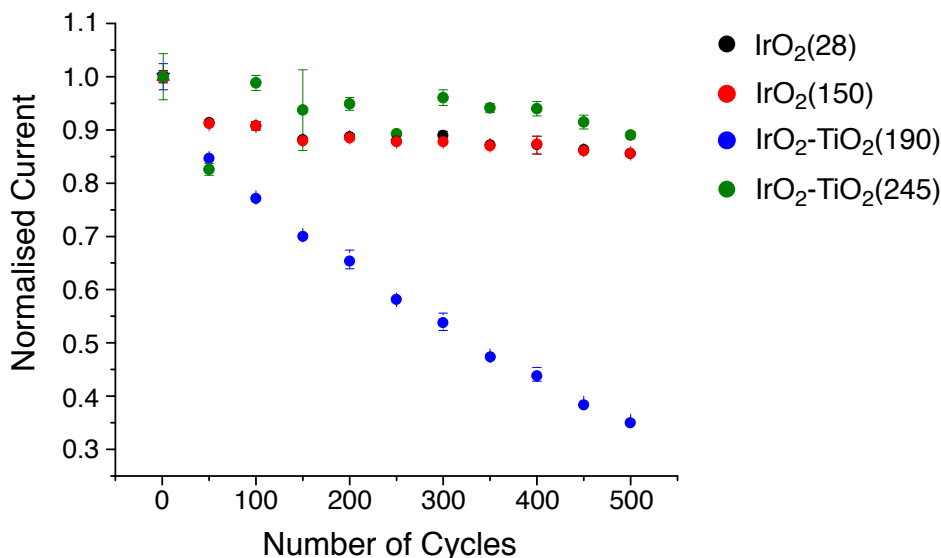


Figure 49: OER stability of IrO₂-TiO₂ during potential cycling.

The variation of normalised current over the range of 500 potential cycles indicates that IrO₂-TiO₂(245), IrO₂(28), IrO₂(150) have similar stabilities, with that of the former being marginally improved. IrO₂-TiO₂(190) shows the largest drop in normalised current after 500 cycles. This drop in current may be explained by Ostwald ripening, a common degradation mechanism for electrocatalysts. However, a similar trend would be expected for IrO₂(150), which is not observed. Additionally the good stability of IrO₂-TiO₂(245) confirms that the presence of TiO₂ is not the cause of the low stability of IrO₂-TiO₂(190). Further characterisation, particularly scanning electron microscopy (SEM) imaging of the electrodes before and after potential cycling, would enable better understanding of the degradation mechanisms of these OER catalysts and would be an interesting subject for future work. Nevertheless IrO₂-TiO₂(245) has shown to be a very active and stable OER catalyst with low Ir content.

4.4 Conclusion

This chapter describes the preparation of iridium titanium oxide materials by a simple one-pot Adams method reaction. This reaction leads to IrO₂-TiO₂ materials, which are mixtures of small IrO₂ and TiO₂ particles. XRD studies indicate a shift in TiO₂ phase in the presence of Ir. Furthermore HAADF-STEM imaging of variable compositions demonstrates the inherent nature of this method to yield small IrO₂ particles approximately 1 nm in diameter independent of Ir content. The relationship between electrical conductivity and Ir content has been modelled using percolation theory. Sufficient conductivity for electrical applications is achieved at 40 mol_M% Ir content.

This reaction method has been extended to cover the preparation of $\text{IrO}_2\text{-MO}_x$ materials, where $M = \text{Sn}$ or Nb , with 40 mol_M% Ir. HAADF-STEM imaging reveals similar morphologies with small IrO_2 particles present. Despite their apparent morphological similarity, both $\text{IrO}_2\text{-MO}_x$ materials have lower electrical conductivities in comparison to $\text{IrO}_2\text{-TiO}_2$. These ternary compositions, as well as their pure component oxides were characterised by $\text{CO}_2\text{-TPD}$, which indicates that IrO_2 surface coverage is not the reason for the observed drop in conductivity. The influence of the TiO_2 phase shown for $\text{IrO}_2\text{-TiO}_2$ may indicate strong particle connectivity, which could contribute to its superior conductivity. These results indicate that MO_x plays a role in determining the conductivity of $\text{IrO}_2\text{-MO}_x$ materials.

Replacing the IrCl_3 precursor by $\text{Ir}(\text{acac})_3$ yields $\text{IrO}_2\text{-TiO}_2$ materials with comparable morphologies and conductivities without chloride contamination. Application of chlorine-free IrO_2 and $\text{IrO}_2\text{-TiO}_2$ compositions in electrochemical oxygen evolution showed that these materials are more active in comparison to commercial alternatives. X-ray absorption spectroscopy reveals that the IrO_2 particles produced by reaction with NaNO_3 at 350 °C are more amorphous in nature in comparison to IrO_2 prepared at a higher temperature. Additionally the presence of iridium oxohydroxide species may account for the improvement in activity. In comparison to commercial iridium titanium oxide, the homemade materials have significantly higher surface areas. Although comparable activities are achieved with high surface area IrO_2 , the application of $\text{IrO}_2\text{-TiO}_2$ materials allows for the minimisation of iridium content, which would dramatically reduce the cost of PEMWEs. Comparing the activity of 40 and 70 mol_M% Ir samples have shown that activity is independent of Ir content. Future work should include further optimisation of Ir content and the investigation of $\text{IrO}_2\text{-TiO}_2$ in membrane electrode assemblies.

4.5 Experimental Details

4.5.1 General

$\text{IrCl}_3 \cdot 3\text{H}_2\text{O}$ (99.9%), $\text{Ir}(\text{acac})_3$ (98%) and NbCl_5 (99%) were purchased from Strem Chemicals, whilst $\text{TiOSO}_4 \cdot 0.6\text{H}_2\text{SO}_4 \cdot 1.3\text{H}_2\text{O}$ (99.99%), $\text{SnCl}_4 \cdot 5\text{H}_2\text{O}$ (99%), NaNO_3 (> 99.0%), concentrated H_2SO_4 and Nafion[®] solution were purchased from Sigma Aldrich. Distilled water was further purified using a Merck Millipore Synergy Ultrapure Water System and had a resistivity of 18.2 M Ω .cm at 25 °C. N_2 adsorption-desorption analysis was conducted using a BEL-Mini device supplied by BEL Japan Inc. All samples were pre-treated at 150 °C under vacuum for 16 h on a BEL-Prep machine also from BEL Japan Inc. Results were fitted using BEL-Master programme and BET theory. The XRD pattern of 40% IrO_2 -60% TiO_2 (detailed in Figure 30) was recorded on a PANalytical X-pert PRO-MPD diffractometer (Cu K α radiation, $\lambda = 1.54187$

Å) and is a combination of 200 scans. Rietveld analysis was however not possible on these samples due to several overlaps of broad features. All other measurements are single scans recorded on a Stoe STADI P diffractometer (Cu K α radiation, $\lambda = 1.54051$ Å). Bright Field TEM images were recorded using a Philips CM12 transmission electron microscope. HAADF-STEM imaging was performed using an aberration corrected Hitachi HDCS2700CS microscope. Electrical conductivity values were determined from powder disks under 0.625 MPa pressure with thicknesses in the range 100 - 1000 μm . For pure TiO_2 and 5% IrO_2 -95% TiO_2 conductivity values were determined using Electrical Impedance Spectroscopy. In the case of all other Ir containing samples, chronoamperometric measurements were used; where the current was recorded for a range of voltages (0.001 - 0.1 V) and conductivity subsequently calculated using Ohm's law. Electrical conductivity was determined for three pellet thicknesses and averaged to give the reported values. XAS experiments were performed on the Super XAS beamline at the Swiss Light Source (Paul Scherrer Institute). The SLS is a third generation synchrotron, which operates under top up mode, 2.4 GeV electron energy and a current of 400 mA. The SuperXAS beamline is positioned on one of the three super-bent ports. Catalyst loading was in the range 0.3 - 0.7 mg and samples were measured in transmission most at room temperature.

4.5.2 Representative preparation of 40% IrO_2 -60% TiO_2 (Cl)

$\text{TiOSO}_4 \cdot 0.6\text{H}_2\text{SO}_4 \cdot 1.3\text{H}_2\text{O}$ (0.610 g, 2.55 mmol) was dissolved in 30 mL of water with 3 mL concentrated H_2SO_4 . $\text{IrCl}_3 \cdot 3\text{H}_2\text{O}$ (0.593 g, 1.68 mmol) was then added, followed by NaNO_3 (15.0 g, 176 mmol). After drying on a rotary evaporator (60 °C, 60 mbar), the solid precursor mixture was then further dried in a Muffle furnace under ambient atmosphere at 150 °C for 2 h before heating to 350 °C and staying at this temperature for 1 h. After heat treatment, the powder was washed with water (ca. 500 mL) and dried in a vacuum oven at 150 °C for 16 h.

4.5.3 Representative preparation of 40% IrO_2 -60% TiO_2 (acac)

$\text{TiOSO}_4 \cdot 0.6\text{H}_2\text{SO}_4 \cdot 1.3\text{H}_2\text{O}$ (0.307 g, 1.28 mmol) was dissolved in 15 mL of water with 1.5 mL concentrated H_2SO_4 . $\text{Ir}(\text{acac})_3$ (0.408 g, 0.828 mmol) was then added, followed by NaNO_3 (7.5 g, 88 mmol). After drying on a rotary evaporator (60 °C, 60 mbar), the solid precursor mixture was then further dried in a Muffle furnace under ambient atmosphere at 150 °C for 2 h before heating to 350 °C and staying at this temperature for 1 h. After heat treatment, the powder was washed with water (ca. 500 mL) and dried in a vacuum oven at 150 °C for 16 h.

4.5.4 Electrochemical RDE Experiments

To prepare the electrodes for the RDE experiments, 10 mg of catalyst material was mixed with water (1 mL), isopropanol (4 mL) and Nafion[®]) solution (20 μL , 5% in aliphatic alcohol and water) by sonication. The ink (10 μL) was deposited on a glassy carbon disk (5 mm diameter) substrate by drop casting. The catalyst loading was $1.02 \mu\text{g}.\text{mm}^{-2}$. The electrochemical characterisations were performed in a standard three-electrode glass cell with 1 M aqueous HClO_4 , saturated with synthetic air. All the experiments were performed at room temperature. The cyclic voltammograms were recorded with a scan rate of 50 mV.s^{-1} . The chronoamperometric measurements were performed by holding the potential for 10 s at different values in the range 1.0 - 1.4 V vs. RHE. During the measurements the RDE was rotating at 2990 rpm. The stability test consists of 500 cycles between 1 V vs. RHE to 1.6 V. The two extreme potentials were held for 10 s before continuing.

5 Oxide Supported Pt Nanoparticles: Preparation, Activity and Stability in Oxygen Reduction

5.1 Individual Contributions

All experiments and characterisation techniques were conducted by E. Oakton unless otherwise stated. Antimony-doped tin oxide was prepared and characterised by D. Lebedev. HAADF-STEM images and EDX maps were recorded by F. Krumeich using the ScopeM facilities of the ETH Zürich. Electrochemical characterisation of Pt on antimony-doped tin oxide was conducted by E. Fabbri of the Electrochemistry Laboratory at the Paul Scherrer Institute. SAXS characterisation was conducted and analysed by J. Tillier at CSEM SA. Anomalous SAXS characterisation was performed by T. Binninger, A. Hoell, X. Erler and E. Gericke at the BESSY II synchrotron at Helmholtz-Zentrum Berlin and analysed by T. Binninger. Electrochemical characterisation and oxygen reduction activity tests were conducted and analysed by T. Binninger of the Electrochemistry Laboratory at the Paul Scherrer Institute.

5.2 Introduction

Alongside new support materials, the Pt catalyst used in polymer electrolyte fuel cells (PEFCs) makes a significant contribution to the cost of this technology. Consequently there is a continuing effort to optimise the amount of Pt required to fulfill operational parameters, which focuses on increasing the activity and stability of the catalyst. Indeed the stability of the Pt catalyst is directly effected by the stability of its support. However, dissolution of Pt under cathodic conditions as well as poisoning from common stream contaminants are inherent issues, which need to be addressed.^[27,28]

Many researchers have focussed on the development of Pt alloy nanoparticles, which can improve activity and reduce poisoning rates from common stream contaminants such as carbon monoxide.^[207] Typical alloy metals include Ni, Ru and Co, with PtNi alloys showing remarkably high oxygen reduction reaction (ORR) activities.^[208] However, the poor stability of such alloys during short and long term operation, as well as the origin of instability, is still under discussion.^[209] In addition to Pt alloys, the recent interest in noble-metal free ORR catalysts cannot be ignored,^[210] although the application of carbon based materials may call their relative stabilities into question. Nevertheless, despite these efforts to reduce Pt content pure Pt nanoparticles remain the catalyst of choice for commercial PEFCs.^[27,30] Therefore there is

a focus on the preparation of pure Pt nanoparticles in the optimum size range (2 - 3 nm) to improve ORR activity.^[211]

Catalyst contaminants such as chloride ions pose an additional challenge for the improvement of PEFC technology. Chloride ions can block Pt surface sites, increasing reaction overpotentials and influencing the ORR reaction pathway.^[212] Additionally, the formation of soluble chloride species^[213] and blocking of Pt sites^[214] reduces active surface area, decreasing operational efficiency. Increased Pt dissolution rates have been observed in chloride contaminated electrolytes.^[215] Although fuel streams can be the major source of chlorine contamination, negative effects of residual Cl^- from H_2PtCl_6 decomposition have been identified.^[216] Although chloride contamination can be reduced by post-synthetic treatment, the high temperature required compromises support surface area.^[216] Therefore there is a clear need to avoid platinum chloride precursors in the preparation of Pt nanoparticles for PEFCs. Despite the well-reported negative effects of Cl^- on PEFCs, chlorinated precursors are still commonly used, primarily because of their wide availability. However there have been reports of $\text{Pt}(\text{acac})_2$,^[136,217] $\text{Pt}_2(\text{dba})_3$ ^[218] and $\text{Pt}(\text{NO}_2)_2(\text{NO}_3)_2$ ^[219] as Pt precursors for fuel cell applications.

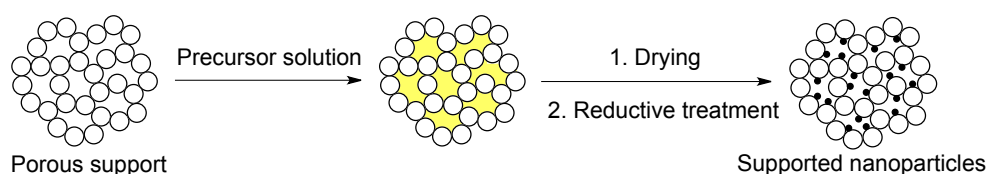
This short summary demonstrates the importance of platinum nanoparticle preparation for the development of PEFC catalyst layers. There is a need to control nanoparticle size, their distribution over the support surface and to avoid chloride contamination. Considering the continuing importance of metal oxide supports in PEFCs, this chapter discusses the preparation of metal-oxide-supported Pt nanoparticles by a variety of methods from chloride free precursors. Firstly, the impregnation of ionic precursor $\text{Pt}(\text{NH}_3)_4(\text{NO}_3)_2$ on SnO_2 supported is discussed, with considerations of support stability under treatment conditions. Colloidal Pt nanoparticle solutions are prepared from a $\text{Pt}(0)$ organometallic precursor and a variety of stabilising ligands, where influences of the preparation conditions on Pt morphology are shown. Finally a homogeneous deposition precipitation method with $\text{H}_2\text{Pt}(\text{OH})_6$ is used to deposit Pt nanoparticles on the $\text{IrO}_2\text{-TiO}_2$ supports presented in Chapter 4 and are evaluated as ORR catalysts.

5.3 Results and Discussion

5.3.1 Precursor Impregnation

Impregnation approaches to form metallic particles on porous supports are commonly found in the literature, primarily due to the ease and flexibility with which samples can be prepared.^[220,221] In short, impregnation involves the addition of a precursor solution to the support material followed by mixing, drying and a reductive gas treatment (Scheme 2). Control at

each individual step is vital for the preparation of nanoparticles with consistent morphologies and narrow size distributions.^[220] Consequently, incipient wetness impregnation (IWI) has become a popular method to control the distribution of particles across the support surface.^[220] With this method, a precursor solution is added until the pores of the support are filled and as a result, greater control of the precursor distribution on the support surface can be achieved.



Scheme 2: Precursor impregnation route to supported nanoparticles.

As discussed in Chapter 3, tin(IV) based oxides are of high interest for the development of durable catalyst supports for PEFCs. Therefore the preparation of platinum nanoparticles supported on commercial tin(IV) oxide was investigated by an impregnation route. Commercial SnO_2 was impregnated (IWI) with an aqueous solution of tetraammineplatinum(II) nitrate. In order to determine the optimum conditions for precursor reduction, H_2 temperature programmed reduction (H_2 -TPR) measurements were performed. Hydrogen temperature programmed reduction is a simple characterisation method, which can be used to determine an accurate reduction temperature for a variety of metal precursors. Additionally this characterisation technique can identify if the support of interest will reduce under similar conditions. This technique follows H_2 consumption by recording gas conductivity during thermal treatment. An increase in the thermal conductivity detector (TCD) signal correlates to the consumption of H_2 by reduction of the sample. Figure 50 displays the TCD signal recorded for the precursor supported on SiO_2 and SnO_2 , in addition to blank SnO_2 .

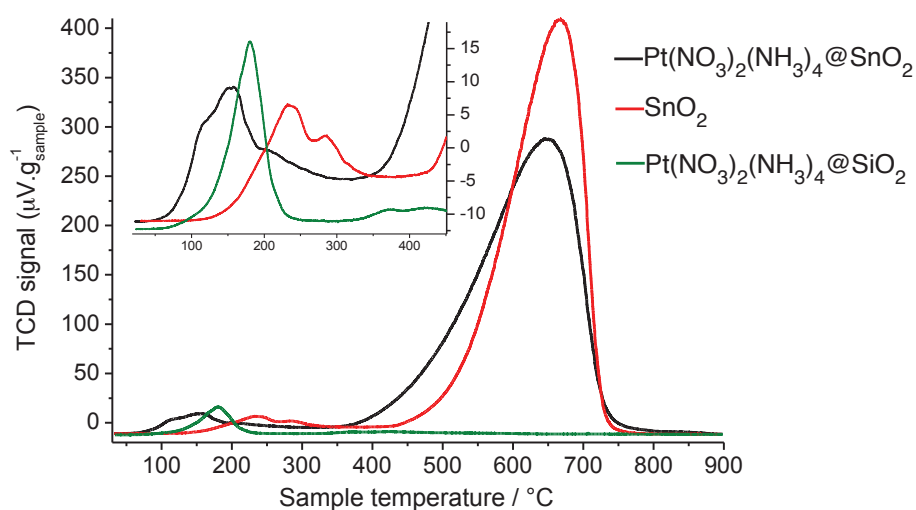


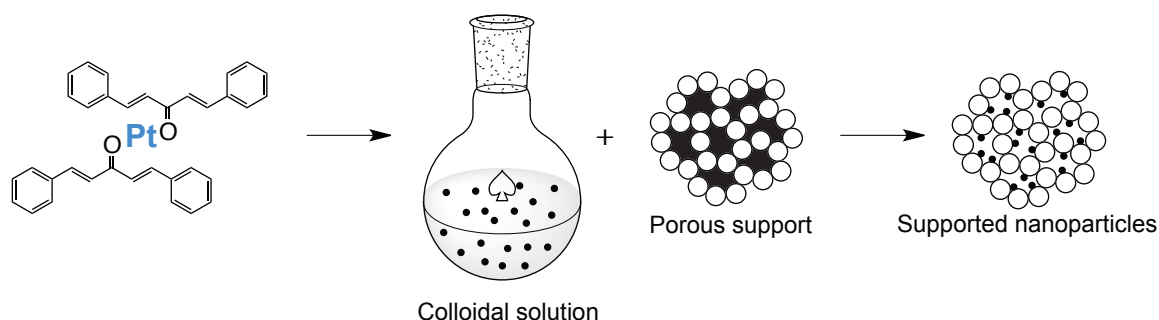
Figure 50: H₂-TPD signals for SnO₂ (red) and Pt(NH₃)₄(NO₃)₂ supported on SiO₂ (green) and SnO₂ (black).

Analysis of the signal recorded for tetraammineplatinum(II) nitrate impregnated on SiO₂ shows that the majority of precursor reduction takes place between 50 and 250 °C, with another peak visible from approximately 300 °C until 500 °C. In contrast, the blank SnO₂ support shows reduction peaks between 100 and 800 °C. Interestingly, reduction appears to start at lower temperatures for the precursor supported on SnO₂. However the inset shows the clear overlap of reduction peaks for tetraammineplatinum(II) nitrate and SnO₂, confirming that the SnO₂ support will be reduced during the H₂ treatment required for particle generation. Considering the known formation of PtSn alloys,^[222–224] the simultaneous reduction of precursor and support could potentially influence catalyst performance.^[225,226] This investigation demonstrates the non-inert nature of reducible oxides under conditions required for nanoparticle generation from impregnation methods.

5.3.2 Impregnation of Colloidal Pt Solutions

For nanoparticle preparation methods such as impregnation, the degree of size-control is dictated by a variety of variables, including the precursor, support, drying and reduction processes.^[220] Unsurprisingly, the high level of control required makes narrow size distributions difficult to achieve. On the other hand, colloidal methods have shown to yield particle solutions with extremely narrow size distributions, with the additional advantage of particle size being support independent.^[227–230] Colloidal solutions of Pt nanoparticles can be prepared from a Pt(0) precursor, such as platinum dibenzylideneacetone,^[231] and impregnated on a

porous material to yield supported nanoparticles, without the need for reductive treatment in the presence of the support (Scheme 3).



Scheme 3: Colloid impregnation approach to supported nanoparticles.

Platinum nanoparticle solutions were prepared by the decomposition of $\text{Pt}(\text{dba})_2$ ^[232] (dba = dibenzylideneacetone, shown in Scheme 3) under H_2 pressure in the presence of one equivalent of octylsilane, which acts as a stabilising agent.^[227, 231] Overnight reaction at room temperature in tetrahydrofuran (THF) solution yielded 1.3 ± 0.3 nm diameter platinum nanoparticles, shown by transmission electron microscopy (TEM) imaging, in agreement with previous reports (Figure 51a).^[231] With an aim to increase nanoparticle size to increase oxygen reduction activity,^[211] the reaction conditions were varied. Interestingly, increasing the amount of stabilising agent did not influence nanoparticle size, but reducing the amount of octylsilane to less than one equivalent led to the formation of nanowires (Figure 51b). Reaction under Ar atmosphere did not go to completion, although others have reported nanoparticle formation under these conditions.^[231] Performing the reaction in toluene yielded slightly larger nanoparticles, where evidence of nanoparticle coalescence can be observed by TEM (Figure 51c). Shortening the alkyl chain length from C_8 to C_4 , produced elongated nanowire particles (Figure 51d).

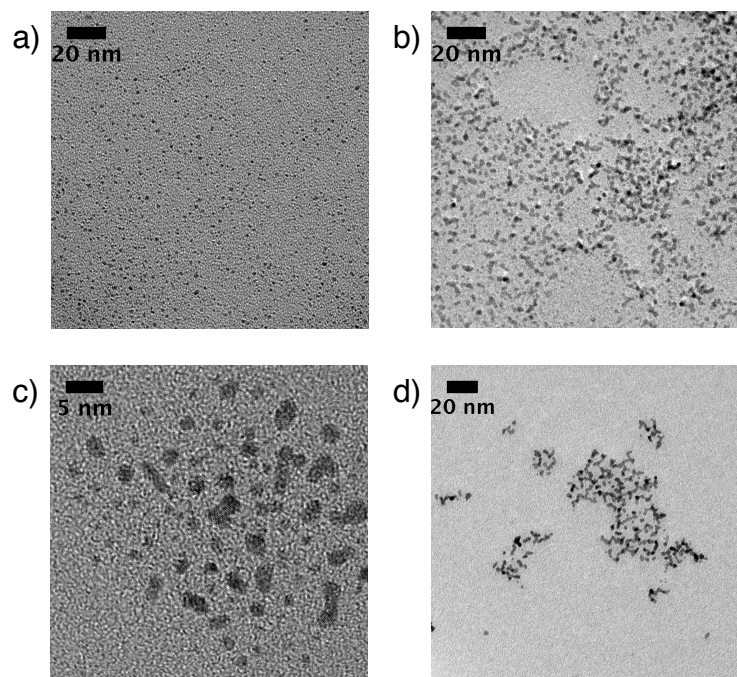


Figure 51: Bright field TEM images of Pt nanoparticle solutions prepared by the reaction of $\text{Pt}(\text{dba})_2$ under H_2 pressure with 1 equivalent of octylsilane in THF (a), 0.5 equivalents of octylsilane in THF (b), 1 equivalent of octylsilane in toluene (c) and 1 equivalent of butylsilane in THF (d).

These experiments show that varying different synthetic parameters does not lead to significant changes in particle size with silane-based stabilising ligands. This may be due to the fast formation of Pt-Si bonds, which limits further nanoparticle growth.^[231] Aiming to increase nanoparticle size to the optimum activity range for ORR (2 - 3 nm),^[211] alternative stabilising agents were investigated. Using hexadecanol as a capping agent, under identical preparation conditions, led to the formation of large particle agglomerates approximately 35 nm in diameter (Figure 52a). Reacting $\text{Pt}(\text{dba})_2$ with hexadecylamine (HDA) under H_2 pressure produced Pt nanowires, consistent with literature (Figure 52b).^[228] However, repeating the reaction under inert atmosphere at a slightly elevated temperature of 60 °C, led to the formation of 1.2 ± 0.3 nm particles (Figure 52c). The results of the different reaction conditions tested are summarised in Table 22.

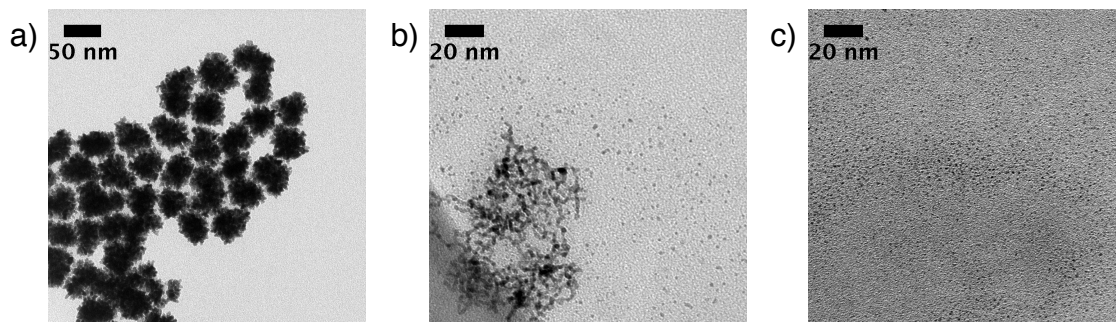


Figure 52: Bright field TEM images of nanoparticle solutions prepared hexadecanol under H_2 at 25 °C (a), hexadecylamine under H_2 at 25 °C (b) and hexadecylamine under Ar at 60 °C (c).

Table 22: Summary of Pt colloid preparation conditions

Stabilising Ligand	Atmosphere	Temperature	Pt Structure Yielded
Octylsilane	H_2	25 °C	Nanoparticles (1.3 ± 0.3 nm)
Octylsilane	Ar	25 °C	No reaction
Hexadecanol	H_2	25 °C	Large agglomerates
Hexadecanol	Ar	25 °C	No reaction
Hexadecylamine	H_2	25 °C	Nanowires
Hexadecylamine	Ar	60 °C	Nanoparticles (1.2 ± 0.3 nm)

Small Pt nanoparticles can be prepared by the reaction of $Pt(dba)_2$ and octylsilane or HDA in the presence or absence of H_2 respectively. However, in order to evaluate the electrochemical performance of these nanoparticles, they need to be impregnated on a support and treated to remove the stabilising agents to expose clean particle surfaces for catalysis. Therefore solutions of Pt nanoparticles stabilised by octylsilane (Pt-octylsilane) and HDA (Pt-HDA) were impregnated on antimony-doped tin oxide ($SnO_2:Sb$) and calcined at 400 °C to remove the stabilising ligands from the Pt surface (Figure A20). High angle annular dark field scanning transmission electron microscopy (HAADF-STEM) imaging shows that Pt-octylsilane increased in size from 1.3 to 2 - 3 nm after calcination treatment (Figure 53a). For Pt-HDA, large bright areas assigned to Pt are observed in the HAADF-STEM image indicating severe particle sintering upon removal of the stabilising ligand (Figure 53b). Considering the likely formation of Pt-Si bonds,^[231] Pt-octylsilane may remain physically stabilised against agglomeration by small SiO_2 particles/agglomerates formed during the decomposition of octylsilane.

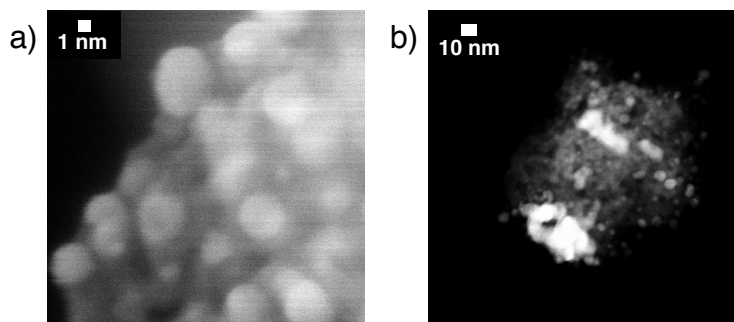


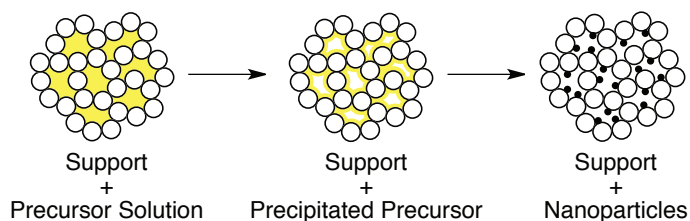
Figure 53: HAADF-STEM images of octylsilane (a) and hexadecylamine (b) stabilised Pt nanoparticles after impregnation on $\text{SnO}_2\text{:Sb}$ and calcination at 400 °C.

The reaction of $\text{Pt}(\text{dba})_2$ with octylsilane forms small Pt nanoparticles, which increase in size during calcination treatment to 2 - 3 nm, within the optimum size range for high ORR activity.^[211] Consequently efforts were made to determine the electrochemically active surface area (ECSA) of $\text{Pt}/\text{SnO}_2\text{:Sb}$ prepared from octylsilane using CO stripping,^[233] however inconsistent results were obtained indicating that CO adsorption is perturbed, perhaps by SiO_2 .

In this work, the preparation of small discrete Pt nanoparticles by stabilisation with HDA has been demonstrated. Attempts to increase nanoparticle size above 1.3 nm led to the formation of nanowire structures or large agglomerates. The impregnation of Pt-HDA and Pt-octylsilane on antimony-doped tin oxide led to the formation of large Pt agglomerates and 2 - 3 nm particles respectively. It is postulated that Pt-octylsilane particles avoid agglomeration during calcination due to the formation of SiO_2 on the particle surface, which blocks CO adsorption on the Pt surface, hindering its application in electrochemical systems. Whilst narrow size distribution Pt nanoparticles can be prepared using colloidal methods, continuing particle growth during post-impregnation treatments should be considered.

5.3.3 Homogeneous Deposition Precipitation

Homogeneous Deposition Precipitation (HDP) has shown to be an effective method for the deposition of Pt nanoparticles with narrow size distributions on carbon supports from a chlorinated Pt precursor.^[234] Furthermore, this method has the inherent advantage of being carbon-free meaning post-synthetic treatment to remove carbon based contaminants is not necessary. HDP involves the mixing of a support suspension and Pt precursor solution followed by a change in pH, which triggers the formation of precursor precipitates on the support surface, which are then reduced upon addition of a reducing agent (Scheme 4).^[234]



Scheme 4: Homogeneous Deposition Precipitation approach to supported Pt nanoparticles.

To test the flexibility of this method towards metal oxide supports, Pt nanoparticles were deposited on various metal oxides, starting from a chlorine free precursor ($\text{H}_2\text{Pt}(\text{OH})_6$). An acidic solution of $\text{H}_2\text{Pt}(\text{OH})_6$ was added to an aqueous suspension of the oxide support. After stirring, the pH was raised to pH 7 and an excess of reducing agent, NaBH_4 , was added. After overnight reaction, a black solid and colourless supernatant were separated by centrifugation. The obtained solid was dried and characterised by transmission electron microscopy. Figure 54 shows TEM images of Pt nanoparticles (10 wt%) deposited on SiO_2 and TiO_2 .

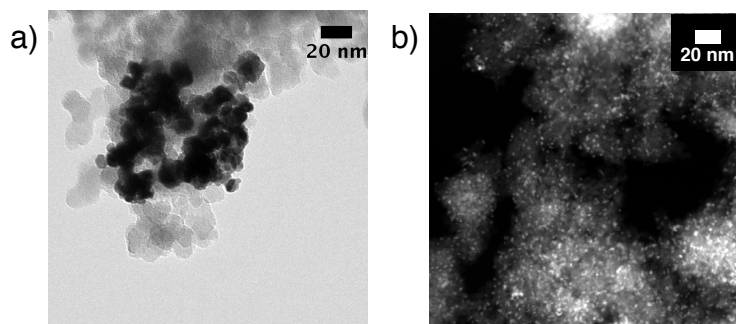


Figure 54: Bright field TEM images of Pt supported on SiO_2 (a) and HAADF-STEM image of Pt supported on TiO_2 (b).

The TEM images above show the variation of nanoparticle sizes obtained through the same deposition method on various supports. Whilst agglomerates of Pt are formed on SiO_2 , well dispersed nanoparticles are formed on TiO_2 . This demonstrates the importance of the support surface for the generation of well distributed nanoparticles. The Pt nanoparticle diameter for Pt/ TiO_2 was determined to be 2.2 ± 0.9 nm from small angle X-ray scattering (SAXS) measurements.

Considering the small Pt nanoparticles formed on pure TiO_2 are in the optimum size window for ORR activity (Figure 54),^[211] Pt nanoparticles were deposited on the chlorine free and chlorine containing IrO_2 - TiO_2 materials described in Chapter 4. It is important to note that both IrO_2 - TiO_2 materials have a nominal Ir content of 40 mol_M% and Pt content of 10

wt%. Preliminary characterisation showed no significant changes in the XRD powder diffraction pattern of either IrO₂-TiO₂ support (Figure A23, Figure A24). Direct determination of the platinum nanoparticle size from bright field TEM images for Pt/IrO₂-TiO₂ is complicated by the presence of IrO₂. Therefore energy dispersive X-ray (EDX) spectroscopy mapping was used to identify localised areas of Pt on the IrO₂-TiO₂ supports (Figure 55).

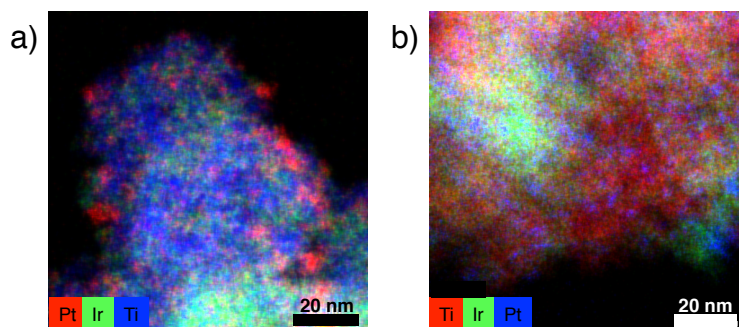


Figure 55: EDX maps of Pt nanoparticles supported on chlorine containing (a) and chlorine free (b) IrO₂-TiO₂.

Whilst the EDX maps clearly show localised areas of Pt on both supports (Figure 55), this data is insufficient to accurately determine particle size and size distribution. Therefore nanoparticle size was more accurately determined by anomalous SAXS measurements.^[235] From this characterisation technique, assuming spherical shape and log-normal size distributions, Pt nanoparticle sizes of 1.8 ± 0.5 nm and 2.8 ± 0.7 nm were determined for the chlorine-free and chlorine-containing supports respectively (Figure 56, Table 23). The larger particle size obtained for Pt/IrO₂-TiO₂(Cl), demonstrating the negative effect of chlorine contamination on nanoparticle growth. Nevertheless both samples are in the optimum size range for ORR.^[211]

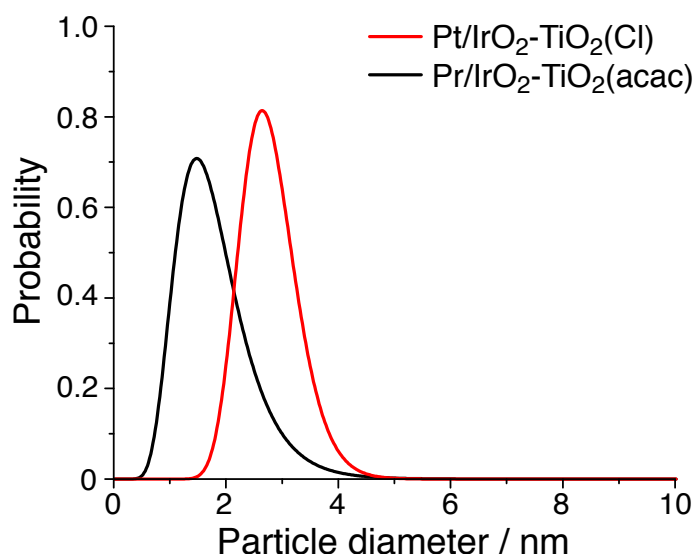


Figure 56: Particle size distribution of Pt nanoparticles supported on chlorine contaminated and chlorine free $\text{IrO}_2\text{-TiO}_2$.

Table 23: Nanoparticle sizes of Pt on $\text{IrO}_2\text{-TiO}_2$ supports

Support	Diameter / nm	Size distribution / nm
$\text{IrO}_2\text{-TiO}_2(\text{Cl})$	2.8	0.5
$\text{IrO}_2\text{-TiO}_2(\text{acac})$	1.8	0.7

This study has shown that whilst nanoparticles prepared by the HDP method vary in size according to the support nature, HDP of a chlorine free Pt precursor on TiO_2 leads to the formation of nanoparticles in the optimum size range for ORR. This method translates to $\text{IrO}_2\text{-TiO}_2$ supports, where 1.8 and 2.8 nm Pt particles were characterised by anomalous SAXS. Not only is this preparation method chloride free, it is carbon free and therefore does not require post-synthetic treatments at high temperature.

5.3.4 Electrochemical Activity and Stability of $\text{Pt/IrO}_2\text{-TiO}_2$ in the Oxygen Reduction Reaction

Pt nanoparticles with diameters within the optimum size range for the ORR reaction have been supported on chlorine-free and chlorine-containing $\text{IrO}_2\text{-TiO}_2$ materials developed in Chapter 4, denoted as $\text{Pt/IrO}_2\text{-TiO}_2(\text{acac})$ and $\text{Pt/IrO}_2\text{-TiO}_2(\text{Cl})$ respectively. Consequently,

these materials were tested under PEFC relevant conditions, investigating their activity and stability in electrochemical oxygen reduction with rotating disk electrode (RDE) experiments. The ORR activity of Pt/IrO₂-TiO₂(Cl) and Pt/IrO₂-TiO₂(acac) are compared to two commercial alternatives of platinum supported on high surface area carbon and iridium titanium oxide denoted as Pt/C and Pt/IrO₂-TiO₂(Umicore) respectively. The latter commercial sample, supplied by Umicore AG, has been studied in detail for PEFC applications, including both rotating disk electrode^[59] and membrane electrode assembly^[198] investigations. Indeed the commercial iridium titanium oxide materials, investigated here as a catalyst support, is the same as that investigated as an OER catalyst in Chapter 3 (IrO₂-TiO₂(34)). Characterisation of these commercial materials can be found in Appendix 4. It is important to note that all Pt nanoparticles are comparable in size and are in the range of 2 - 3 nm (Table A7).

A variety of electrochemical techniques were used to evaluate the suitability of the commercial and homemade supported nanoparticles as oxygen reduction catalysts. For all measurements, the catalyst powders were combined with Nafion[®], a perfluorosulfonic acid proton conducting polymer and deposited on a glassy carbon rotating disk electrode. Rotating disk electrode experiments are used to reduce mass transfer limitations by inducing a convective flow of the acidic electrolyte (0.1 M HClO₄) to the electrode surface. It is important to note that all reported potentials are with reference to the reversible hydrogen electrode (RHE).

The activity of the ORR catalysts is described by the current achieved at a set potential of 0.9 V. The amount of current generated can be reported with respect to the mass of catalyst, or the active catalyst surface area. Unlike the oxygen evolution (OER) catalysts discussed in Chapter 4, methods to determine Pt surface area are more established. The electrochemically active surface area (ECSA) can be determined from cyclic voltammetry, where potential is varied in a linear sweep. Current generated from hydrogen underpotential deposition (H_{UPD}) or the oxidation of adsorbed CO (CO stripping) can be correlated to Pt surface area. The ECSA is often thought of as a more accurate descriptor for inherent catalyst activity, as only catalyst phase with sufficient electrical connection to undergo electrochemical processes are accounted for. This is an important consideration for catalysts deposited on supports composed of conductive and non-conductive oxide mixtures. The stability of each catalyst is determined by monitoring the drop in current after potential cycling, which mimics the start-stop potential variations at the PEFC cathode, which can lead to oxidation and dissolution. Cyclic voltammetry can also be used to observe potential dependent changes in current, which may be used to rationalise the catalyst activities.

Table 25 details the ECSA per mass of platinum ($\text{m}^2.\text{g}_{\text{Pt}}^{-1}$) as well as current densities generated per active surface area ($j_{\text{ECSA}}, \mu\text{A}.\text{cm}^{-2}$) and per mass of platinum ($j_{\text{ms}}, \text{A}.\text{g}_{\text{Pt}}^{-1}$) at a potential

of 0.9 V for all investigated catalysts. The initial ECSA values for the homemade catalysts are compared to the theoretical values expected from particle size (Table 24). After recording these initial activities, the potential was cycled between 0.5 and 1.5 V to mimic start-stop potential variations, which trigger electrode degradation. The ECSA, j_{ECSA} and j_{ms} values were determined again after the degradation cycling and are reported in Table 26, percentage losses as a result of cycling are reported in parenthesis in Table 26. Pt loss during deposition is expected to be minimal due to the large excess of reducing agent used and colourless supernatant removed during centrifugation. Additionally earlier reports of comparable deposition conditions confirm nominal and final loadings to be in agreement.^[234] Furthermore, the elemental analysis of IrO₂ containing samples is problematic, due to limited dissolution options. Therefore ECSA and j_{ms} are reported with respect to nominal Pt content and consequently these values can be considered as lower limits. On the other hand, j_{ECSA} represents the current density per electrochemically active Pt surface area, determined experimentally. Methods of ECSA determination are discussed in the experimental section of this chapter.

Table 24: Comparison of theoretical ECSA value and measured value

Material	Theoretical ECSA / $\text{m}^2 \cdot \text{g}_{Pt}^{-1}$	Measured ECSA / $\text{m}^2 \cdot \text{g}_{Pt}^{-1}$
IrO ₂ -TiO ₂ (Cl)	94	95 ± 16
IrO ₂ -TiO ₂ (acac)	121	71 ± 15

Table 25: ECSA and ORR activity values before potential cycling

	ECSA / $\text{m}^2 \cdot \text{g}_{Pt}^{-1}$	j_{ECSA} / $\mu\text{A} \cdot \text{cm}^{-2}$	j_{ms} / $\text{A} \cdot \text{g}_{Pt}^{-1}$
Pt/C	63 ± 3	210 ± 20	130 ± 10
Pt/IrO ₂ -TiO ₂ (Umicore)	55 ± 7	160 ± 20	85 ± 6
Pt/IrO ₂ -TiO ₂ (Cl)	95 ± 16	29 ± 3	30 ± 7
Pt/IrO ₂ -TiO ₂ (acac)	71 ± 15	26 ± 3	18 ± 4

Table 26: ECSA and ORR activity values after potential cycling. Potential losses are reported in parenthesis

	ECSA / $\text{m}^2 \cdot \text{g}_{\text{Pt}}^{-1}$	$j_{\text{ECSA}} / \mu\text{A} \cdot \text{cm}^{-2}$	$j_{\text{ms}} / \text{A} \cdot \text{g}_{\text{Pt}}^{-1}$
Pt/C	29 \pm 1 (54)	165 \pm 20 (21)	49 \pm 6 (62)
Pt/IrO ₂ -TiO ₂ (Umicore)	34 \pm 4 (38)	130 \pm 20 (19)	44 \pm 3 (48)
Pt/IrO ₂ -TiO ₂ (Cl)	64 \pm 9 (32)	32 \pm 7 (0)	20 \pm 5 (33)
Pt/IrO ₂ -TiO ₂ (acac)	50 \pm 10 (29)	25 \pm 3 (4)	13 \pm 3 (28)

The initial ECSA values of the homemade catalysts determined by CO stripping (vide infra) are comparable to that expected from the measured Pt nanoparticle size (Table 24). The consistency between these values for Pt/IrO₂-TiO₂(Cl) suggests the Pt nominal loading is maintained. The slight decrease is observed for Pt/IrO₂-TiO₂(acac) may be explained by inaccessible Pt, which is electrically disconnected Pt nanoparticles or agglomerated.

The ECSA values of all catalysts are comparable with Pt/IrO₂-TiO₂(Cl) having a slightly larger value than the other materials (Table 25). The activity results in Tables 25 and 26 show that both Pt/IrO₂-TiO₂ catalysts have lower mass specific and ECSA specific ORR current densities in comparison to the commercial catalysts. However, the activities of Pt supported on IrO₂-TiO₂(Cl) and IrO₂-TiO₂(acac) are comparable. As expected, the Pt/C catalyst has the largest percentage loss for all parameters after the degradation cycling likely due to oxidation of the support at high potentials.^[31,32] Interestingly both homemade catalysts show lower percentage losses in comparison to the commercial Pt/IrO₂-TiO₂(Umicore).

The reduced activity of Pt/IrO₂-TiO₂(Cl) and Pt/IrO₂-TiO₂(acac) may be explained by their reduced electronic conductivity and increased amount of TiO₂ with respect to commercial IrO₂-TiO₂(Umicore) (Table A6). Despite both homemade supports having electrical conductivity values deemed sufficient for PEFC applications,^[38] the presence of TiO₂ particles may limit conduction at the nanoscale. Taking Pt/IrO₂-TiO₂(acac) as representative of both homemade materials, this hypothesis is supported by the CO oxidation curves obtained during the CO stripping experiments for ECSA determination.^[233] CO stripping involves the saturation of the Pt surface with CO, followed by potential cycling to oxidatively remove CO, producing a peak in the cyclic voltammogram. Figure 57 shows that the CO oxidation peak of the commercial IrO₂-TiO₂ material is much narrower than that of Pt/IrO₂-TiO₂(acac), indicating higher potentials are required to oxidise all adsorbed CO from Pt on the homemade support, which may be due to wider variation of Pt electrical connection.

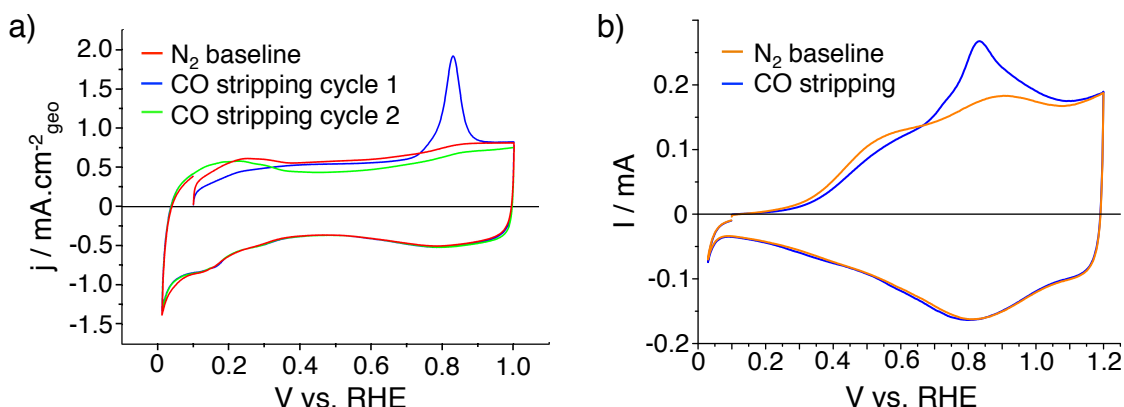


Figure 57: CO stripping experiment for Pt/IrO₂-TiO₂(Umicore) (a) and Pt/IrO₂-TiO₂(acac) (b).

Indeed CO stripping experiments have proved viable for the homemade catalysts. However, comparing the cyclic voltammograms of Pt/IrO₂-TiO₂(acac) and Pt/IrO₂-TiO₂(Umicore) (Figure 58a) reveals a reduction in the low potential current for Pt/IrO₂-TiO₂(acac), which is also observed for Pt/IrO₂-TiO₂(Cl). This region is typical for the adsorption and desorption of protons, known as hydrogen underpotential deposition (H_{UPD}) and therefore indicates that the homemade catalysts do not adsorb and desorb H^+ in the expected potential window. In contrast, peaks due to H_{UPD} are clearly visible for Pt/IrO₂-TiO₂(Umicore). The suppression of H_{UPD} for Pt/IrO₂-TiO₂(acac) is further confirmed by analysing the lower potential limit of the ORR RDE curve (Figure 58b). Increased H_2O_2 production, triggered by increased proton adsorption, under ORR conditions is known to decrease the ORR limiting current.^[212] However such limitations are not observed in the ORR RDE curve for Pt/IrO₂-TiO₂(acac), further indicating that H_{UPD} is suppressed. The contrasting adsorption of neutral and charged species on Pt/IrO₂-TiO₂(acac) indicates a shift in the electronic properties of the Pt nanoparticles when supported on the IrO₂-TiO₂ supports.

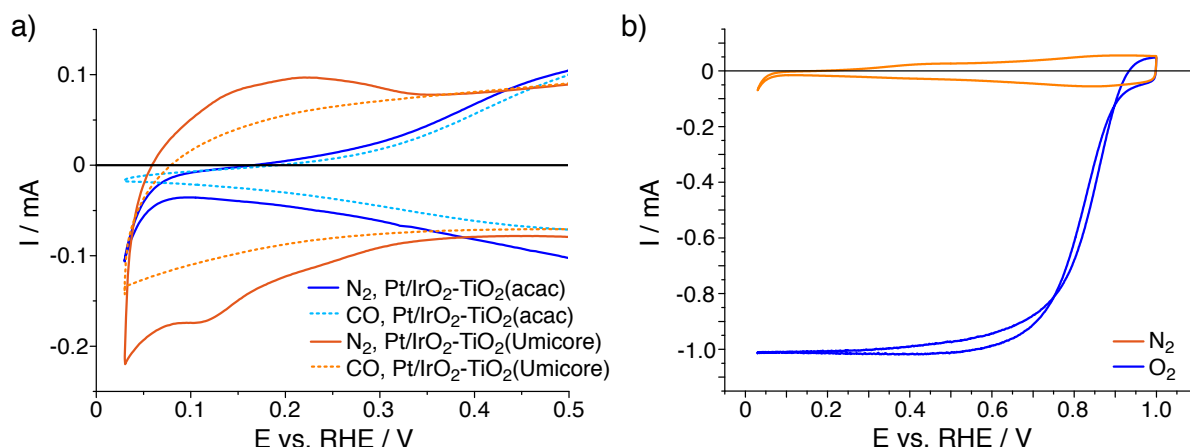


Figure 58: Cyclic voltammograms of Pt/IrO₂-TiO₂(acac) and Pt/IrO₂-TiO₂(Umicore) in N₂ and CO saturated electrolyte (a) and ORR RDE curve for Pt/IrO₂-TiO₂(acac).

Continuing from a body of work regarding iridium oxide conductivity in electrochemical systems,^[236–238] Lervik et al. note limitations in current for IrO₂ electrode films in comparison to nanoparticulate IrO₂, which is rationalised by the p-type semiconducting nature of the amorphous film electrode.^[239] However, despite notable electronic structure differences, the oxygen evolution activities were comparable.^[239] X-ray absorption spectroscopy data reported in Chapter 4 suggest that IrO₂ in IrO₂-TiO₂ has some amorphous character, which may cause variations in conductivity. However, the onset of the hydrogen evolution reaction observed for Pt/IrO₂-TiO₂(acac) by the increasing current at low potentials (Figure 58a) indicates that variations in IrO₂ conductivity may not be the only reason behind the drop in ORR activity. Interestingly, related current drops in the low potential conductivity and lack of H_{UPD} have been observed for Pt/IrO₂ and rationalised by the attenuation of Pt d-electron energies through interaction with IrO₂.^[240,241] In particular, the more facile formation of Pt-OH surface species results in lower ORR activities due to blocked O₂ adsorption sites. With this in mind the drop in ORR activity observed can be explained by the interaction between Pt and the homemade support, resulting in a shift of adsorption energies of charged species on the Pt surface and increasing formation of Pt-OH species on the homemade catalysts.

Despite the lower activity of Pt/IrO₂-TiO₂(Cl) and Pt/IrO₂-TiO₂(acac) towards ORR, these materials show lower percentage losses in comparison to the commercial catalysts, indicating improved stability. Furthermore, the mass-specific current densities (j_{ms}) obtained after potential cycling are on the same order of magnitude as the commercial alternatives. With respect to Pt/C, this improved stability can be explained by increased oxidation resistance. In comparison to Pt/IrO₂-TiO₂(Umicore), the improved stability of the homemade materials is likely due to the increased surface area of the support material (Table A6), which physically stabilises the

Pt nanoparticles against Ostwald ripening. Both homemade catalysts show comparable percentage losses, indicating that chlorine present in the catalyst support does not significantly contribute to the degradation. However the chlorine free method used to deposit Pt on IrO₂-TiO₂(Cl) and IrO₂-TiO₂(acac) may explain the improved stability due to reduced Pt dissolution in the absence of Cl.^[213]

5.4 Conclusion

Initial investigations of the precursor impregnation method, with tetraammineplatinum(II) nitrate and tin oxide, highlight the importance of support modifications during reductive treatments. A way to avoid co-reduction of the support upon nanoparticle formation, is to impregnate the support of interest with a solution of preformed, colloidal nanoparticles. Building on previous work,^[228,231] Pt nanoparticles stabilised by octylsilane and hexadecylamine were prepared and supported on antimony-doped tin oxide. After calcination treatment to remove the stabilising ligand, the octylsilane stabilised particles remained discrete whilst the amine stabilised particles agglomerate. However, the probable formation of SiO₂ in the former case limits electrochemical applications. This study shows that the choice of stabilising ligand is vital to maintaining the particle size during particle formation and post-synthetic treatments. Both these studies show that the preparation of Pt nanoparticles supported on oxide materials should involve minimal high temperature treatments, which may be required to form a metallic phase or remove organic moieties. The final investigated preparation method involves Homogeneous Deposition Precipitation, a chlorine and carbon-free route, which takes place at room temperature and does not require post-synthetic treatments. In addition to these advantageous practical aspects this method yields 1.8 and 2.8 nm Pt particles on chlorine containing and chlorine free IrO₂-TiO₂, which are within the optimum activity range for ORR.^[211]

Pt/IrO₂-TiO₂ catalysts prepared by Homogeneous Deposition Precipitation showed reduced activity but improved stability in ORR with respect two commercial catalysts. Considering literature reports, the drop in conductivity can be explained by inherent properties of IrO₂, which may display potential-dependent conductivity variations in addition to perturbing the adsorption of charged species on the Pt surface. The effect of the support on Pt oxidation state could be probed by X-ray photoelectron spectroscopy and would be an interesting subject for future work. Additionally in-situ X-ray absorption studies could confirm the presence of Pt-OH species, which may block adsorption sites. The improved stability of the homemade catalysts is rationalised by the increase in support surface area, which reduces Ostwald ripening. Furthermore, the comparable stability and activity of the chlorine containing and chlorine free homemade materials indicates that chlorine present on the catalyst support has little influ-

ence on performance. However, the chlorine-free nature of Pt nanoparticle deposition likely contributes to the improved stability due to reduced rates of Pt dissolution.

5.5 Experimental Details

5.5.1 General

All chemicals were used as received unless otherwise stated. Tetraammineplatinum(II) nitrate (99.995%), tin(V) chloride (98%) and antimony(V) chloride (> 99%) were purchased from Sigma Aldrich. Platinum dibenzylideneacetone was synthesised according to literature.^[232] Dihydrogen hexahydroxyplatinate(IV) (99.995%) was purchased from Strem Chemicals. Sodium borohydride was purchased from Merck. Ammonia solution, HCl and H₂SO₄ were purchased from Sigma Aldrich. KOH was purchased from Fisher Scientific. N-octylsilane (99.8%), n-butylsilane (95%), hexadecanol (99%) and hexadecylamine (95%) were purchased from ABCR, ABCR, Fluka-Chemie and Alfa Aesar respectively. Hydrogen (99.999%) was purchased from Pan-Gas. Distilled water was further purified using a Merck Millipore Synergy Ultrapure Water System and had a resistivity of 18.2 MΩ.cm at 25 °C upon use. Toluene was dried over an alumina column (MB SPS-800, MBraun), stored over 4 Å molecular sieves and degassed before use. THF was dried and distilled over Na and stored over 4 Å molecular sieves and degassed before use. SnO₂ (99.5%) was purchased from Alfa Aesar. SiO₂ was purchased from Aerosil Degussa and calcined at 500 °C before use. TiO₂ and IrO₂-TiO₂ supports were prepared as reported in Chapter 4. H₂-TPR measurements were performed on a Bel-cat instrument from Bel Japan Inc., with approximately 100 mg of sample. Bright field TEM imaging was performed on a Phillips CM12 microscope. HAADF-STEM images and EDX maps were recorded on a FEI Talos F200X microscope. The Small Angle X-ray Scattering (SAXS) experiments were performed with an X'Pert Pro-MPD diffractometer configured in the transmission mode. The diffractometer was equipped with the copper Kα radiation (1.541874 Å). In the incident beam path, the (1/32)° SAXS slit was placed after the parabolic mirror. The scattered intensity was measured using a PIXcel detector in the receiving slit mode using an active length of 0.165 mm which corresponds to 3 active channels.

5.5.2 Impregnation of Tetraammineplatinum(II) nitrate

An aqueous solution of Pt(NH₃)₄(NO₃)₂ (0.8 mL, 0.05 g.mL⁻¹) was added dropwise to SiO₂ (1.041 g) with stirring. The powder (1.9 wt% Pt) was dried at 120 °C under synthetic-air flow for 16 h (2 °C.min⁻¹, 100 mL.min⁻¹).

An aqueous solution of $\text{Pt}(\text{NH}_3)_4(\text{NO}_3)_2$ (0.1 mL, 0.143 g.mL^{-1}) was added dropwise to SnO_2 (1.0285 g) with stirring. The powder (0.7 wt% Pt) was dried at 120°C under synthetic-air flow for 16 h (2°C.min^{-1} , 100 mL.min^{-1}).

5.5.3 Representative Colloidal Procedure

Under Ar atmosphere, $\text{Pt}(\text{dba})_2$ (0.1051 g, 0.16 mmol) was dissolved in THF or toluene (100 mL) and transferred to a high pressure reactor under Ar. A solution of stabilising ligand was added to achieve the required equivalents per metal atom (ca. 1 mL total volume). In the case of reactions performed under H_2 , the Ar atmosphere was evacuated and replaced by H_2 (4 bar). After 16 h reaction with stirring, the H_2 atmosphere was removed and replaced by Ar.

5.5.4 Preparation of Antimony-doped Tin Oxide

The preparation of antimony-doped tin oxide was adapted from literature.^[158] SnCl_4 (10 mL, 0.098 mol) and SbCl_5 (0.57 mL, 0.0045 mol) were mixed in 30 mL of concentrated HCl. The solution was added dropwise to 500 mL of H_2O (ice bath) and after 30 min stirring 25% aqueous ammonia solution was added dropwise until pH 3.5, which caused the formation of a pale yellow precipitate. The precipitate left settle overnight, washed with H_2O and refluxed for 3 h. The volume of the obtained colloidal solution was reduced to 300 mL, and transferred into 4 autoclave reactors (125 mL) and heated at 200°C for 24 h. A blue precipitate was collected, washed with H_2O and dried at 150°C overnight in a vacuum oven. The powder was calcined at 500°C for 16 h under synthetic air-flow (2°C.min^{-1} , 100 mL.min^{-1}).

5.5.5 Colloid Impregnation

Continuing from the colloid synthesis described above. After transfer to a Schlenk flask, the solvent was evaporated until a total volume of ca. 0.5 mL was achieved. The concentrated colloid solution was impregnated on $\text{SnO}_2\text{:Sb}$, prepared as described above, to achieve 10 wt% Pt loading. After drying under ambient conditions for 16 h, the solid was calcined under synthetic-air flow at 400°C for 12 h (2°C.min^{-1} , 100 mL.min^{-1}).

5.5.6 Representative Homogeneous Deposition Precipitation Procedure

The support of interest (ca. 0.2 g) was suspended in water (100 mL) by sonication. $\text{H}_2\text{Pt}(\text{OH})_6$ (0.035 g, 1.2×10^{-4} mol) was dissolved in H_2O (3 mL) with ca. 0.5 mL H_2SO_4

and added dropwise to the support suspension under stirring. After 3 h, the pH of the solution was raised to pH 7 with 0.4 M KOH. NaBH_4 (0.0441 g, 10 equiv) was dissolved in ca. 10 mL H_2O and added dropwise to the suspension. After overnight reaction, the solid was separated by centrifugation, where the supernatant was colourless. The black solid was washed with ca. 100 mL H_2O and dried in a vacuum oven at 150 °C for 16 h.

5.5.7 Anomalous SAXS Characterisation

ASAXS analysis was used to extract the Pt scattering from the entire signal containing strong scattering from the $\text{IrO}_2\text{-TiO}_2$ support. For this purpose, SAXS curves were recorded at three different X-ray energies ($E_1 = 11553$ eV, $E_2 = 11205$ eV, $E_3 = 10998$ eV) distributed around the Pt and Ir L_{III} absorption edges ($E_{Pt,L_{III}} = 11563$ eV, $E_{Ir,L_{III}} = 11215$ eV). In this way, the energy-dependent scattering of the Ir-containing support oxide was taken into account in the analysis. Separation of the individual scattering contributions was done as described in literature.^[235] Extracted Pt particle form factors were fitted with the model of spherical particles with log-normal size distribution. A term ($B^*q^{-P} + C$) was added to the fitting function in order to take into account both an insufficient correction for support background scattering apparent at low q values and an isotropic background originating mainly from the Ir fluorescence at energy E_1 above the Ir absorption edge.

5.5.8 Electrochemical RDE Experiments

The catalyst materials were electrochemically characterized regarding their electrochemically active surface area (ECSA), their activity towards oxygen reduction reaction (ORR) and their stability during a start/stop degradation protocol. Porous thin-film electrodes were prepared from an ink consisting of 5 mg of catalyst powder, 1 mL water (Milli-Q), 4 mL Isopropanol (Sigma-Aldrich, 99.9% for HPLC) and 20 μL Nafion (Aldrich, 5 wt.-% solution). 40 μL of the ink was dropped on a glassy carbon disk (5 mm diameter), resulting in Pt loadings in the range of 20 $\mu\text{g}_{Pt}\cdot\text{cm}^{-2}$. The electrodes were tested in 0.1 M perchloric acid (prepared from Kanto Chemical Co., Inc., 60% HClO_4) inside a glass cell with three-electrode arrangement using a gold mesh counter electrode and a $\text{Hg/Hg}_2\text{SO}_4$ reference electrode, which was calibrated against a reversible hydrogen electrode (RHE). Experiments were performed with a Biologic VSP 300 potentiostat. For comparison, all experiments were also performed with an 8.8 wt% Pt/ $\text{IrO}_2\text{-TiO}_2$ (Umicore) catalyst provided by Umicore AG & Co KG (74 wt% Ir) and a commercial 47 wt% Pt/C catalyst (Tanaka TEC10E50E). Reproducibility of the results and experimental errors were established by repeating the protocol at least three times on

each material. For different catalysts, different techniques of ECSA determination had to be used: Cyclic voltammetry (CV) in N_2 -purged electrolyte was used for the commercial catalysts in order to determine the hydrogen underpotential deposition (H_{UPD}) charge ($Q_{spec} = 210 \mu\text{cm}^{-2}$). Whereas a simple background correction from the capacitive currents in the double layer region in the CV (0.4-0.5 V vs. RHE) is possible for the Pt/C Tanaka catalyst,^[233] a more sophisticated method was necessary for the Umicore catalyst using a CV recorded in CO saturated electrolyte as background correction.^[233] CO stripping voltammetry was used to determine the ECSA of the homemade catalysts: After 5 min of CO adsorption at 0.1 V vs. RHE, the electrolyte was purged with N_2 for 15 min (electrode potential kept at 0.1 V vs. RHE). Then, the potential was swept up to 1.2 V vs. RHE at 20 mVs^{-1} in order to oxidatively strip the adsorbed CO monolayer from the Pt surface. A CO stripping simulation experiment in CO-free electrolyte served as baseline for the charge integration ($Q_{spec} = 420 \mu\text{C.cm}^{-2}$).^[233] ORR activities were determined at room temperature using the thin-film rotating disk electrode (RDE) technique.^[242] Kinetic currents were extracted from the cathodic scans in the 2nd CV cycles at 5 mVs^{-1} recorded in oxygen saturated electrolyte at an electrode rotation rate of 1600 rpm. Potentials were corrected for Ohmic IR-drops (measured by high frequency impedance). For all Pt/IrO₂-TiO₂ catalysts, a correction for the comparably large CV currents (at 5 mVs^{-1}) in oxygen free electrolyte was necessary. Finally, the ORR currents were corrected for mass transport losses using the Koutecky-Levich equation. The resulting kinetic currents were taken at 0.9 V vs. RHE for comparison of the different catalyst materials. The bare support materials showed no relevant activity for ORR at potentials above 0.5 V vs. RHE. Cathode catalyst degradation during polymer electrolyte fuel cell (PEFC) operation was assessed by simulating PEFC start/stop conditions in the glass cell set-up using 1000 potential cycles between 0.5 V vs. RHE and 1.5 V vs. RHE in N_2 purged electrolyte.^[243–245]

6 Conclusion and Outlook

Metal oxides have been proposed as durable catalyst supports for polymer electrolyte fuel cells (PEFCs) as they exhibit good corrosion stability in an acidic environment and can be easily prepared with high surface areas and porosities. However, increasing metal oxide conductivity to a value sufficient for PEFCs (0.1 S.cm^{-1}) remains a limitation for these materials. Therefore this work has focused on the preparation of high surface area conductive oxides, using different methods to increase oxide conductivity, namely oxygen defects, doping and the use of intrinsically conductive oxides.

High surface area tungsten oxides have been prepared using non-hydrolytic sol-gel chemistry. Exploring the reaction of different tungsten precursors showed that different particle shapes are formed, with WCl_6 and $\text{WCl}_4(\text{DME})$ yielding cube and rod-shape particles respectively. The precursor oxidation state appears to influence the oxide phase, with a substoichiometric oxide formed from $\text{WCl}_4(\text{DME})$. Electron paramagnetic resonance (EPR) spectroscopy confirmed the oxygen deficiency of both oxides, with the identification of W(V) species. These oxides have higher electrical conductivities than commercial WO_3 , which could be further improved by treatment under nitrogen flow at 500°C . Although the highest electrical conductivities achieved here are lower than the proposed minimal requirement for PEFCs (0.04 vs. 0.1 S.cm^{-1}), conductivity has been significantly improved in comparison to commercial WO_3 (0.04 vs. $4.5 \times 10^{-7} \text{ S.cm}^{-1}$), demonstrating the influence of oxygen defects on oxide electrical properties. To understand the stability of oxygen deficient materials under PEFC relevant conditions, the electrochemical stability of oxygen deficient tungsten oxide (WO_x) was investigated using rotating disk electrode experiments. Cyclic voltammetry and X-ray photoelectron spectroscopy (XPS) indicated that WO_x was oxidised during potential cycling between 0 and 1 V as well as 0.5 and 1.5 V . Oxidation of WO_x would be expected to decrease its conductivity, which would have huge impacts on operation efficiency in a real PEFC system. This demonstrates that whilst oxygen defects may significantly improve oxide conductivity, the resulting materials do not have sufficient stability in electrochemical systems.

Doped tin oxide supports were developed to investigate the effect of doping on oxide conductivity. Niobium-doped tin oxide ($\text{SnO}_2\text{:Nb}$) was thus prepared by an aqueous coprecipitation method, where a nominal Nb loading of $5 \text{ mol}_M\%$ and calcination at 500°C were found to be the optimum conditions to provide $\text{SnO}_2\text{:Nb}$ with the highest electrical conductivity. Interestingly, antimony-doped tin oxide ($\text{SnO}_2\text{:Sb}$) prepared under identical conditions had a much larger electrical conductivity (0.02 vs. $10^{-5} \text{ S.cm}^{-1}$). X-ray diffraction (XRD) and elemental mapping by energy dispersive X-ray (EDX) spectroscopy suggest these materials have

comparable oxide structures and dopant distributions. Monitoring the crystallisation process by variable temperature XRD showed however, that the crystallite growth rates of SnO_2 and $\text{SnO}_2\text{:Sb}$ are near identical, whilst the growth of $\text{SnO}_2\text{:Nb}$ is limited and reaches only half the value of SnO_2 and $\text{SnO}_2\text{:Sb}$. This limited crystallite growth is an indication of dopant segregation. The presence of a segregated niobium oxide phase was further investigated by X-ray absorption spectroscopy (XAS) at the Nb K-edge, where Nb centers in a tetrahedral geometry were identified, which is consistent with commercial and homemade Nb_2O_5 . Interestingly, line broadening of the Sn(VI) signal in the ^{119}Sn nuclear magnetic resonance (NMR) spectrum of calcined $\text{SnO}_2\text{:Nb}$ in comparison to that of SnO_2 was observed, which indicates that Nb does influence the host SnO_2 lattice after calcination and is at least partially present in the SnO_2 lattice. Through this combination of characterisation techniques, the partial segregation of Nb in $\text{SnO}_2\text{:Nb}$ has been revealed and this effective reduction in dopant content is consistent with the lower electrical conductivity of this material. As part of this work, high surface area antimony-doped tin oxide has been prepared with relatively low dopant content. Considering that reducing dopant content has been suggested as a way to improve the stability of antimony-doped tin oxides,^[48] electrochemical characterisation of this material would be of high interest in this field and an interesting subject for future work. Furthermore, the range of techniques used here, to characterise antimony and niobium-doped tin oxides, provides a benchmark for the effective characterisation of such materials. This improved structural understanding will aid the development of the structure-property relationships for doped materials, which have a wide variety of applications.

Another approach to generate conductive oxide supports, with minimal cost, is to combine an expensive but highly conductive oxide, such as iridium oxide with a cheaper oxide but less conductive oxide like titanium oxide. This approach has been investigated in literature, to yield materials with applications as PEFC catalyst supports and oxygen evolution catalysts, however reducing iridium content remains of high interest. Towards this goal, iridium titanium oxide materials ($\text{IrO}_2\text{-TiO}_2$) were prepared by a one-pot reaction with sodium nitrate (Adams method). TEM revealed these high surface area materials are composed of TiO_2 and IrO_2 particles with 5 and 1 nm diameters respectively. Furthermore, IrO_2 particle size is independent of composition. Interestingly, XRD showed that the presence of Ir influences the phase of TiO_2 formed. An iridium content of 40 mol_M% yields a material with sufficient electrical conductivity for PEFC applications (0.46 S.cm^{-1}). Extending the preparation method to $\text{IrO}_2\text{-MO}_x$ materials, where $M = \text{Sn}$ or Nb , yielded oxides with similar morphologies, but reduced electrical conductivities in comparison to $\text{IrO}_2\text{-TiO}_2$. This demonstrates that the co-oxide used in combination with IrO_2 also influences electrical conductivity. Moreover, changing the iridium precursor from iridium chloride to iridium acetylacetonate provided chlorine-free $\text{IrO}_2\text{-TiO}_2$

with similar morphology and conductivity, further demonstrating the inherent nature of this preparation method to produce small IrO₂ particles. Interestingly the IrO₂-TiO₂ materials described above have significantly larger surface areas than a commercial alternative provided by Umicore AG (250 vs. 34 m².g⁻¹). Moreover, the composition with sufficient conductivity for PEFCs has a reduced Ir content in comparison to the same commercial alternative (40 vs. 70 mol_M% or 55 vs. 74 wt% Ir).

Towards the generation of improved PEFCs, chlorine-containing and chlorine-free IrO₂-TiO₂ were evaluated as catalyst supports in PEFCs. For this purpose a chlorine-free homogeneous deposition precipitation route was used to deposit Pt nanoparticles on these supports and the resulting materials evaluated as oxygen reduction (ORR) electrocatalysts. The similar activities and stabilities of the chlorine-containing and chlorine-free homemade supports indicate that chlorine contamination of the support does not influence these parameters. The homemade catalysts have lower activities but improved stabilities with respect to two commercial alternatives. Interestingly, cyclic voltammetry of the homemade catalysts shows an absence of hydrogen underpotential deposition, which indicates a shift in the adsorption properties on the Pt surface. This observation could be explained by potential dependent changes in IrO₂ conductivity and/or Pt-IrO₂ interactions perturbing Pt d-electron energies. Changes in the adsorption energies of reactants, intermediates and products of ORR on the Pt surface could also explain the reduced activities of the homemade catalysts. After potential cycling between 0.5 and 1.5 V, the oxide based catalysts show better stability in comparison to commercial Pt/C. Furthermore the homemade catalysts show marginally improved stability with respect to commercial Pt/IrO₂-TiO₂ provided by Umicore AG & Co. This enhanced stability is attributed to the increased surface area of homemade IrO₂-TiO₂ and the chlorine-free nature of Pt deposition.

Iridium oxide is of high interest for PEFC catalyst support applications due to its high conductivity and stability. The influence of M on the electrical conductivity of IrO₂-MO_x has been shown and would be an interesting subject for further investigation. The high stability of platinum nanoparticles supported IrO₂-TiO₂ prepared by Adams method has been demonstrated, although their lower oxygen reduction activity in comparison to commercial alternatives is indeed a disadvantage. Support composition may play a role in determining conductivity at the nanoscale, for which the investigation of varying IrO₂-TiO₂ compositions would be important to fully evaluate the PEFC suitability of such materials. The amorphous nature of IrO₂ could also influence the oxygen reduction activity and therefore alternative IrO₂-TiO₂ preparation routes to increase the crystallinity of IrO₂ would be of interest. The improved stability of Pt/IrO₂-TiO₂ could also be as a result of the chlorine-free Pt nanoparticle deposition method. Comparing commercial and homemade Pt/support catalysts would confirm or disprove this hypothesis.

Combining PEFCs with water splitting technology would provide the fuels cells with pure H_2 and O_2 , the latter of which is expected to positively impact cell efficiency. Interestingly, in addition to their potential application as PEFC catalyst supports, tungsten oxide and iridium oxide are also known to be active catalysts for oxygen evolution. Consequently the tungsten oxides and iridium titanium oxide materials described above were also investigated as photocatalytic and electrocatalytic oxygen evolution catalysts respectively.

The activity and stability of blue tungsten oxides prepared by non-hydrolytic sol-gel were investigated in photocatalytic oxygen evolution under UV irradiation. All homemade tungsten oxides showed lower oxygen evolution activities in comparison to commercial WO_3 , which was rationalised by the presence of oxygen defects and small particle sizes, which enhance electron-hole recombination. Although particle shape did not appear to influence activity, an increase in oxygen evolution activity observed after nitrogen treatment was attributed to increased particle size. Nitrogen treatment also caused a phase change from tetragonal to monoclinic for WO_x prepared from WCl_6 , which explains its further activity enhancement after post-synthetic treatment. This study has demonstrated the importance of oxygen deficiency, particle size and phase for tungsten oxide based photocatalysts and can be used to develop more active oxygen evolution photocatalysts. Despite their lower activities, the nitrogen treated tungsten oxides showed improved stability with respect to commercial WO_3 . The origin of this improved stability remains an open question, however characterisation after photocatalysis would provide more information regarding catalyst deactivation.

Chlorine-free iridium titanium oxides prepared from iridium acetylacetonate (70 and 40 mol_M% Ir) were investigated as oxygen evolution electrocatalysts. Taking the potential required to achieve a current of 10 A.g_{Ir}^{-1} as an activity descriptor, these catalysts showed improved activity in comparison to commercial IrO_2 and $IrO_2\text{-TiO}_2$. Characterisation of the dry catalysts by XAS at the Ir L_{III} -edge showed that this improved activity is correlated to the amorphous nature of IrO_2 prepared by reaction with sodium nitrate at 350 °C. Although pure IrO_2 prepared by at the same temperature has a comparable activity, the application of $IrO_2\text{-TiO}_2$ has the additional advantage of reducing IrO_2 content, which would have a significant impact on cost and consequently commercial viability of water electrolyzers. Interestingly, the 40 mol_M% Ir catalyst has a comparable stability to pure IrO_2 , but $IrO_2\text{-TiO}_2$ with 70 mol_M% Ir is much less stable. These stability studies would benefit from repeat measurements and electrode characterisation after stability tests to determine the origin of catalyst deactivation. The investigation of $IrO_2\text{-TiO}_2$ in membrane electrode assemblies (MEAs) is an important next step for the full evaluation of $IrO_2\text{-TiO}_2$ as an oxygen evolution catalyst for proton exchange membrane water electrolyzers (PEMWEs).

Alongside the PEFC and PEMWE applications discussed as part of this work, iridium titanium oxide has applications in photocatalytic oxygen evolution through water oxidation and total water splitting in the presence of Pt.^[246] Considering the mixtures of small TiO₂ and IrO₂ particles yielded from the Adams method, the investigation of these materials as oxygen evolution photocatalysts could make a contribution to this field. Furthermore, the combination of Pt nanoparticles with IrO₂-TiO₂, discussed as part of this work, could contribute to the development of catalysts capable of total water splitting.

References

- [1] Chew, K. J. *Philos. Trans. R. Soc. A* **2014**, 372.
- [2] Arico, A. S.; Bruce, P.; Scrosati, B.; Tarascon, J. M.; Schalkwijk, W. V. *Nature Materials* **2005**, 4, 366–377.
- [3] Haldane, J. B. S., *Daedalus, or Science and the Future*; Kegan Paul, Trench, Trubner & Co., Ltd., 1923.
- [4] Jones, L. W. *Science* **1971**, 174, 367–370.
- [5] Bockris, J. O. *Science* **1972**, 176, 1323.
- [6] Williams, L. O., *Hydrogen Power: An Introduction into Hydrogen Energy and Its Applications*; Elsevier Ltd., 1980.
- [7] Osterloh, F. E. *Chem. Mater.* **2008**, 20, 35–54.
- [8] Kudo, A.; Miseki, Y. *Chem. Soc. Rev.* **2009**, 38, 253–278.
- [9] Chen, X.; Shen, S.; Guo, L.; Mao, S. S. *Chem. Rev.* **2010**, 110, 6503–6570.
- [10] Osterloh, F. E. *Chem. Soc. Rev.* **2013**, 42, 2294–2320.
- [11] Jaramillo, T. F.; Jørgensen, K. P.; Bonde, J.; Nielsen, J. H.; Horch, S.; Chorkendorff, I. *Science* **2007**, 100–102.
- [12] Li, Y.; Wang, H.; Xie, L.; Liang, Y.; Jong, G.; Dai, H. *J. Am. Chem. Soc.* **2011**, 133, 7296–7299.
- [13] Voiry, D.; Yamaguchi, H.; Li, J.; Silva, R.; Alves, D. C. B.; Fujita, T.; Chen, M.; Asefa, V. B. T. and Shenoy; Eda, G.; Chhowalla, M. *Nature Materials* **2013**, 12, 850–855.
- [14] Chen, G.; Delafuente, D. A.; Sarangapani, S.; Mallouk, E. *Catal. Today* **2001**, 67, 341–355.

- [15] Shaprio, D.; Duffy, J.; Kimble, M.; Pien, M. *Solar Energy* **2005**, *79*, 544–550.
- [16] Pettersson, J.; Ramsey, B.; Harrison, D. *J. Power Sources* **2006**, *157*, 28–34.
- [17] Holladay, J. D.; Hu, J.; King, D. L.; Wang, Y. *Catal. Today* **2009**, *139*, 244–260.
- [18] Armandi, M.; Drago, D.; Pagani, M.; Bonelli, B.; Santrarelli, M. *Int. J. Hydrogen Energy* **2012**, *37*, 1292–1300.
- [19] D'Alessandro, D. M.; Smit, B.; Long, J. R. *Angew. Chem. Int. Ed.* **2010**, *49*, 6058–6082.
- [20] Carrette, L.; Friedrich, K. A.; Stimming, U. *ChemPhysChem* **2000**, *1*, 162–193.
- [21] White, C. M.; Steeper, R. R.; Lutz, A. E. *Int. J. Hydrogen Energy* **2006**, *31*, 1292–1305.
- [22] Das, L. M. *Int. J. Hydrogen Energy* **1990**, *15*, 425–443.
- [23] Verhelst, S. *Int. J. Hydrogen Energy* **2014**, *39*, 1071–1085.
- [24] Barnett, B. M.; Teagan, W. P. *J. Power Sources* **1992**, *37*, 15–31.
- [25] Mekhilef, S.; Saidur, R.; Safari, A. *Renewable Sustainable Energy Rev.* **2012**, *16*, 981–989.
- [26] Wang, Y.; Chen, K. S.; Mishler, J.; Cho, S. C.; Adroher, X. C. *Appl. Energy* **2011**, *88*, 981–1007.
- [27] Borup, R.; Meyers, J.; Pivovar, B.; Kim, Y. S.; Mukundan, R.; Garland, N.; Myers, D.; Wilson, M.; Garzon, F.; Wood, D.; Zelenay, P.; More, K.; Stroh, K.; Zawodzinski, T.; Boncella, J.; McGrath, J. E.; Inaba, M.; Miyatake, K.; Hori, M.; Ota, K.; Ogumi, Z.; Miyata, S.; Nishikata, A.; Siroma, Z.; Uchimoto, Y.; Yasuda, K.; Kimijima, K.-I.; Iwashita, N. *Chem. Rev.* **2007**, *107*, 3904–3951.
- [28] Wu, J.; Yuan, X. Z.; Martin, J. J.; Wang, H.; Zhang, J.; Shen, J.; Wu, S.; Werida, W. *J. Power Sources* **2008**, *184*, 104–119.
- [29] Brett, D. J. L.; Kucernak, A. R.; Aguiar, P.; Atkins, S. C.; Brandon, N. P.; Clague, R.; Cohen, L. F.; Kinds, G.; Kalyvas, C.; Offer, G. J.; Ladewig, B.; Maher, R.; Marquis, A.; Shearing, P.; Vasileiadis, N.; Vesovic, V. *ChemPhysChem* **2010**, *11*, 2714–2731.
- [30] Gottesfeld, S.; Zawodzinski, T. A., *Polymer Electrolyte Fuel Cells in Advances in Electrochemical Science and Engineering*; Wiley-VCH Verlag GmbH, 1997.
- [31] Kinoshita, K., *Electrochemical and Physicochemical Properties*; John Wiley & Sons, 1988.

- [32] Linse, N.; Gubler, L.; Scherer, G. G.; Wokaun, A. *Electrochim. Acta* **2011**, *56*, 7541–7549.
- [33] Kangasniemi, K. H.; Condit, D. A.; Jarvi, T. D. *J. Electrochem. Soc.* **2008**, *151*, E125–E132.
- [34] Linse, N.; Scherer, G. G.; Wokaun, A.; Gubler, L.; In *The ASME 8th International Conference on Fuel Cell Science, Engineering and Technology*, Vol. 2, pages 357–362, 2010.
- [35] Zhang, S.; Yuan, X. Z.; Hing, J. N. C.; Wang, H.; Friedrich, K. A.; Schulze, M. *J. Power Sources* **2009**, *194*, 588–600.
- [36] Roen, L. M.; Paik, C. H.; Jarvi, T. D. *Electrochem. Solid-State Lett.* **2004**, *7*, A19–A22.
- [37] Schulenburg, H.; Schwanitz, B.; Linse, N.; Scherer, G. G.; Wokaun, A.; Krbanjevic, J.; Grothausmann, R.; Manke, I. *J. Phys. Chem. C* **2011**, *115*, 14236–14243.
- [38] Rabis, A.; Rodriguez, P.; Schmidt, T. J. *ACS Catal.* **2012**, *2*, 864–890.
- [39] Sasaki, K.; Takasaki, F.; Noda, Z.; Hayashi, S.; Shiratori, Y.; Ito, K. *ECS Trans.* **2010**, *33*, 473–482.
- [40] Hench, L. L.; West, J. K. *Chem. Rev.* **1990**, *90*, 33–72.
- [41] Yang, P. D.; Zhai, D. Y.; Margolese, D. I.; Chmelka, B. F.; Stucky, G. D. *Nature* **1998**, *396*, 152–155.
- [42] Niederberger, M. *Acc. Chem. Res.* **2007**, *40*, 793–800.
- [43] Mutin, P. H.; Vioux, A. *Chem. Mater.* **2009**, *21*, 582–596.
- [44] Wang, D. L.; Subban, C. V.; Wang, H. S.; Rus, E.; DiSalvo, F. J.; Abruna, H. D. *J. Am. Chem. Soc.* **2010**, *132*, 10218–10220.
- [45] Chhina, H.; Campbell, S.; Kesler, O. *J. Electrochem. Soc.* **2007**, *154*, B533–B539.
- [46] Masao, A.; Noda, S.; Takasaki, F.; Ito, K.; Sasaki, K. *Electrochem. Solid-State Lett.* **2009**, *12*, B119–B122.
- [47] Elezovic, N. R.; Babic, B. M.; Radmilovic, V. R.; Krstajic, N. V. *J. Electrochem. Soc.* **2013**, *160*, F1151–F1158.
- [48] Fabbri, E.; Rabis, A.; Kötz, R.; Schmidt, T. J. *Phys. Chem. Chem. Phys.* **2014**, *16*, 13672–13681.

- [49] Orilall, M. C.; Matsumoto, F.; Zhou, Q.; Sai, H.; Abruna, H. D.; DiSalvo, F. J.; Wiesner, U. *J. Am. Chem. Soc.* **2009**, *131*, 9389–9395.
- [50] Zhang, L.; Wang, L. Y.; Holt, C. M. B.; Navessin, T.; Malek, K.; Eikerling, M. H.; Mitlin, D. *J. Phys. Chem. C* **2010**, *114*, 16463–16474.
- [51] Bonakdarpour, A.; Tucker, R. T.; Fleischauer, M. D.; Beckers, N. A.; Brett, M. J.; Wilkinson, D. P. *Electrochim. Acta* **2012**, *85*, 492–500.
- [52] Kraemer, S. v.; Wikander, J.; Lindbergh, G.; Lundblad, A.; Palmqvist, A. E. C. *J. Power Sources* **2008**, *180*, 185–190.
- [53] Gojkovic, S. L.; Babic, B. M.; Radmilovic, V. R.; Krstajic, N. V. *J. Electroanal. Chem.* **2010**, *639*, 161–166.
- [54] Wu, G.; Nelson, M. A.; Mack, N. H.; Ma, S. G.; Sekhar, P.; Garzon, F. H.; Zelenay, P. *Chem. Commun.* **2010**, *46*, 7489–7491.
- [55] Christian, J. B.; Smith, S. P. E.; Whittingham, M. S.; Abruna, H. D. *Electrochem. Commun.* **2007**, *9*, 2128–2132.
- [56] Yin, M.; Xu, J. Y.; Li, Q. F.; Jensen, J. O.; Huang, Y. J.; Cleeman, L. N.; Bjerrum, N. J.; Xing, W. *Appl. Catal. B* **2014**, *144*, 112–120.
- [57] Jiang, Z.; Wang, Z.; Chu, Y.; Gu, D.; Yin, G. *Energy Environ. Sci.* **2011**, *4*, 728–735.
- [58] Suchsland, J. P.; Klose-Schubert, B.; Herein, D.; Martin, T.; Eickes, C.; Lennartz, M. *ECS Trans.* **2012**, *50*, 1659–1667.
- [59] Binninger, T.; Fabbri, E.; Kötz, R.; Schmidt, T. J. *ECS Trans.* **2013**, *58*, 1835–1841.
- [60] Lewera, A.; Timperman, L.; Roguska, A.; N., A.-V. *J. Phys. Chem. C* **2011**, *115*, 20153–20159.
- [61] Zhang, Z.; Liu, J.; J., G.; Su, L.; Cheng, L. *Energy Environ. Sci.* **2014**, *7*, 2535–2558.
- [62] Luo, Y.; Alanso-Vante, N. *Electrochim. Acta* **2015**, *179*, 108–118.
- [63] Kakinuma, K.; Uchida, M.; Kamino, T.; Uchida, H.; Watanabe, M. *Electrochim. Acta* **2011**, *56*, 2881–2887.
- [64] Tauster, S. J.; Fung, S. C. *J. Catal.* **1978**, *55*, 29–35.
- [65] Dunn, S. *Int. J. Hydrogen Energy* **2002**, *27*, 235–264.

- [66] Smith, W. J. *Power Sources* **2000**, 86, 74–83.
- [67] Ioroi, T.; Kitazawa, N.; Yasuda, K.; Yamamoto, Y.; Takenaka, H. *J. Appl. Electrochem.* **2001**, 31, 1179–1183.
- [68] Büchi, F. N.; Hofer, M.; Peter, C.; Cabalzar, U. D.; Bernard, J.; Hannesen, U.; Schmidt, T. J.; Closset, A.; Dietrich, P. *RSC Adv.* **2014**, 4, 56139–56146.
- [69] Pan, H.; Zhu, S.; Lou, X.; Mao, L.; Lin, J.; Tian, F.; Zhang, D. *RSC Adv.* **2015**, 5, 6543–6552.
- [70] Frydendal, R.; Busch, M.; Halck, N. B.; Paoli, E. A.; Krtil, P.; Chorkendorff, I.; Rossmeisl, J. *ChemCatChem* **2015**, 7, 149–154.
- [71] Trasatti, S. *J. Electroanal. Chem.* **1980**, 111, 125–131.
- [72] Lee, Y.; Suntivich, J.; May, K. J.; Perry, E. E.; Shao-Horn, Y. *J. Phys. Chem. Lett.* **2012**, 3, 399–404.
- [73] Mazur, P.; Polonsky, J.; Paidar, M.; Bouzek, K. *Int. J. Hydrogen Energy* **2012**, 37, 12081–12088.
- [74] Song, J.; Huang, Z.-F.; Pan, L.; Zhang, X.; Wang, L. *ACS Catal.* **2015**, 5, 6594–6599.
- [75] Gillet, M.; Lemire, C.; Gillet, E.; Aguir, K. *Surf. Sci.* **2003**, 532, 519–525.
- [76] Granqvist, C. G. *Appl. Phys. A: Solid Surf.* **1993**, 57, 3–12.
- [77] Eranna, G.; Joshi, B. C.; Runthala, D. P.; Gupta, R. P. *Crit. Rev. Solid State* **2004**, 29, 111–118.
- [78] Berger, O.; Hoffmann, T.; Fischer, W.-J. *J. Mater. Sci-Mater. El.* **2004**, 15, 483–493.
- [79] Polleux, J.; Gurlo, A.; Barsan, N.; Wiemar, U.; Antonietti, M.; Niederberger, M. *Angew. Chem. Int. Ed.* **2006**, 45, 261–265.
- [80] Cheng, W.; Baudrin, E.; Dunn, B.; Zink, J. I. *J. Mater. Chem.* **2001**, 11, 92–97.
- [81] Liang, L.; Zhang, J.; Zhou, Y.; Xie, J.; Zhang, X.; Guan, M.; Pan, B.; Xie, Y. *Scientific Reports* **2013**, 3, 1936.
- [82] Abe, R.; Takami, H.; Murakami, N.; Ohtani, B. *J. Am. Chem. Soc.* **2008**, 130, 7780–7781.
- [83] Ma, S. S. K.; Maeda, K.; Abe, R.; Domen, K. *Energy Environ. Sci.* **2012**, 5, 8390–8397.

- [84] Shao, Y.; Liu, Y. J. Wang; Lin, Y. J. *Mater. Chem.* **2009**, *19*, 46–59.
- [85] Nakajima, H.; Honma, I. *Solid State Ionics* **2002**, *148*, 607–610.
- [86] Li, Y.-M.; Hibino, M.; Miyayania, M.; Kudo, T. *Solid State Ionics* **2000**, *134*, 271–279.
- [87] Inaba, M.; Yamada, H.; Tokunaga, J.; Matsuzawa, K.; Hatanaka, A.; Tasaka, A. *ECS Trans.* **2006**, *8*, 315–322.
- [88] Kulesza, P. J.; Miecznikowski, K.; Baranowska, B.; Skunik, M.; Fiechter, S.; Bogdanoff, P.; Dorbandt, I. *Electrochem. Commun.* **2006**, *8*, 904–908.
- [89] Zhu, T.; Chong, M. N.; Chan, E. S. *ChemSusChem* **2014**, *7*, 2974–2997.
- [90] Amano, F.; Ishinaga, E.; Yamakata, A. *J. Phys. Chem. C* **2013**, *117*, 22584–22590.
- [91] Bamwenda, G. R.; Arakawa, H. *Appl. Catal. A-Gen.* **2001**, *210*, 181–191.
- [92] Liu, G.; Han, J.; Zhou, X.; Huang, L.; Zhang, F.; Wang, X.; Ding, C.; Zheng, X.; Han, H.; Li, C. *J. Catal.* **2013**, *307*, 148–152.
- [93] Zhao, Z.-G.; Miyauchi, M. *Angew. Chem. Int. Ed.* **2008**, *47*, 7051–7055.
- [94] Wang, J.; Wang, Z.; Huang, B.; Ma, Y.; Liu, Y.; Qin, X.; Zhang, X.; Dai, Y. *ACS Appl. Mater. Interfaces* **2012**, *4*, 4024–4030.
- [95] Ansari, S. A.; Khan, M. M.; Kalathil, S.; Nisar, A.; Lee, J.; Cho, M. H. *Nanoscale* **2013**, *5*, 9238–9246.
- [96] Aminian, M. K.; Ye, J. *J. Mater. Res.* **2010**, *25*, 141–148.
- [97] Kato, H.; Asakura, K.; Kudo, A. *J. Am. Chem. Soc.* **2003**, *125*, 3082–3089.
- [98] Balazs, N.; Mogyerosi, K.; Sranke, D. F.; Pallagi, A.; Alapi, T.; Oszko, A.; Dombi, A.; Sipos, P. *Appl. Catal. B-Environ.* **2008**, *84*, 356–362.
- [99] Zheng, H.; Ou, J. Z.; Strano, M. S.; Kaner, R. B.; Mitchell, A.; Kalantar-Zadeh, K. *Adv. Funct. Mater.* **2011**, *21*, 2175–2196.
- [100] Orsini, G.; Tricoli, V. *J. Mater. Chem.* **2010**, *20*, 6299–6308.
- [101] Vioux, A. *Chem. Mater.* **1997**, *9*, 2292–2299.
- [102] Orsini, G.; Tricoli, V. *J. Mater. Chem.* **2011**, *21*, 14530–14542.

- [103] Polleux, J.; Antonietti, M.; Niederberger, M. *J. Mater. Chem.* **2006**, *16*, 3969–3975.
- [104] Debecker, D. P.; Mutin, P. H. *Chem. Soc. Rev.* **2012**, *41*, 3624–3650.
- [105] Corriu, R. J. P.; Leclercq, D.; Lefevre, P.; Mutin, P. H.; Vioux, A. *J. Mater. Chem.* **1992**, *2*, 673–674.
- [106] Acosta, S.; Corriu, R. J. P.; Leclercq, D.; Lefevre, P.; Mutin, P. H.; Vioux, A. *J. Non-Cryst. Solids* **1994**, *170*, 234–242.
- [107] Arnal, P.; Corriu, R. J. P.; Leclercq, D.; Mutin, P. H.; Vioux, A. *Chem. Mater.* **1997**, *9*, 694–698.
- [108] Bourget, L.; Corriu, R. J. P.; Leclercq, D.; Mutin, P. H.; Vioux, A. *J. Non-Cryst. Solids* **1998**, *242*, 81–91.
- [109] Corriu, R. J. P.; Leclercq, D.; Lefevre, P.; Mutin, P. H.; Vioux, A. *Chem. Mater.* **1992**, *4*, 961–963.
- [110] Debecker, D. P.; Delaigle, R.; Bouchmella, K.; Eloy, P.; Gaigneaux, E. M.; Mutin, P. H. *Catal. Today* **2010**, *157*, 125–130.
- [111] Arnal, P.; Corriu, R. J. P.; Leclercq, D.; Mutin, P. H.; Vioux, A. *Mat. Res. Soc. Symp. Proc.* **1994**, *346*, 339–344.
- [112] Aboulaich, A.; Boury, B.; Mutin, P. H. *Eur. J. Inorg. Chem.* **2011**, *24*, 3644–3649.
- [113] Chemseddine, A.; Morineau, R.; Livage, J. *Solid State Ionics* **1983**, *9-10*, 372–362.
- [114] Khyzhun, O. Y. *J. Alloys Compd.* **2000**, *305*, 1–6.
- [115] Gerand, B.; Nowogrocki, G.; Guenot, J.; Figlarz, M. *J. Solid State Chem.* **1979**, *29*, 429–434.
- [116] *X-ray Photoelectron Spectroscopy Database, Version 4.1*; National Institute of Standards and Technology, Gaithersburg, 2012.
- [117] Linsebigler, A. L.; Guangquan, L.; Yates, J. T. *Chem. Rev.* **1995**, *95*, 735–758.
- [118] Chauvin, J.; Thomas, K.; Clet, G.; Houalla, M. *J. Phys. Chem. C* **2015**, *119*, 12345–12355.
- [119] Ross-Medgaarden, E. I.; Wachs, I. E. *J. Phys. Chem. C* **2007**, *111*, 15089–15099.

- [120] Zhou, H.; Shi, Y.; Wang, L.; Zhang, H.; Zhao, C.; Hagfeldt, A.; Ma, T. *Chem. Commun.* **2013**, 49, 7626–7628.
- [121] Rawal, S. B.; Bera, S.; Lee, W. I. *Catal. Lett.* **2012**, 142, 1482–1488.
- [122] Hilaire, S.; Süess, M. J.; Kränzlin, N.; Bienkowski, K.; Solarska, R.; Augustynski, J.; Niederberger, M. *J. Mater. Chem. A* **2014**, 2, 20530–20537.
- [123] Xin, G.; Guo, W.; Ma, T. *Appl. Surf. Sci.* **2009**, 256, 165–169.
- [124] Persson, C.; Andersson, C. *Inorg. Chim. Acta* **1993**, 203, 235–238.
- [125] Zhang, G.; Liu, M. *Sens. Actuators, B* **2000**, 69, 144–152.
- [126] Watson, J. *Sens. Actuators* **1984**, 5, 29–42.
- [127] Nayral, C.; Ould-Ely, T.; Maisonnat, A.; Chaudret, B.; Fau, P.; Lescouzeres, L.; Peyre-Lavigne, A. *Adv. Mater.* **1999**, 11, 61–63.
- [128] Kolmakov, A.; Zhang, Y. X.; Cheng, G. S.; Moskovits, M. *Adv. Mater.* **2003**, 15, 997–1000.
- [129] Wu, H. B.; Chen, J. S.; Hng, H. H.; Lou, X. W. *Nanoscale* **2012**, 4, 2526–2542.
- [130] Zhang, Y. L.; Liu, Y.; Liu, M. L. *Chem. Mater.* **2006**, 18, 4643–4646.
- [131] Idota, Y.; Kubota, T.; Matsufuji, A.; Maekawa, Y.; Miyasaka, T. *Science* **1997**, 276, 1395–1397.
- [132] Saadeddin, I.; Pecquenard, B.; Manaud, J. P.; Decourt, R.; Labrugere, C.; Buffeteau, T.; Campet, G. *Applied Surface Science* **2007**, 253, 5240–5249.
- [133] Dai, Z. R.; Pan, Z. W.; Wang, Z. L. *Adv. Funct. Mater.* **2003**, 13, 9–24.
- [134] Hoel, C. A.; Mason, T. O.; Gaillard, J. F.; Poepelmeier, K. R. *Chem. Mater.* **2010**, 22, 3569–3579.
- [135] Takeguchi, T.; Anzai, Y.; Kikuchi, R.; Eguchi, K.; Ueda, W. *J. Electrochem. Soc.* **2007**, 154, B1132–B1137.
- [136] Tsukatsune, T.; Takabatake, Y.; Noda, Z.; Daio, T.; Zaitse, A.; Lyth, S. M.; Hayashi, A.; Sasaki, K. *J. Electrochem. Soc.* **2014**, 161, F1208–F1213.
- [137] Hagemeyer, A.; Hogan, Z.; Schlichter, M.; Smaka, B.; Streukens, G.; Turner, H.; Volpe, A.; Weinberg, H.; Yaccato, K. *Appl. Catal., A* **2007**, 317, 139–148.

- [138] Xu, X.; Zhang, R.; Zeng, X.; Han, X.; Li, Y.; Liu, Y.; Wang, X. *ChemCatChem* **2013**, *5*, 2025–2036.
- [139] Orel, Z. C.; Orel, B.; Hodoscek, M.; Kaucic, V. *J. Mater. Sci.* **1992**, *27*, 313–318.
- [140] Shanthi, E.; Dutta, V.; Banerjee, A.; Chopra, K. L. *J. Appl. Phys.* **1980**, *51*, 6243–6251.
- [141] Mishra, K. C.; Johnson, K. H.; Schmidt, P. C. *Phys. Rev. B* **1995**, *51*, 13972–13976.
- [142] Leite, D. R.; Mazali, I. O.; Aguiar, E. C.; Las, W. C.; Cilense, M. *J. Mater. Sci.* **2006**, *41*, 6256–6259.
- [143] Wang, Y. D.; Djerdj, I.; Antonietti, M.; Smarsly, B. *Small* **2008**, *4*, 1656–1660.
- [144] Wang, Y. D.; Mu, Q. Y.; Wang, G. F.; Zhou, Z. L. *Sens. Actuators, B* **2010**, *145*, 847–853.
- [145] Luo, L.; Bozyigit, D.; Wood, V.; Niederberger, M. *Chem. Mater.* **2013**, *25*, 4901–4907.
- [146] Mueller, V.; Rasp, M.; Rathousky, J.; Schutz, B.; Niederberger, M.; Fattakhova-Rohlfing, D. *Small* **2010**, *6*, 633–637.
- [147] Dou, M. L.; Hou, M.; Wang, F.; Liang, D.; Zhao, Q.; Shao, Z. G.; Yi, B. L. *J. Electrochem. Soc.* **2014**, *161*, F1231–F1236.
- [148] Shukla, A. K.; Arico, A. S.; El-Khatib, K. M.; Kim, H.; Antonucci, P. L. *Appl. Surf. Sci.* **1999**, *137*, 20–29.
- [149] Ke, K.; Waki, K. *J. Electrochem. Soc.* **2007**, *154*, A207–A212.
- [150] Senoo, Y.; Kakinuma, K.; Uchida, M.; Uchida, H.; Deki, S.; Watanabe, M. *RSC Adv.* **2014**, *4*, 32180–32188.
- [151] Takasaki, F.; Matsuie, S.; Takabatake, Y.; Noda, Z.; Hayashi, A.; Shiratori, Y.; Ito, K.; Sasaki, K. *J. Electrochem. Soc.* **2011**, *158*, B1270–B1275.
- [152] Wang, Y.; Brezesinski, T.; Antonietti, M.; Smarsly, B. *ACS Nano* **2009**, *3*, 1373–1378.
- [153] Gokulakrishnan, V.; Parthiban, S.; Jeganathan, K.; Ramamurthi, K. *J. Mater. Sci.* **2011**, *46*, 5553–5558.
- [154] Stefik, M.; Cornuz, M.; Mathews, N.; Hisatomi, T.; Mhaisalkar, S.; Grätzel, M. *Nano Lett.* **2012**, *12*, 5431–5435.
- [155] Cavaliere, S.; Subianto, S.; Savych, I.; Tillard, M.; Jones, D. J.; Rozière, J. *J. Phys. Chem. C* **2013**, *117*, 18298–18307.

- [156] Turgut, G.; Keskenler, E. F.; Aydin, S.; Sönmez, E.; Doğan, S.; Düzgün, B.; Ertuğrul, M. *Superlattices and Microstruct.* **2013**, *56*, 107–116.
- [157] Hu, Y.; Yella, A.; Guldin, S.; Schreier, M.; Stellacci, F.; Grätzel, M.; Stefić, M. *Adv. Energy Mater.* **2014**, *4*, 1400510–1400517.
- [158] Nütz, T.; zum Felde, U.; Haase, M. *J. Chem. Phys.* **1999**, *110*, 12142–12150.
- [159] Hu, P.; Yang, H. *Appl. Clay Sci.* **2010**, *48*, 368–374.
- [160] Rawal, S. B.; Chakraborty, A. K.; Kim, Y. J.; Kim, H. J.; Lee, W. I. *RSC Adv.* **2012**, *2*, 622–630.
- [161] Du, Y.; Yan, J.; Meng, Q.; Wang, J.; Dai, H. *Mater. Chem. Phys.* **2012**, *133*, 907–912.
- [162] Wang, Y.; Zheng, J.; Jiang, F.; Zhang, M. *J. Mater. Sci.: Mater. Electron* **2014**, *25*, 4524–4530.
- [163] Neimark, A. V.; Ravikovitch, P. I., *Characterization of Porous Solids V*; Elsevier, 2000.
- [164] Shannon, R. D. *Acta Crystallogr.* **1976**, *A32*, 751–767.
- [165] Vijayarangamuthu, K.; Rath, S. *Appl. Phys. A* **2014**, *114*, 1181–1188.
- [166] Jin, H.; Ju, Y.; Pang, G.; Dong, W.; Wan, Q.; Sun, Y.; Feng, S. *Mater. Chem. Phys.* **2004**, *85*, 58–62.
- [167] Avadhut, Y. S.; Weber, J.; Hammarberg, E.; Feldmann, C.; Schellenberg, I.; Pöttgen, R.; Schmedt auf der Günne, J. *Chem. Mater.* **2011**, *23*, 1526–1538.
- [168] Issac, I.; Heinzmann, R.; Becker, S. M.; Bräuniger, T.; Zhao-Karger, Z.; Adelhelm, C.; Chakravadhanula, V. S. K.; Kübel, C.; Ulrich, A. S.; Indris, S. *RSC Adv.* **2012**, *2*, 10700–10707.
- [169] Popescu, D. A.; Herrmann, J.-M.; Ensuque, A.; Bozon-Verduraz, F. *Phys. Chem. Chem. Phys.* **2001**, *3*, 2522–2530.
- [170] Canevali, C.; Chiodini, N.; Morazzoni, F.; Scotti, R. *J. Mater. Chem.* **1999**, *10*, 773–778.
- [171] Ushikubo, T.; Koike, Y.; Wada, K.; Xie, L.; Wang, D.; Guo, X. *Catal. Today* **1996**, *28*, 59–69.
- [172] Li, P.; Chen, I.-W.; Penner-Hahn, J. E. *J. Am. Ceram. Soc.* **1994**, *77*, 1289–1295.

- [173] Carmo, M.; Fritz, D. L.; Mergel, J.; Solten, D. *Int. J. Hydrogen Energy* **2013**, *38*, 4901–4934.
- [174] Russell, J. H.; Nuttall, L. J.; Fickett, A. P. *Prepr. Pap. - Am. Chem. Soc., Div. Fuel Chem.* **1973**, *18*, 24–40.
- [175] Fabbri, E.; Haberer, A.; Waltar, K.; Kötz, R.; Schmidt, T. J. *Catal. Sci. Technol.* **2014**, *4*, 3800–3821.
- [176] Matsumoto, Y.; Sato, E. *Mater. Chem. Phys.* **1986**, *14*, 397–426.
- [177] Bockris, J. O. *J. Chem. Phys.* **1956**, *24*, 817–827.
- [178] Krasil'shchikov, A. I. *Zh. Fiz. Khim.* **1963**, *37*, 273.
- [179] Wade, W. H.; Hackerman, N. *Trans. Faraday Soc.* **1957**, *53*, 1636–1647.
- [180] Antolini, E. *ACS Catal.* **2014**, *4*, 1426–1440.
- [181] Neophytides, S. G.; Murase, K.; Zafeiratos, S.; Papakonstantinou, G.; Paloukis, F. E.; Krstajic, N. V.; Jaksic, M. M. *J. Phys. Chem. B* **2006**, *110*, 3030–3042.
- [182] Krstajic, N. V.; Vracar, L. M.; Radmilovic, V. R.; Neophytides, S. G.; Labou, M.; Jaksic, J. M.; Tunold, R.; Falaras, P.; Jaksic, M. M. *Surf. Sci.* **2007**, *601*, 1949–1966.
- [183] Ma, L. R.; Sui, S.; Zhai, Y. C. *Int. J. Hydrogen Energy* **2009**, *34*, 678–684.
- [184] Polonsky, J.; Petrushina, I. M. M.; Christensen, E.; Bouzek, K.; Prag, C. B. B. *Int. J. Hydrogen Energy* **2012**, *37*, 2173–2181.
- [185] Nikiforov, A. V.; Tomas Garcia, A. L.; Petrushina, I. M.; Christensen, E.; Bjerrum, N. J. *Int. J. Hydrogen Energy* **2011**, *36*, 5797–5805.
- [186] Siracusano, S.; Baglio, V.; D'Urso, C.; Antonucci, V.; Arico, A. S. *Electrochim. Acta* **2009**, *54*, 6292–6299.
- [187] Wang, X.-M.; Hu, J.-M.; Zhang, J.-Q. *Electrochim. Acta* **2010**, *55*, 4587–4593.
- [188] Xu, J.-Y.; Liu, G.-Y.; Li, J.-L.; Wang, X.-D. *Electrochim. Acta* **2012**, *59*, 105–112.
- [189] Liu, G.-Y.; Xu, J.-Y.; Wang, Y.; Wang, X.-D. *J. Mater. Chem. A* **2015**, *3*, 20791–20800.
- [190] Di Blasi, A.; D'Urso, C.; Baglio, V.; Antonucci, V.; Arico, A. S.; Ornelas, R.; Matteucci, F.; Orozco, G.; Beltran, D.; Meas, Y.; Arriaga, L. G. *J. Appl. Electrochem.* **2009**, *39*, 191–196.

- [191] Osman, J. R.; Crayston, J. A.; Pratt, A.; Richens, D. T. *J. Sol-Gel Sci. Technol.* **2007**, *44*, 219–225.
- [192] Osman, J. R.; Crayston, J. A.; Pratt, A.; Richens, D. T. *J. Sol-Gel Sci. Technol.* **2008**, *46*, 126–132.
- [193] Adams, R.; Shriner, R. L. *J. Am. Chem. Soc.* **1923**, *45*, 2171–2179.
- [194] Hutchings, R.; Müller, K.; Kötz, R.; Stucki, S. *J. Mat. Sci.* **1984**, *19*, 3987–3994.
- [195] Lasch, K.; Jörissen, L.; Garche, J. *J. Power Sources* **1999**, *84*, 225–230.
- [196] Marshall, A.; Borresen, B.; Hagen, G.; Tsyppkin, M.; Tunold, R. *Mater. Chem. Phys.* **2005**, *94*, 226–232.
- [197] Song, S.; Zhang, H.; Ma, C.; Shao, Z.; Baker, R. T.; Yi, B. *Int. J. Hydrogen Energy* **2008**, *33*, 4955–4961.
- [198] Patru, A.; Rabis, A.; Temmel, S. E.; Kotz, R.; Schmidt, T. *J. Catal. Today* **2016**, *262*, 161–169.
- [199] McLachlan, D. S.; Blaszkiewicz, M.; Newnham, R. E. *J. Am. Ceram. Soc.* **1990**, *73*, 2187–2203.
- [200] Konstantinova, O. V.; Kuz'mov, A. V.; Skorokhod, V. V.; Shtern, M. B. *Powder Metall. Met. Ceram.* **2007**, *46*, 25–31.
- [201] Balberg, I. *Phys. Rev. Lett.* **1987**, *59*, 1305–1308.
- [202] Carmona, F.; Conet, R.; Delhaes, P. *J. Appl. Phys.* **1987**, *61*, 2550–2557.
- [203] Deprez, N.; McLachlan, D. S. *J. Phys. D: Appl. Phys.* **1988**, *D21*, 101–107.
- [204] Prouzet, E. *J. Phys.: Condens. Matter* **1995**, *7*, 8027–8033.
- [205] Mo, Y.; Stefan, I. C.; Cai, W.-B.; Dong, J.; Carey, P.; Scherson, D. A. *J. Phys. Chem. B* **2002**, *106*, 3681–3686.
- [206] Cruz, A. M.; Carretero, N. M.; Moral-Vico, J.; Fraxedas, J.; Lozano, P.; Subias, G.; Padial, V.; Carballo, M.; Collazos-Castro, J. E.; Casan-Pastor, N. *J. Phys. Chem. C* **2012**, *116*, 5155–5168.
- [207] Igarashi, H.; Fujino, T.; Zhu, Y.; Uchida, H.; Watanabe, M. *Phys. Chem. Chem. Phys.* **2001**, *3*, 306–314.

- [208] Stamenkovic, V. R.; Fowler, B.; Mun, B. S.; Wang, G. F.; Ross, P. N.; Lucas, C. A.; Markovic, N. M. *Science* **2007**, *315*, 493–497.
- [209] Antolini, E.; Salgado, J. R. C.; Gonzalez, E. R. *J. Power Sources* **2006**, *160*, 957–968.
- [210] Zhu, C.; Dong, S. *Nanoscale* **2013**, *5*, 1753–1767.
- [211] Shao, M.; Peles, A.; Shoemaker, K. *Nano Lett.* **2011**, *11*, 3714–3719.
- [212] Schmidt, T. J.; Paulus, U. A.; Gasteiger, H. A.; Behm, R. J. *J. Electroanal. Chem.* **2001**, *508*, 41–47.
- [213] Yadav, A. P.; Nishikata, A.; Tsuru, T. *Electrochim. Acta* **2007**, *52*, 7444–7452.
- [214] Lam, A.; Li, H.; Zhang, S.; Wang, H.; Wilkinson, D. P.; Wessel, S.; Cheng, T. T. H. *J. Power Sources* **2012**, *205*, 235–238.
- [215] Shrestha, B. R.; Tada, E.; Nishikata, A. *Electrochim. Acta* **2014**, *143*, 161–167.
- [216] Job, N.; Chatenet, M.; Berthon-Fabry, S.; Hermany, S.; Maillard, F. *J. Power Sources* **2012**, *240*, 294–305.
- [217] Laurent-Brocq, M.; Job, N.; Eskenazi, D.; Pireaux, J.-J. *Appl. Catal., B* **2014**, *147*, 453–463.
- [218] Ramirez-Meneses, E.; Dominguez-Crespo, M. A.; Montiel-Palma, V.; Chavez-Herrera, V. H.; Gomez, E.; Hernandez-Tapia, G. *J. Alloys Compd.* **2009**, *483*, 573–577.
- [219] Saida, T.; Sugimoto, W.; Takasu, Y. *Electrochim. Acta* **2010**, *55*, 857–864.
- [220] de Jong, K., *Synthesis of Solid Catalysts*; Wiley, 2009.
- [221] White, R. J.; Luque, R.; Budarin, V. L.; Clark, J. H. *Chem. Soc. Rev.* **2009**, *38*, 481–494.
- [222] Burch, R. *J. Catal.* **1981**, *71*, 348–359.
- [223] Meitzner, G.; Via, G. H.; Lytle, F. W.; Fung, S. C.; Sinfelt, J. H. *J. Phys. Chem.* **1988**, *92*, 2925–2932.
- [224] Humblot, F.; Didillon, D.; Lepeltier, F.; Candy, J.-P.; Corker, J.; Clause, O.; Bayard, F.; Basset, J.-M. *J. Am. Chem. Soc.* **1998**, *120*, 137–146.
- [225] Hsieh, C.-T.; Liu, Y.-Y.; Chen, W.-Y.; Hsieh, Y.-H. *Int. J. Hydrogen Energy* **2011**, *36*, 15766–15774.

- [226] Beyhan, S.; Sahin, N. E.; Pronier, S.; Leger, J.-M. *Electrochim. Acta* **2015**, *151*, 565–573.
- [227] Pelzer, K.; Laleu, B.; Lefebvre, F.; Philippot, K.; Chaudret, B.; Candy, J.-P.; Basset, J.-M. *Chem. Mater.* **2004**, *16*, 4937–4941.
- [228] Ramirez, E. E.; Philippot, K.; Lecante, P.; Chaudret, B. *Adv. Funct. Mater.* **2007**, *17*, 2219–2228.
- [229] Amiens, C.; Chaudret, B.; Ciuculescu-Pradines, D.; V, C.; Fajerweg, K.; Fau, P.; Kahn, M.; Maisonnat, A.; Soulantica, K.; Philippot, K. *New J. Chem.* **2013**, *37*, 3374–3401.
- [230] Laurent, P.; Baudouin, D.; Fenet, B.; Veyre, L.; Donet, S.; Copéret, C.; Thieuleux, C. *New J. Chem.* **2014**, *38*, 5952–5956.
- [231] Laurent, P.; *Molecular Approach Towards the Design and the Preparation of Supported and Non-Supported Pt- and Pd-based Nanoparticles*; PhD thesis, University of Lyon, **2012**.
- [232] Moseley, K.; Maitlis, P. M. *J. Chem. Soc. D* **1971**, 982–983.
- [233] Binninger, T.; Fabbri, E.; Kötz, R.; Schmidt, T. J. *J. Electrochem. Soc.* **2014**, *161*, H121–H128.
- [234] Fang, B.; Chaudhari, N. K.; Kim, M.-S.; Kim, J. H.; Yu, J.-S. *J. Am. Chem. Soc.* **2009**, *131*, 15330–15338.
- [235] Binninger, T.; Garganourakis, M.; Han, J.; Patru, A.; Fabbri, E.; Sereda, O.; Kötz, R.; Menzel, A.; Schmidt, T. J. *Phys. Rev. Applied* **2015**, *3*, 024012.
- [236] Yuen, M. F.; Lauks, I. *Solid State Ionics* **1983**, *11*, 19–29.
- [237] Gottesfeld, S.; Redondo, A.; Rubenstein, I.; Feldberg, S. W. *J. Electroanal. Chem.* **1989**, *265*, 15–22.
- [238] Silva, T. M.; Simões, A. M. P.; Ferreira, M. G. S.; Walls, M.; Belo, M. D. S. *J. Electroanal. Chem.* **1998**, *441*, 5–12.
- [239] Lervik, I. A.; Tsyppkin, M.; Owe, L.-E.; Sunde, S. *J. Electroanal. Chem.* **2010**, *645*, 135–142.
- [240] Yao, W.; Yang, J.; Wang, J.; Nuli, Y. *Electrochem. Commun.* **2007**, *9*, 1029–1034.
- [241] Kitchin, J. R.; Nørskov, J. K.; Barteau, M. A.; Chen, J. G. *J. Chem. Phys.* **2004**, *120*, 10240–10246.

- [242] Schmidt, T. J.; Gasteiger, H. A.; Stäb, G. D.; Urban, P. M.; Kolb, D. M.; Behm, R. J. *J. Electrochem. Soc.* **1998**, *145*, 2354–2358.
- [243] Reiser, C. A.; Bregoli, L.; Patterson, T. W.; Yi, J. S.; Yang, J. D.; Perry, M. L.; Jarvi, T. D. *Electrochem. Solid-State Lett.* **2005**, *8*, A273–A276.
- [244] Tang, H.; Qi, Z.; Ramani, M.; Elter, J. F. *J. Power Sources* **2006**, *158*, 1306–1312.
- [245] Büchi, F. N.; Inaba, M.; Schmidt, T. J., *Polymer Electrolyte Fuel Cell Durability*; Springer, 2009.
- [246] Meekins, B. H.; Kamat, P. V. *J. Phys. Chem. Lett.* **2011**, *2*, 2304–2310.

Appendix

A1 Blue Tungsten Oxide: Synthesis, Electrochemical Properties and Photocatalytic Performance

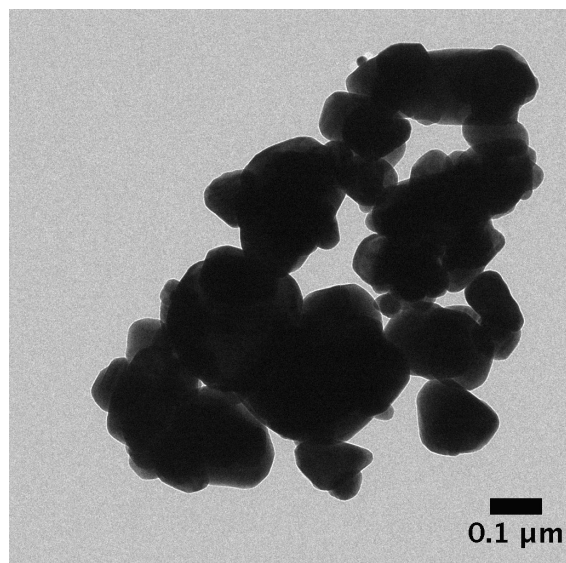


Figure A1: Bright Field TEM image of commercial WO₃.

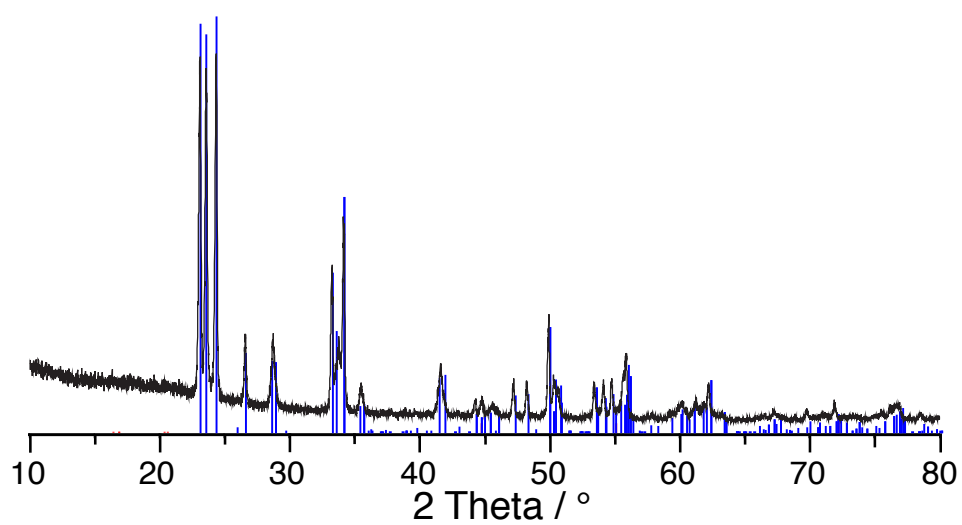


Figure A2: X-ray powder diffraction pattern of commercial WO₃ (black) with monoclinic WO₃ reference pattern (blue, ICDD 00-083-0951).

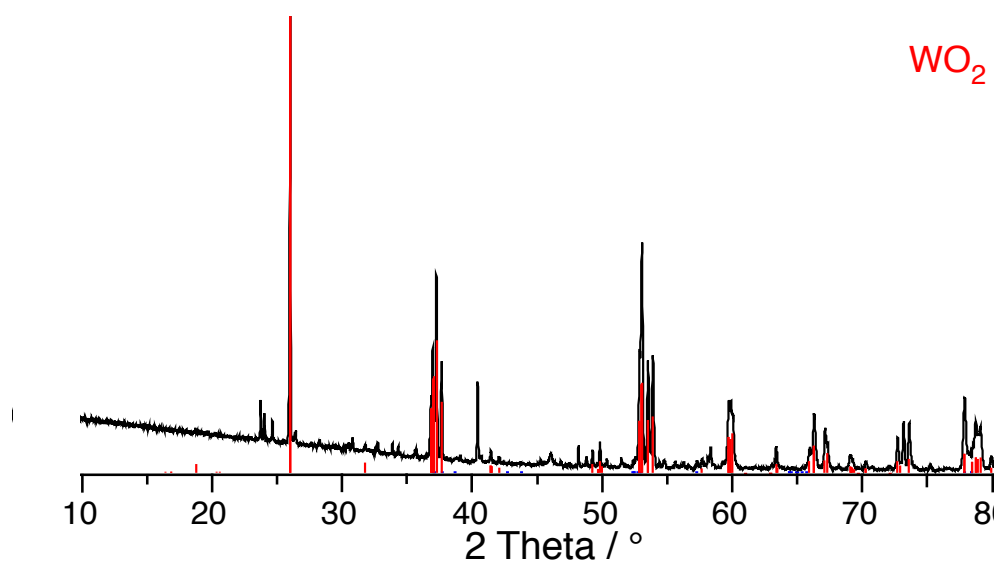


Figure A3: X-ray powder diffraction pattern of commercial WO_2 (black) with WO_2 reference pattern (red, ICDD 00-086-0134).

A2 Niobium and Antimony-doped Tin Oxide: Structural Differences and Consequences for Electrical Conductivity

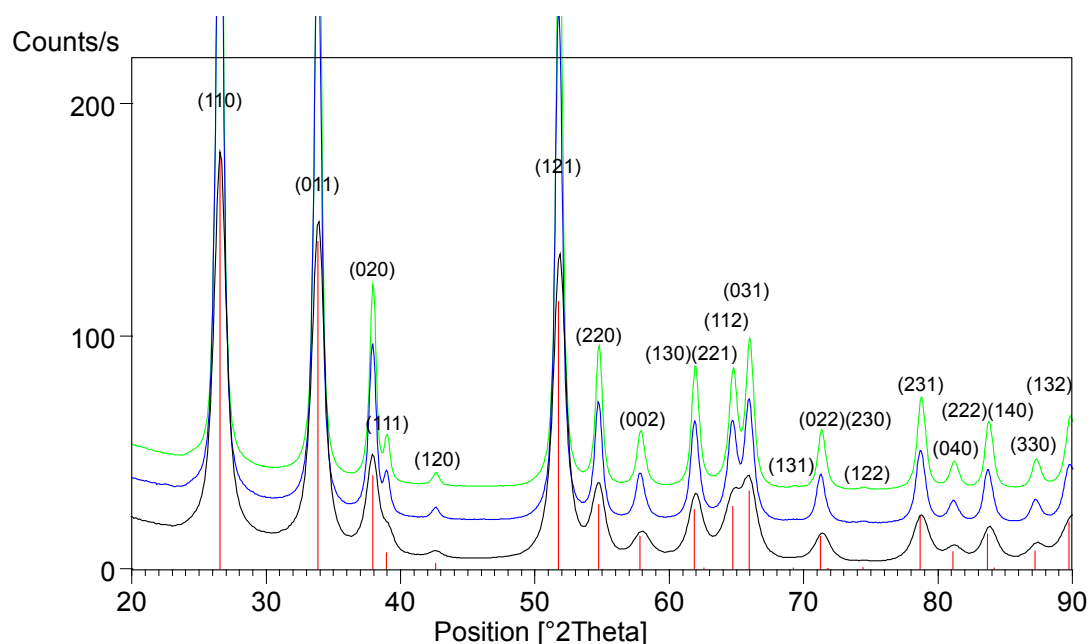


Figure A4: XRD powder diffraction patterns of SnO_2 (green), $\text{SnO}_2:\text{Sb}$ (blue) and $\text{SnO}_2:\text{Nb}$ (black) measured on a glass substrate at room temperature after the HT-XRD measurements. The red lines represent the theoretical peak positions of Cassiterite SnO_2 (ICSD 98-001-7021). Major diffraction peaks are indexed (hkl) and assigned to cassiterite SnO_2 .

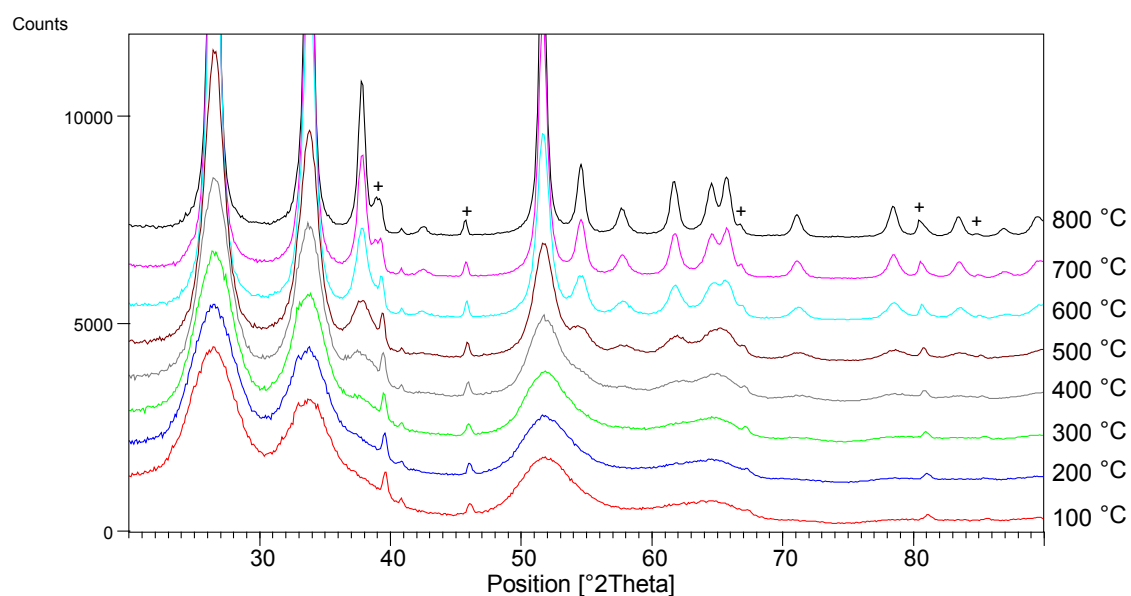


Figure A5: HT-XRD diffraction patterns of SnO_2 during heating cycle 1. Peaks due to the Pt heating strip are denoted by a + sign. All others correspond to cassiterite SnO_2 .

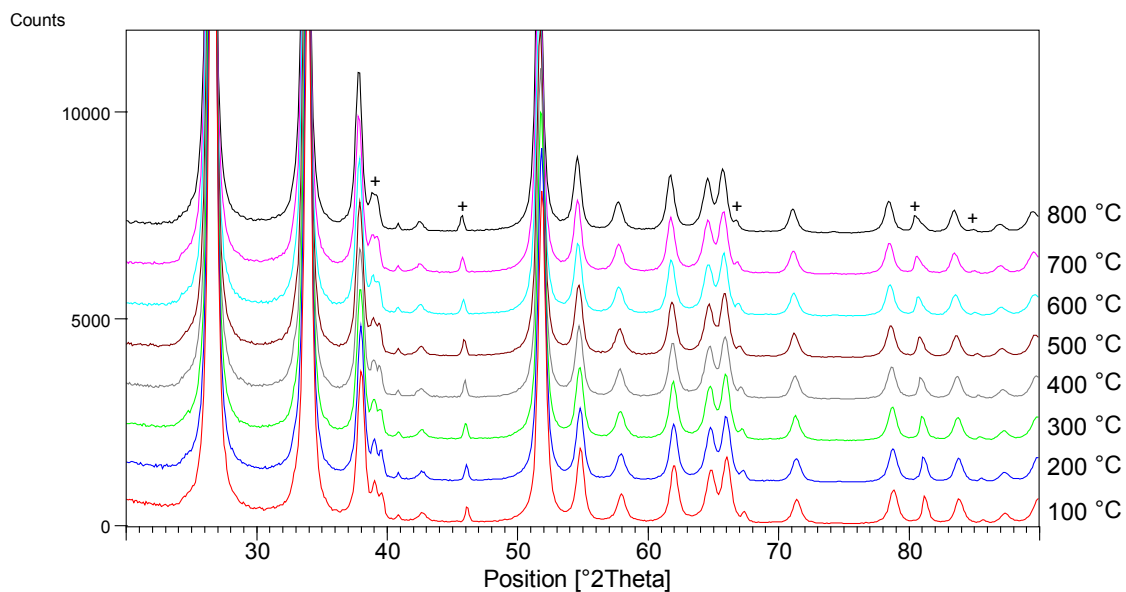


Figure A6: HT-XRD diffraction patterns of SnO_2 during heating cycle 2. Peaks due to the Pt heating strip are denoted by a + sign. All other corresponds to cassiterite SnO_2 .

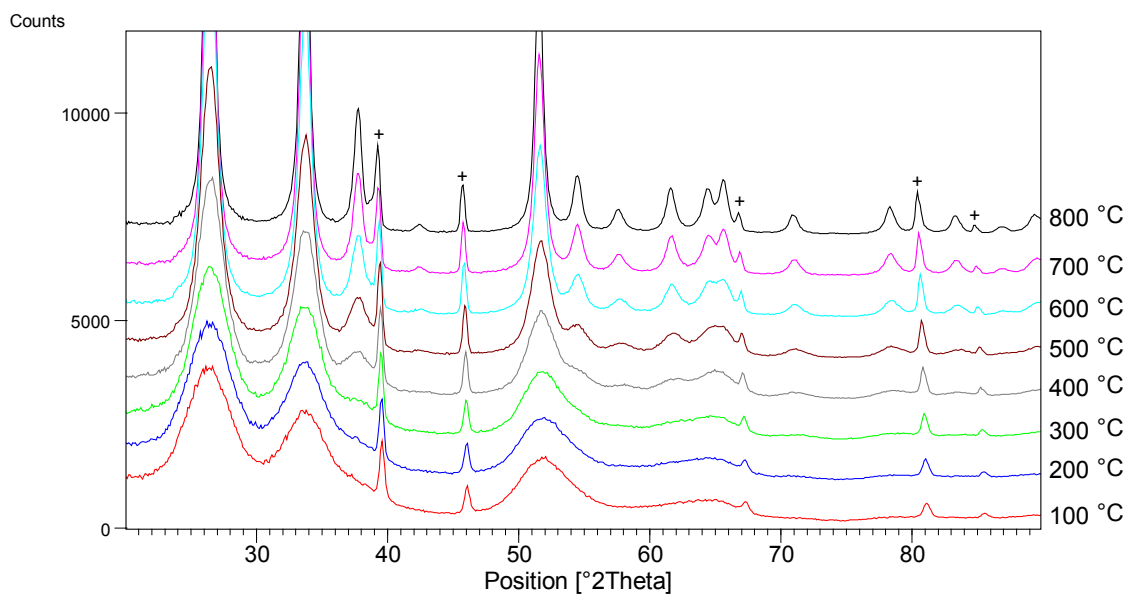


Figure A7: HT-XRD diffraction patterns of $\text{SnO}_2\text{:Sb}$ during heating cycle 1. Peaks due to the Pt heating strip are denoted by a + sign. All others correspond to cassiterite SnO_2 .

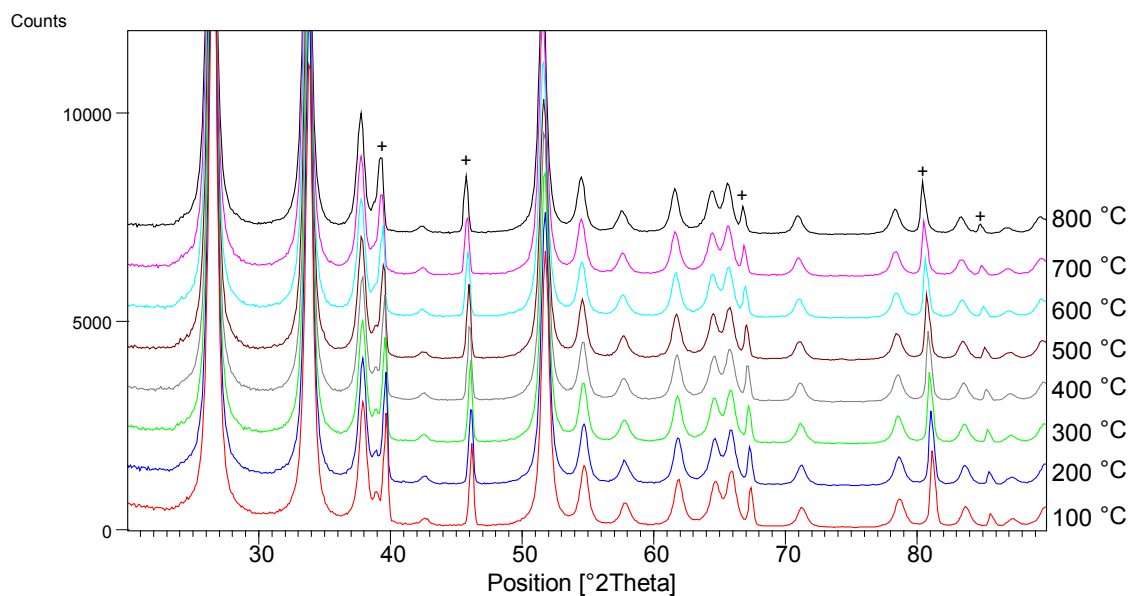


Figure A8: HT-XRD diffraction patterns of $\text{SnO}_2\text{:Sb}$ during heating cycle 2. Peaks due to the Pt heating strip are denoted by a + sign. All others correspond to cassiterite SnO_2 .

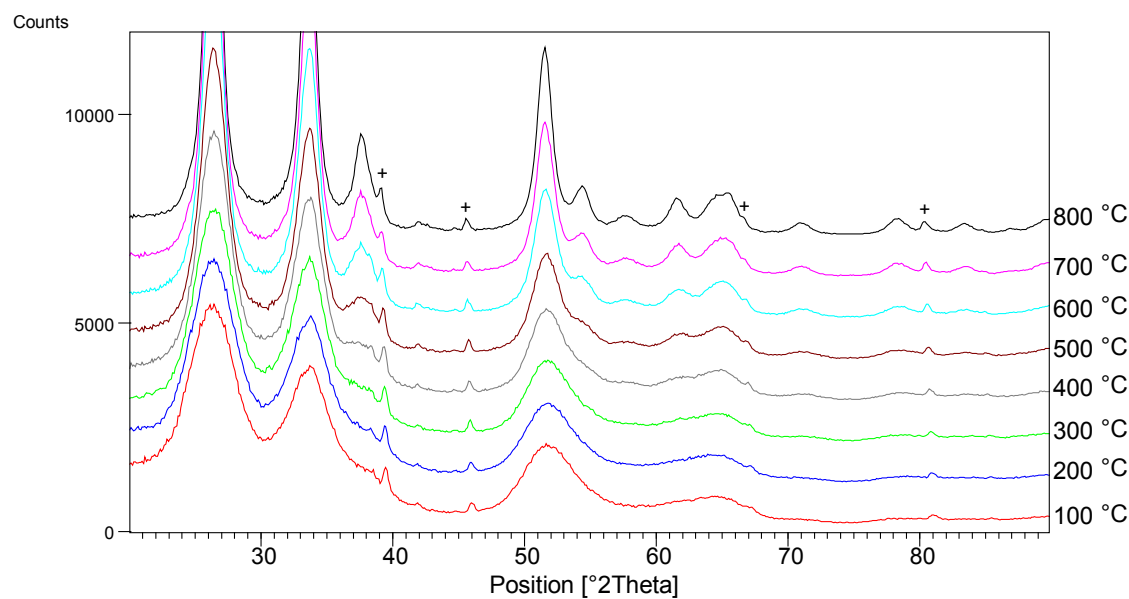


Figure A9: HT-XRD diffraction patterns of $\text{SnO}_2\text{:Nb}$ during heating cycle 1. Peaks due to the Pt heating strip are denoted by a + sign. All others correspond to cassiterite SnO_2 .

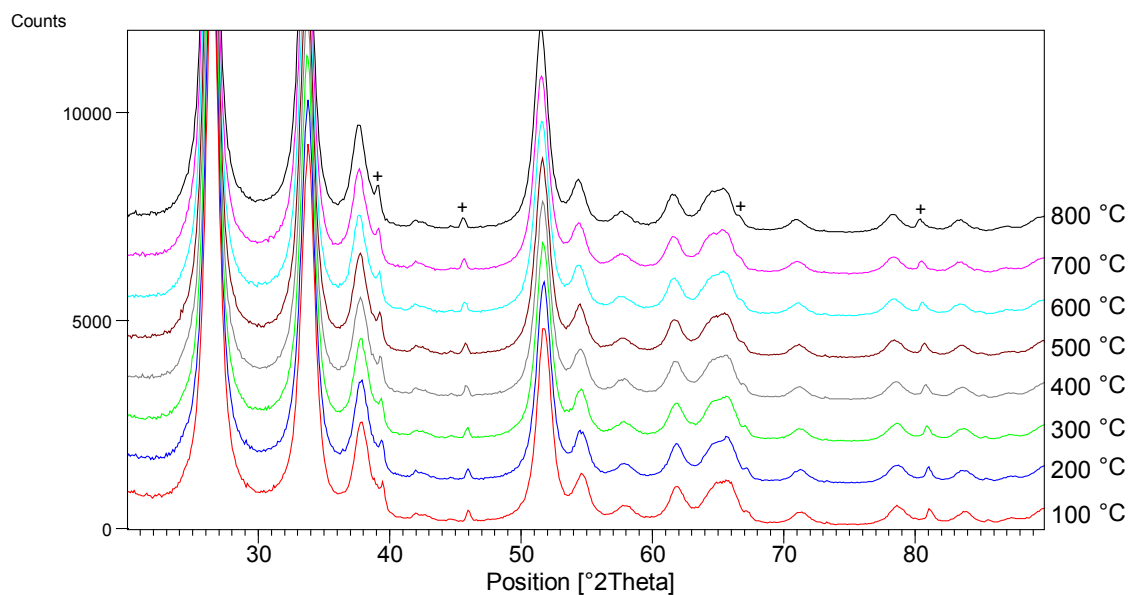


Figure A10: HT-XRD diffraction patterns of $\text{SnO}_2\text{:Nb}$ during heating cycle 2. Peaks due to the Pt heating strip are denoted by a + sign. All others correspond to cassiterite SnO_2 .

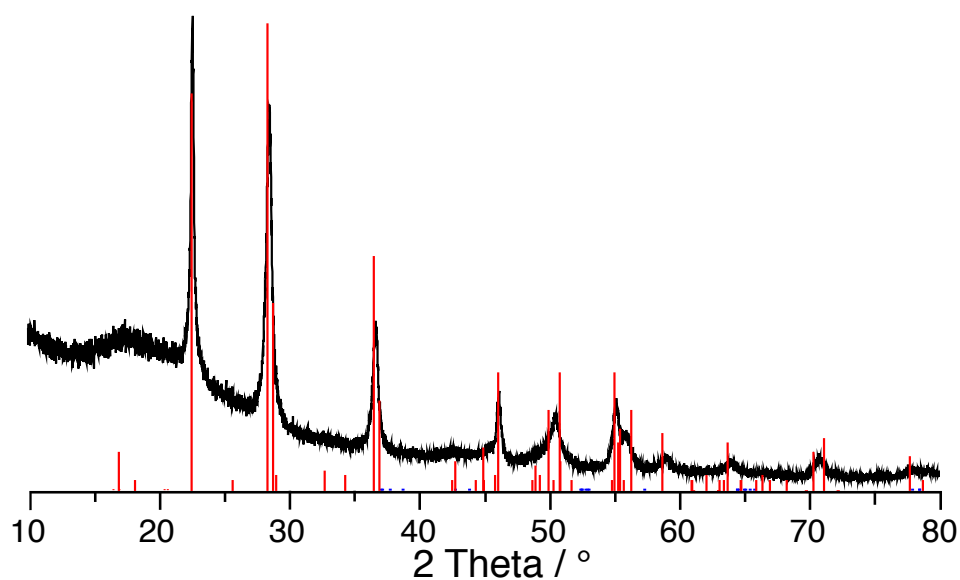


Figure A11: X-ray powder diffraction pattern of Nb_2O_5 prepared by co-precipitation with orthorhombic Nb_2O_5 reference pattern (ICDD 00-030-0873).

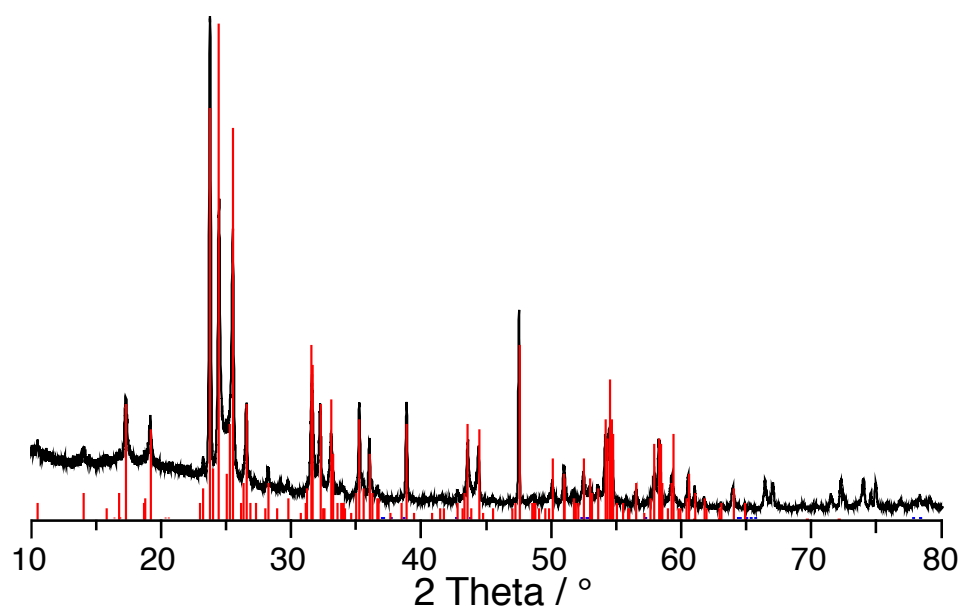


Figure A12: X-ray powder diffraction pattern of commercial Nb₂O₅ with monoclinic Nb₂O₅ reference pattern (ICDD 00-037-1468).

A3 Iridium Titanium Oxide: Preparation, Optimisation and Application in Oxygen Evolution

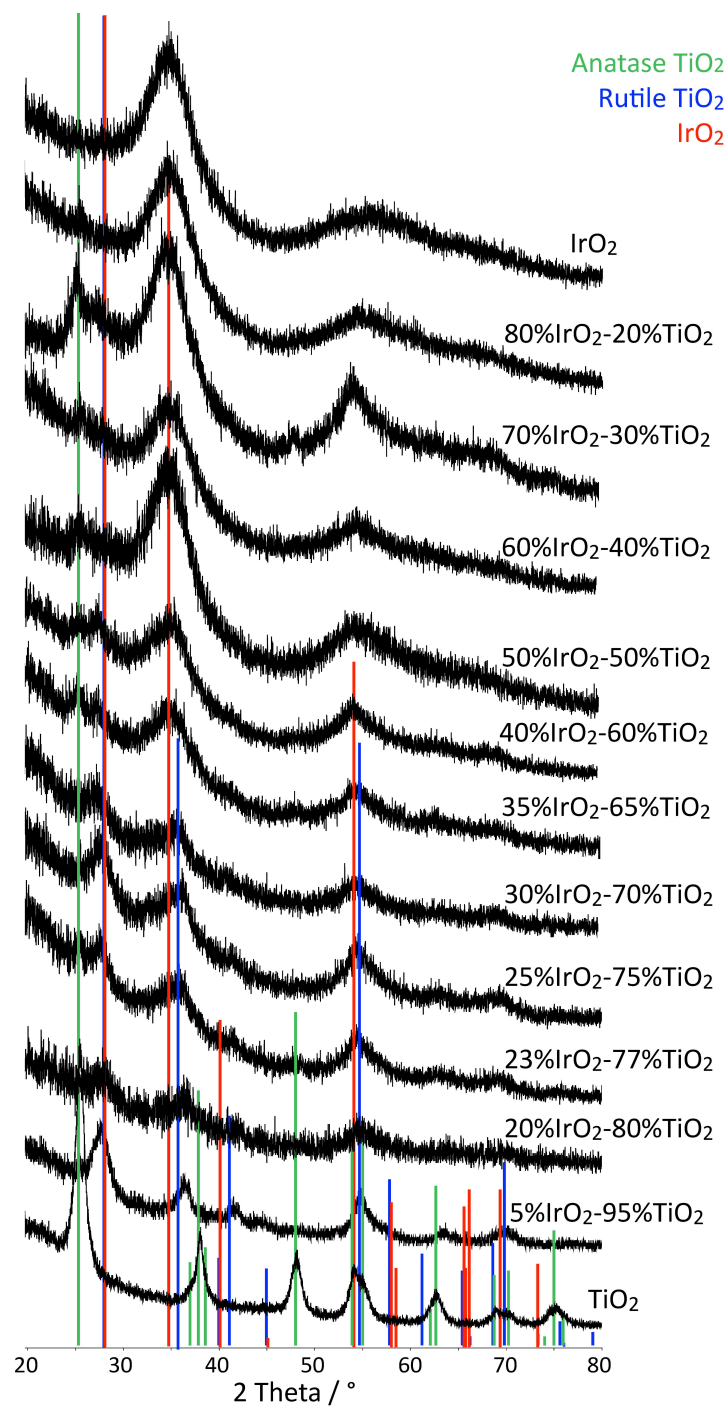


Figure A13: Powder XRD diffraction patterns of various additional IrO₂-TiO₂ compositions with reference patterns of anatase TiO₂ (green, ICDD 00-084-1286), rutile TiO₂ (blue, ICDD 00-086-0147) and IrO₂ (red, ICDD 00-015-0870) respectively.

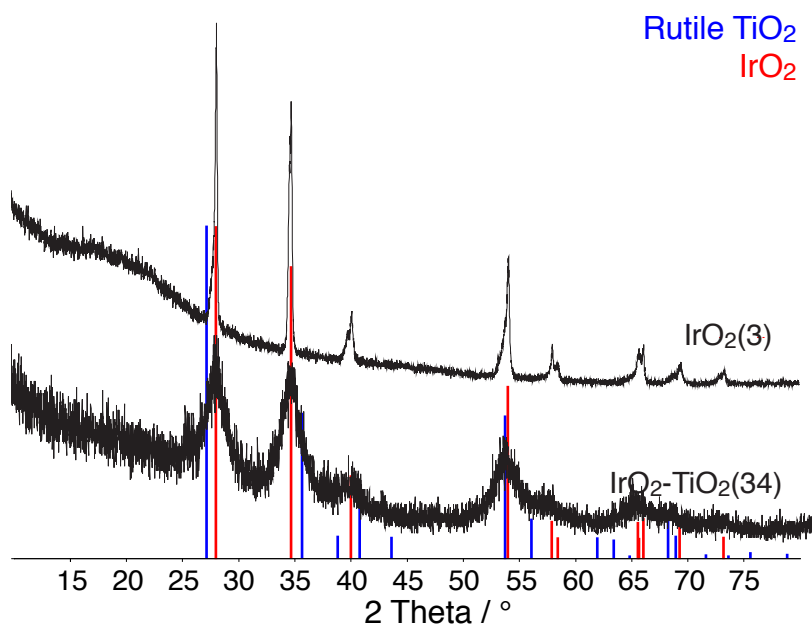


Figure A14: X-ray powder diffraction patterns of commercial materials tested in OER with reference patterns of rutile TiO_2 (blue, ICDD 00-086-0147) and IrO_2 (red, 00-015-0870).

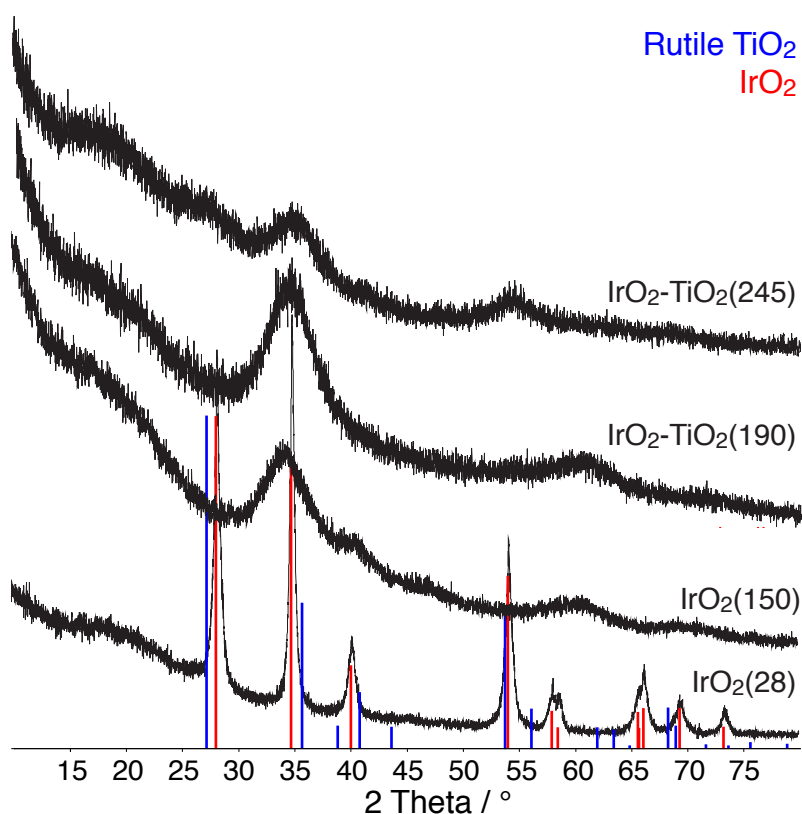


Figure A15: X-ray powder diffraction patterns of homemade materials tested in OER with reference patterns of rutile TiO_2 (blue, ICDD 00-086-0147) and IrO_2 (red, 00-015-0870).

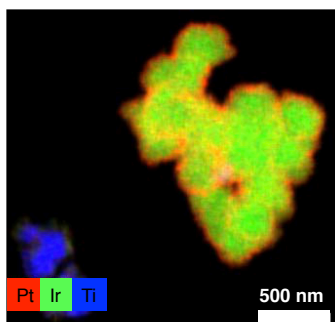


Figure A16: EDX map of Pt nanoparticles supported on IrO₂-TiO₂(34).

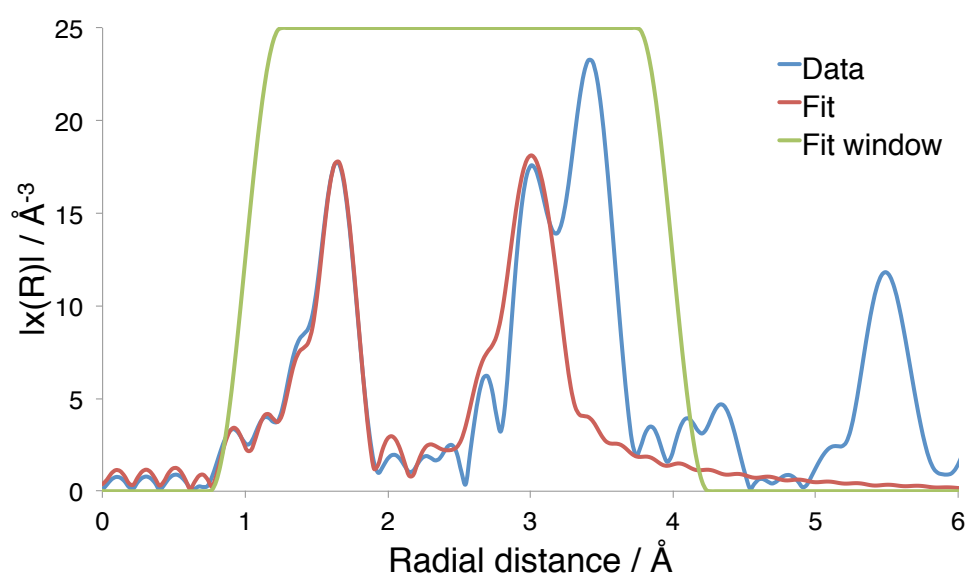


Figure A17: EXAFS data fit for IrO₂(28).

Table A1: EXAFS data fir for IrO₂(28)

Name	N	SO ₂	$\sigma^2 / \text{\AA}^2$	e_0 / eV	$\Delta R / \text{\AA}$	$R_{eff} / \text{\AA}$	$R / \text{\AA}$
OSS	6	0.874	0.0022	8.868	0.00189	1.983	1.98489
Ir1.1	2	0.874	0.00081	8.868	0.00047	3.1544	3.15487

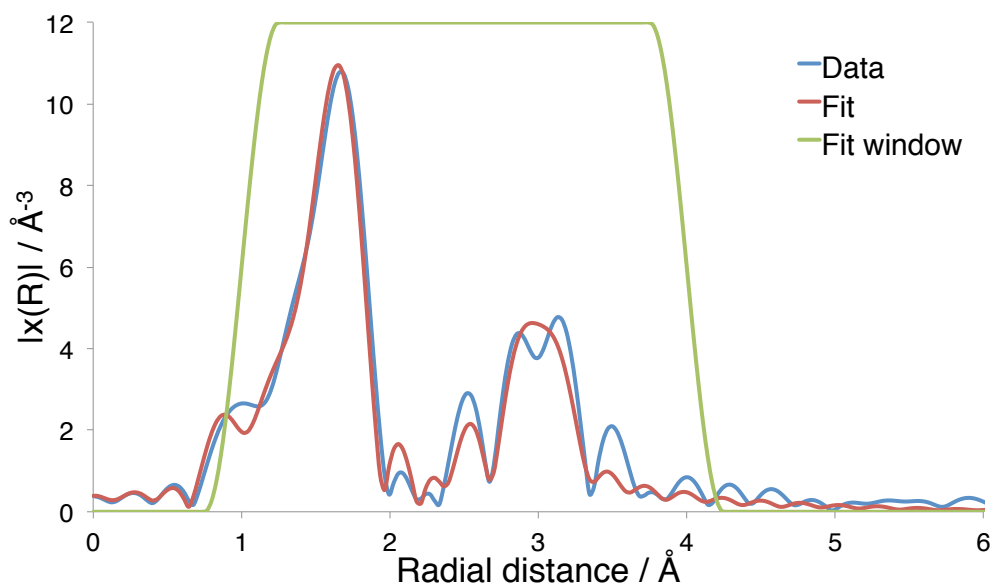


Figure A18: EXAFS data fit for IrO₂(150).

Table A2: EXAFS data fit for IrO₂(150)

Name	N	SO ₂	$\sigma^2 / \text{\AA}^2$	e_0 / eV	$\Delta R / \text{\AA}$	$R_{eff} / \text{\AA}$	$R / \text{\AA}$
OSS	6	0.874	0.00496	7.598	0.03964	1.983	2.02264
Ir1.1	2	0.874	0.0035	7.598	-0.03554	3.1544	3.11886

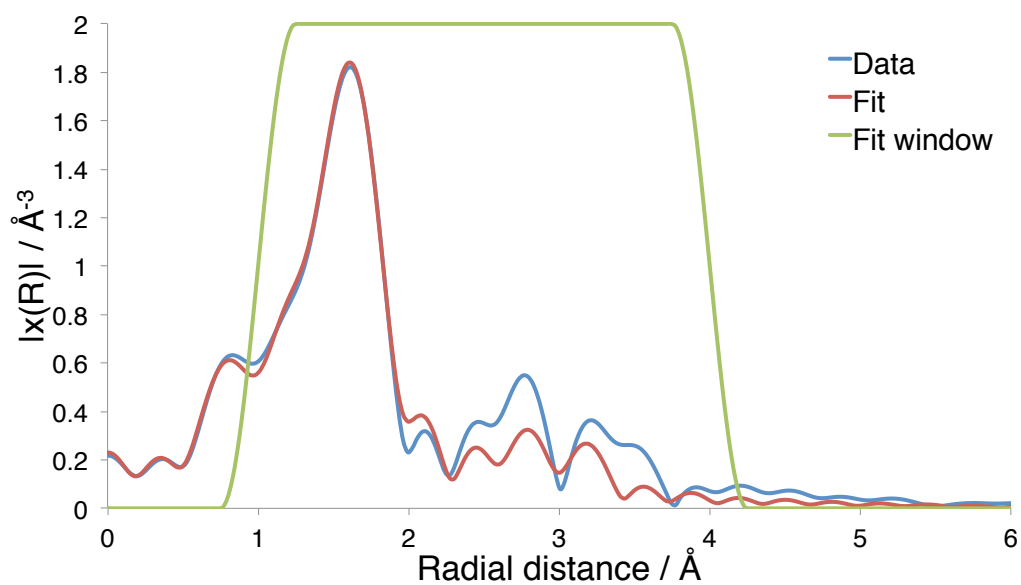


Figure A19: EXAFS data fit for IrO₂-TiO₂(245).

Table A3: EXAFS data fir for IrO₂-TiO₂(245)

Name	N	SO ₂	$\sigma^2 / \text{\AA}^2$	e_0 / eV	$\Delta R / \text{\AA}$	$R_{eff} / \text{\AA}$	$R / \text{\AA}$
OSS	6	0.89	0.00507	9.898	0.03026	1.983	2.01326
Ir1.1	2	0.89	0.00465	9.898	-0.04447	3.1544	3.10993

A4 Oxide Supported Pt Nanoparticles: Preparation, Activity and Stability in Oxygen Reduction

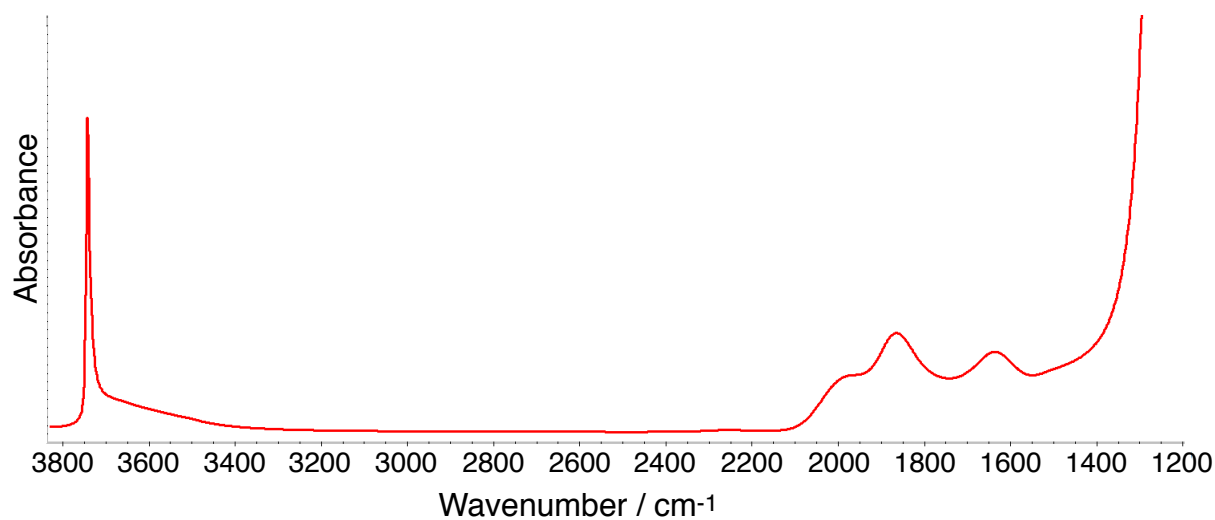


Figure A20: IR spectrum of Pt/SiO₂, prepared by impregnation and calcination of octylsilane stabilised Pt colloid. The absence of C-H confirms calcination of 400 °C is sufficient to remove the stabilising ligand.

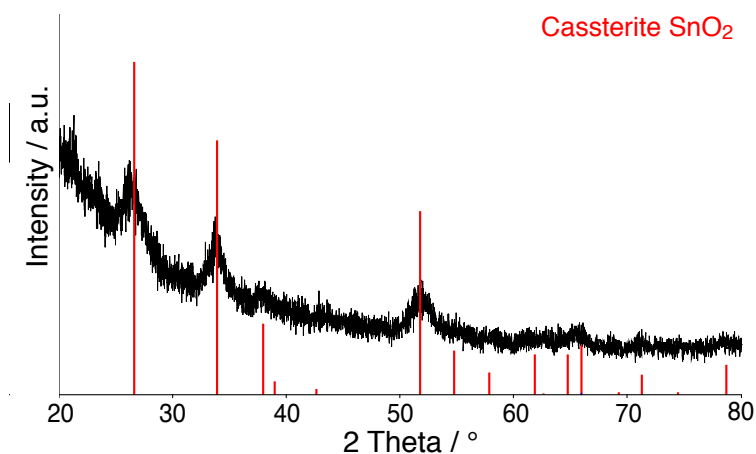


Figure A21: XRD powder diffraction pattern of SnO₂:Sb used for Pt colloid impregnation with reference pattern of cassiterite SnO₂ (ICDD 00-077-0447).

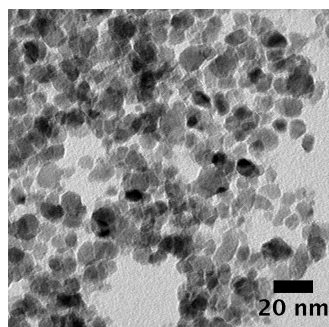


Figure A22: Bright field TEM image of $\text{SnO}_2\text{:Sb}$ used for Pt colloid impregnation.

Table A4: Surface area and Sb content of $\text{SnO}_2\text{:Sb}$ used for Pt colloid impregnation

$S_{BET} / \text{m}^2.\text{g}^{-1}$	Sb content / wt%
76	3.4

Table A5: Surface area of supports used for HPD

Support	$S_{BET} / \text{m}^2.\text{g}^{-1}$
SiO_2	200
TiO_2	250

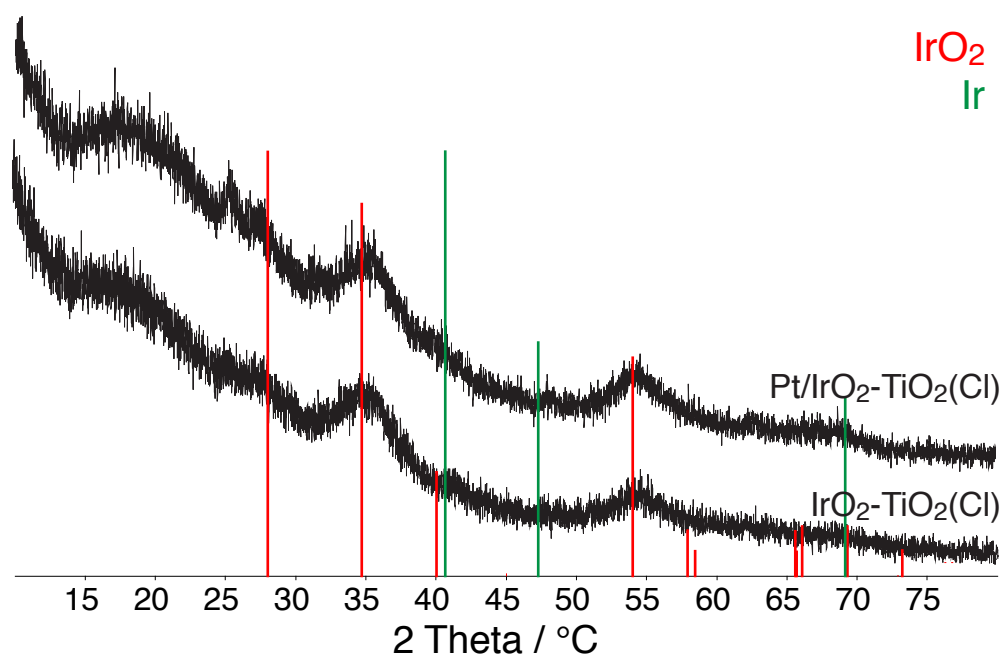


Figure A23: XRD powder diffraction patterns of IrO₂-TiO₂(Cl) and Pt/IrO₂-TiO₂(Cl) with reference patterns of IrO₂ (ref, ICDD 00-015-0870) and Ir (green, ICDD 00-046-1044).

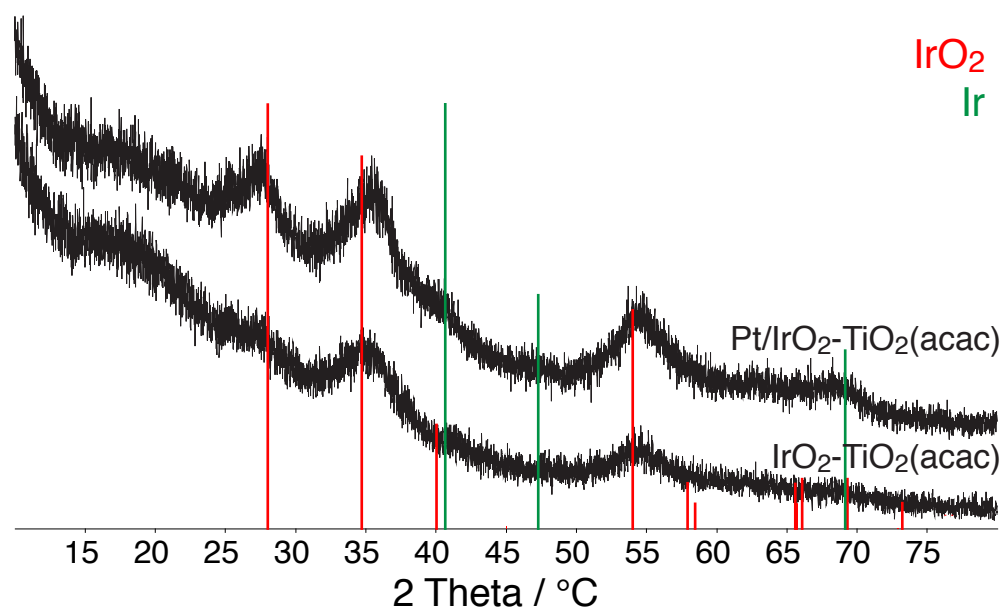


Figure A24: XRD powder diffraction patterns of IrO₂-TiO₂(acac) and Pt/IrO₂-TiO₂(acac) with reference patterns of IrO₂ (ref, ICDD 00-015-0870) and Ir (green, ICDD 00-046-1044).

Table A6: Ir content, surface area and electrical conductivities of the homemade and commercial iridium titanium oxide materials

Support	Ir content / mol _M %	S_{BET} / m ² .g ⁻¹	σ / S.cm ⁻¹
IrO ₂ -TiO ₂ (Umicore)	70	34	13
IrO ₂ -TiO ₂ (Cl)	40	251	0.3
IrO ₂ -TiO ₂ (acac)	40	245	0.2

Table A7: Average particle diameters of Pt in the commercial and homemade materials determined by anomalous SAXS measurements

Sample	Pt diameter / nm
Pt/C	2.4 ±0.6
Pt/IrO ₂ -TiO ₂ (Umicore)	2.0 ±0.3 ^[235]
Pt/IrO ₂ -TiO ₂ (Cl)	2.8 ±0.5
Pt/IrO ₂ -TiO ₂ (acac)	1.8 ±0.7

